이학박사학위논문

Effective potential and machine learning approaches to synchronization of coupled oscillators

결합된 진동자들의 동기화에 대한 유효 포텐셜 및
기계학습 접근법

2021년 2월

서울대학교 대학원

물리·천문학부

송 제 웅

Effective potential and machine learning approaches to synchronization of coupled oscillators

결합된 진동자들의 동기화에 대한 유효 포텐셜 및 기계학습 접근법

2021년 2월

서울대학교 대학원

물리·천문학부

송 제 웅

Effective potential and machine learning approaches to synchronization of coupled oscillators

결합된 진동자들의 동기화에 대한 유효 포텐셜 및 기계학습 접근법

지도교수 강 병 남
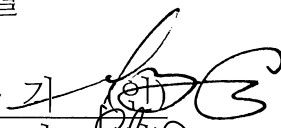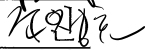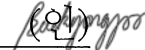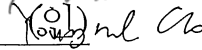
이 논문을 이학박사 학위논문으로 제출함
2021년 2월

서울대학교 대학원
물리·천문학부
송 제 웅

송제웅의 박사 학위논문을 인준함
2021년 1월

위 원 장: 양 운 기

부위원장: 강 병 남

위   원: 조 정 효

위   원: 백 용 주

위   원: 조 영 설

Abstract

Effective potential and machine learning approaches to synchronization of coupled oscillators

Je Ung Song

Department of Physics and Astronomy

The Graduate School

Seoul National University

Systems with multiple interacting elements exhibit collective behaviors. As one of examples of collective behaviors, synchronization is a process of coordinating two or more elements to realize the system in unison. It is an omnipresent phenomena in nature, for instance, firefly flashing, cricket chirping, cardiac pacemaker cell, and so on. To understand and describe the mechanism of synchronization phenomena, coupled oscillator system is often adopted as the most conventional and suitable model for interacting system. Each oscillator has own frequency representing each unique characteristics, and its phase is adjusted through the interaction with other oscillators on the system. On the way to phase synchronization, such interactions or connections between oscillators can be expressed as links on the complex network and each element (oscillator) is then denoted by a node. A number of studies for coupled oscillators on complex networks have been progressed over the past two decades.

Among the studies for synchronization of coupled oscillator systems, the Kuramoto model has played a crucial role as a simple and representative model for describing such collective behavior. Owing to its rich properties such as chaotic dynamical behavior and synchronization transition, the Kuramoto model is an appropriate

model to explore. First, fundamental results of previous studies on synchronization of the coupled oscillator system, especially the Kuramoto model, are introduced.

This dissertation is composed of two main studies for the coupled oscillator system by adopting two different approaches, respectively. As the first main study of this dissertation, we examine the Kuramoto model using analytical way, the effective potential approach. The Kuramoto model exhibits different types of synchronization transitions depending on the type of natural frequency distribution. To obtain these results, the Kuramoto self-consistency equation (SCE) approach has been used successfully. However, this approach affords only limited understanding of more detailed properties such as the stability. We here extend the SCE approach by introducing an effective potential, that is, an integral version of the SCE. We examine the landscape of this effective potential for second-order, first-order, and hybrid synchronization transitions in the thermodynamic limit. In particular, for the hybrid transition, we find that the minimum of effective potential displays a plateau across the region in which the order parameter jumps. This result suggests that the effective potential can be used to determine a type of synchronization transition.

In the second study for the coupled oscillator systems, we applied the machine learning approach to investigate the system based on data-driven analysis and to figure out whether the methodology can be extended to the real world system. With growing interest in the machine learning, recent works on physical systems has demonstrated successful progresses by adopting the machine learning approaches for tasks of classification and generation. We here perform various machine learning approaches to the Kuramoto system which is basic model for synchronization phenomena and exhibits complicated chaotic behavior. As the system displays rich properties such as synchronization transition and nonlinearity with varying parameters, we applied machine learning for finding the value of the coupling strength and the critical value. Considering the finite size scaling, we confirm that results follow the critical behavior

of the Kuramoto system. By focusing on the phase dynamics of all oscillators, we applied the performance of the artificial neural network for predicting future behaviors of all oscillators and detecting underlying real brain network topology. As the Kuramoto model offers support for the application on real-world systems exhibiting synchronization phenomena or nonlinear behaviors, our work has potential for utilizing the machine learning approaches to such systems.

Contents

List of Figures

List of Tables

Chapter 1

Introduction

1.1 Complex network

A wide variety of natural and artificial systems are described by complex organization of entities. For example, the Internet is a complex network of routers and computers linked by physical or wireless links; proteins can be nodes on a protein-protein interaction network with interaction between them denoted by links. Investigating the mechanisms of such interwoven systems leads to determine the topology of complex networks. In view of graph theory, a complex network is described mathematically as a graph G consisting of N nodes connected by L links. And the the degree of node i is denoted by k_i. And this graph can be represented by the adjacency matrix A with entries $a_{ij} = 1$ if a directed link from j to i exists, and 0 otherwise. For more general case of a weighted network W, its entries w_{ij} represent the strength (or weight) of the directed link from j to i. Through the investigation for the statistical properties of various forms of complex networks, one can classify complex networks in several categories. The degree distribution $P(k)$ which indicates the probability of a node to have a degree k, is the most representative of these statistical properties of complex networks. As the difference in the tail of the distribution is observed, homogeneous and heterogeneous networks are distinguished through the distribution $P(k)$. If it decays exponentially with the degree, the network is referred to as homogeneous. As a network composed of randomly connected nodes, the Erdos-Renyi (ER) network [1] is the most representative example. On the contrary, when the tail of the distribution
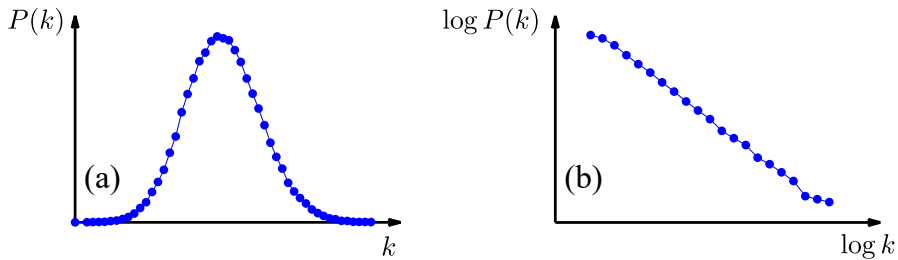
Figure 1.1: Degree distributions for Erdos-Renyi (ER) and scale-free (SF) networks. (a) The degree distribution for ER network follows the Poisson distribution. (b) The degree distribution for SF network follows a power-law distribution.

is heavy, one can refer to as heterogeneous network. As the most representative example of heterogeneous network, scale-free (SF) networks exhibit a power-law form of degree distribution, expressed as $P(k) \sim k^{-\gamma}$. By following a mechanism where all incoming nodes are linked preferentially to the existing nodes, Barabasi-Albert (BA) network is constructed as one of the model for describing the formation of scale-free networks [2]. It is well-known that many interaction patterns of natural and artificial networks such as the Internet, the World-Wide Web, scientific collaboration network, and biological networks, follow a power-law behavior, having a form of scale-free networks [3–9].

1.2 Coupled oscillators on complex networks

By focusing not only on the the network structure of real world network but also on the dynamics and interactions between nodes, studies for various real systems have been progressed by implementing complex network approaches. Among a number of complex systems, neural network in human brain is one of remarkable system to identify behavior of neurons and their collective phenomena. In the late 80's, studies for synchronization of coupled oscillators on a complex network were fostered to describe and understand such biological neural networks.

Strogatz and Mirollo [10] investigated the collective behavior of interacting limit

cycle oscillators with random intrinsic frequencies on lattice structures. One of the impressive findings in this study is that adding long-range connections leads to a more rapid and robust synchronization. This observation triggers vibrant studies of coupled oscillators on complex networks.

All nodes in models for describing this system are represented by oscillators which adjust their phases and finally set the phases to almost mean phase of their neighbors through non-linear interaction. Due to this interaction between oscillators, the model for this coupled oscillator system, governed by deterministic laws, demonstrates the chaotic behavior, where a small change in the initial state can result in large differences in the final state. This yields that prediction for long-term behavior becomes impossible in general although the deterministic mechanism is embedded.

1.3   Machine learning

In the meanwhile, we have witnessed remarkable advances of artificial intelligence applications in various fields of research areas over the past decade. As a sub-field of artificial intelligence, machine learning provides expectation for one of the ways of achieving artificial intelligence (AI). As the computer scientist and machine learning pioneer, Tom M. Mitchell defined the machine learning as : "Machine learning is the study of computer algorithms that allow computer programs to automatically improve through experience." in his book [11], machine learning relies on work with datasets by examining and comparing for desired purposes.

In the fields of science, experimental data can be the experience required to learn the machine. Such data-based or data-driven method is applied across many disciplines of science. For studies of statistical physics as well, machine learning method is implemented to verify the results obtained through other theoretical methods or to figure out new result which cannot be obtained through analytical or numerical ways. For phase transitions appearing in various systems such as classical Ising model, XY model, and quantum systems, machine learning methods have been adopted for clas-

sifying phases and finding the critical point [12–18]. For chaotic systems, in addition, prediction for the dynamical long-term behavior and inference of underlying variables have been proceeded steadily using the reservoir computing [19–29]. Nevertheless, there is lack of researches utilizing the machine learning approach to coupled oscillator systems yielding synchronization phenomena. As the synchronization transition and chaotic behavior both are exhibited on this coupled oscillator system, it is necessary and meaningful to identify the applicability of the machine learning approaches on such system and to which future work it can be helpful by extending the methods.

In this thesis, we investigate the coupled oscillator system with both analytic approach and data-driven approach. In chapter 2, we provide basic conception and backgrounds for synchronization which is a ubiquitous phenomena in nature and can be described by the coupled oscillator system. As one of the quintessential coupled oscillator model describing synchronization phenomena, the Kuramoto model and the corresponding synchronization transition arising as coupling strength increases is introduced and explained by defining the order parameter of the system.

In chapter 3, we investigate the synchronization transition with effective potential approach. From the self-consistency equation, the *ad hoc* potential for the Kuramoto model is constructed to provide intuitive understanding for behavior of the system, like the Landau potential energy scheme for phase transition of thermal system. Such methodology is applied to various natural frequency distributions and modified Kuramoto models exhibiting second, first, and hybrid synchronization transitions. In particular, models with the hybrid synchronization transition, display the plateau of the *ad hoc* potential landscape at the critical point and this quantity satisfies the criterion for the hybrid phase transition of thermal system. By analyzing the potential scheme for such non-equilibrium systems, our results imply that the methodology can be extended to other Kuramoto-type models to identify their transition types and properties.

In chapter 4, we demonstrate studies of machine learning approach to one of the coupled oscillator system, the Kuramoto model. We examine whether underlying pa-

rameters of the system can be deduced from the limited amount of information by introducing machine learning techniques. In the first work of this chapter, exploiting the machine learning to predict the coupling strength from the dynamics of the order parameter, we demonstrate that accurate value of coupling is obtained from the well-trained machine. Next, the snapshot of phases for all oscillators are also adopted to discriminate synchronized and asynchronized states and to determine the critical value of the Kuramoto system. As the learning the neural network with parameters of the Kuramoto model is achieved, we applied it to other model-free tasks. We predict the future evolution of the system by considering a situation where a detailed description for the dynamics of the system is unavailable or insufficient, but observational data of time evolution is given. Finally, underlying connections between oscillators are reconstructed from phase dynamics of all oscillators using the machine learning techniques. As the Kuramoto model offers support for the application on real-world systems exhibiting synchronization phenomena or nonlinear behaviors, our work has potential for utilizing the machine learning approaches to such systems.

We conclude in the final chapter.

Chapter 2

Synchronization of coupled oscillators

2.1   Synchronization

In the jungles of Southeast Asia (particularly in Malaysia, Thailand, and the Philippines), one can observe the nature's dramatic light shows by fireflies. By coordinating their flashing patterns, thousands of fireflies blink in perfect unison for minutes, sometimes hours. Meanwhile, on 10 June 2000, the day of opening of millennium bridge, thousands of people walked on the bridge at a time and the natural sway motion of people walking caused sideways oscillations in the bridge. And this bridge's movements caused people to sway in step, which induces the increase in the amplitude of the bridge again, and the "positive feedback" occurs. Due to this unexpected lateral vibration, the bridge was closed in 12 June for modifications. These two cases have features in common that individual's states or characteristics match with the neighbor's as time goes by, which are called "synchronization" phenomena.

Synchronization is a process of precisely coordinating or matching two or more things to realize the system in unison or the collective synchronous behavior. Besides the two examples mentioned above, there are a number of examples of synchronization in nature. Crickets can achieve synchronization by either lengthening or shortening their chirp intervals. Cardiac pacemaker cells are synchronized to control the contraction of heart muscles. And cellular clocks in the brain are integrated into a stable and robust pacemaker to sustain the rhythm of 24-hours-period. Rhythmic clapping of humans in an audience is also an example of the synchronization.

Such collective behaviors emerge due to interactions between individuals in the system. Through diverse form of active positive interactions between them, individual intrinsic properties can be restrained and the unity of the whole system can be achieved. As a variety of examples are observed in nature, analysis for real systems and the modeling for the synchronization phenomena are essential to understand the nature and utilize them.

2.2   Coupled oscillators

To describe the synchronization phenomena or setup the model, oscillators are usually adopted to represent elements in the system. Each oscillators have its own phases and such phases are changed with time as oscillators interact with each other.

One can consider two types of synchronization of coupled oscillators system: frequency synchronization and phase synchronization. Frequency synchronization indicates the state where all oscillators have equivalent frequencies or angular velocities regardless of their phases. On the other hand, the phase synchronization requires the condition that all oscillators have equal phases, which guarantees the equal frequencies as well.

There are various models which have been dealt with for studying synchronization of the coupled oscillator system. For example, the pulse-coupled model contains the interaction between oscillators with the form of a pulse. In particular, the integrate-and-fire oscillators, one of the pulse-coupled model, is used for describing the behavior of neurons in the brain. The system composed of this type of oscillators exhibits interesting dynamics and properties, however, we do not take into account such models in this dissertation, but the most representative model consisting of the limit cycle oscillators, the Kuramoto model.

2.3 The Kuramoto model

As one of the model describing the synchronization phenomena, the Kuramoto model has been widely dealt with as a mathematical model for the collective synchronization behavior [30, 31]. The Kuramoto model consists of N globally coupled oscillators interacting with each other via nonlinear coupling, which is written as

$$\dot{\theta}_i = \omega_i + \frac{K}{N} \sum_{j=1}^{N} \sin(\theta_j - \theta_i) \tag{2.1}$$

where θ_i is the phase of oscillator i. ω_i is the natural frequency of oscillator i that follows the distribution $g(\omega)$ and this represents intrinsic characteristic of each oscillator. And K denotes the coupling strength which indicates that how strongly the oscillators interact with each other. Hence, the phase of each oscillator evolves with time as the result of the combination of two terms in the right hand side of the Eq. (2.1). The first term is the oscillation term representing the velocity of the oscillator without any interactions. The second term is the interaction term representing the force to reduce phase differences by comparing with phases of other oscillators.

As K indicates the coupling strength, the system is in incoherent (asynchronous) state for sufficiently small value of K. As K increases, the system becomes in coherent (synchronous) state and oscillators in the system are synchronized. And the transition from the incoherent state to coherent state is referred as "synchronization transition" which will be treated in the Sec. 2.7.1.

The Kuramoto model of globally coupled oscillators given in Eq. (2.1) can be generalized for complex networks as

$$\dot{\theta}_i = \omega_i + K \sum_{j=1}^{N} A_{ij} \sin(\theta_j - \theta_i) \, . \tag{2.2}$$

Another form for complex networks is written as

$$\dot{\theta}_i = \omega_i + \frac{K}{k_i} \sum_{j=1}^{N} A_{ij} \sin(\theta_j - \theta_i) \tag{2.3}$$

where k_i is the degree of node i. And all these can be generalized by

$$\dot{\theta}_i = \omega_i + \frac{K}{k_i^{1-\alpha}} \sum_{j=1}^{N} A_{ij} \sin(\theta_j - \theta_i) \tag{2.4}$$

using the parameter α. When $\alpha = 1$, the Eq. (2.4) reduces to the Eq. (2.2) and when $\alpha = 0$, it reduces to the Eq. (2.3).

2.4   Natural frequency

As natural frequencies indicate intrinsic characteristic of oscillators in the system, the set of natural frequencies, $\{\omega_i\}$, is constant with time. This set of natural frequencies, $\{\omega_i\}$, is drawn from the natural frequency distribution $g(\omega)$ for finite size system. And such difference between oscillators induces the disorder in the system. Since the form of natural frequency distribution is important as it determines the type of phase transitions, we here introduce some distributions used frequently in the study of synchronization. We consider the case of thermodynamic limit of $N \to \infty$ for all contents in this section.

2.4.1   Gaussian distribution

Gaussian distribution for the set of natural frequencies is given by

$$g(\omega) = \frac{1}{\sqrt{2\pi\sigma^2}} e^{-\frac{(\omega - \omega_0)^2}{2\sigma^2}} \tag{2.5}$$

where ω_0 is the mean of the distribution and σ is its standard deviation. For this case, the system exhibits the second-order transition with the critical coupling of $K_c =$

$2/[\pi g(\omega_0)]$ [30, 31]. For the special case of the normal distribution with $\omega_0 = 0$ and $\sigma = 1$, the critical coupling is given by $K_c = \sqrt{8/\pi}$.

2.4.2 Lorentzian distribution

Lorentzian distribution is given by

$$g(\omega) = \frac{\gamma/\pi}{(\omega - \omega_0)^2 + \gamma^2}. \qquad (2.6)$$

where γ is the scale parameter. For this distribution, the second-order transition appears with the critical value of $K_c = 2\gamma$ [32, 33]. In particular, for the case of $\gamma = 1$ and $\omega_0 = 0$, the critical coupling is given by $K_c = 2$.

2.4.3 Uniform distribution

Uniform distribution with zero mean is given by

$$g(\omega) = \begin{cases} \frac{1}{2\gamma} & \text{for} \quad |\omega| \leq \gamma \\ 0 & \text{for} \quad |\omega| > \gamma \end{cases}. \qquad (2.7)$$

In this case, the hybrid synchronization transition occurs and the critical value and the jump height are given by $K_c = 2/[\pi g(0)] = 4\gamma/\pi$ and $r_c = \pi/4$, respectively [34]. It is introduced in section 3.5.1 which exhibits the hybrid synchronization transition.

2.5 Sampling of natural frequency

For the study of synchronization of the system with finite size, numerical simulations are required to verify the analytical approaches or observe the scaling behavior. To implement simulations, the set of natural frequencies, $\{\omega_i\}$ are selected from the distribution, $g(\omega)$, given in the previous section. Generally, there are two sampling methods : random sampling and regular sampling.
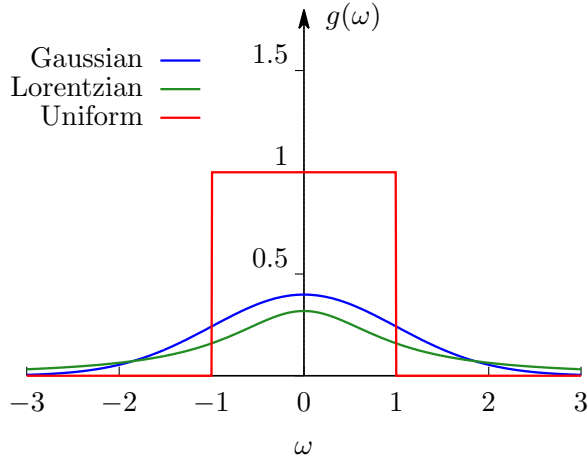
Figure 2.1: Various forms of natural frequency distribution. Blue line denotes the Gaussian distribution given in Eq. (2.5) with $\omega = 0$ and $\sigma = 1$. Green line denotes the Lorentzian distribution given in Eq. (2.6) with $\gamma = 1$ and $\omega_0 = 0$. Red line denotes the uniform distribution given in Eq. (2.7) with $\gamma = 1$.

2.5.1 Random sampling

For this sampling, all the natural frequencies are randomly selected from the distribution $g(\omega)$. Here, we used the "xorshift" for the random number generator in this study.

2.5.2 Regular sampling

For regular sampling, the set of natural frequencies can be assigned according to the equation

$$\int_{-\infty}^{\omega_j} g(\omega)d\omega = \frac{-0.5 + j}{N} \tag{2.8}$$

for $j = 1, 2, ..., N$, which indicates that the area under the distribution function curve are equally divided by N. In this case, the frequency-disorder fluctuation in natural frequency does not emerge, as the set of frequencies is determined as the form of distribution $g(\omega)$ is given.

(a) Gaussian distribution

By substituting Eq. (2.5) with $\omega = 0$ into Eq. (2.8), the natural frequencies are obtained as

$$\omega_j = \sqrt{2\sigma^2}\,\mathrm{erf}^{-1}\left(-1 + \frac{2j-1}{N}\right), \quad j = 1, 2, ..., N\,. \tag{2.9}$$

(b) Lorentzian distribution

In the same way, we can obtain the set of natural frequencies by inserting Eq. (2.6) into Eq. (2.8),

$$\omega_j = \gamma \tan\left(\frac{\pi}{2}\left(-1 + \frac{2j-1}{N}\right)\right), \quad j = 1, 2, ..., N\,. \tag{2.10}$$

Another regular sampling of the Lorentzian distribution is used by the authors in the paper [35], which is given by

$$\omega_j = \gamma \tan\left(\frac{\pi}{2}\left(-1 + \frac{2j}{N+1}\right)\right), \quad j = 1, 2, ..., N\,, \tag{2.11}$$

instead of Eq. (2.10).

(c) Uniform distribution

To assign N natural frequencies for the uniform distribution, there are two ways of regular sampling referred to as the midpoint rule and the endpoint rule [36]. For the uniform distribution with the range of $[-\gamma, \gamma]$, the midpoint rule is given by

$$\omega_j = \gamma\left(-1 + \frac{2j-1}{N}\right), \quad j = 1, 2, ..., N\,, \tag{2.12}$$

where the values of $\omega = \pm\gamma$ are not included in the sampling of $\{\omega_i\}$. And the endpoint is given by

$$\omega_j = \gamma\left(-1 + \frac{2j-2}{N-1}\right), \quad j = 1, 2, ..., N \tag{2.13}$$

Table 2.1: Natural frequency distributions and their regular sampling.

Distribution	$g(\omega)$	Regular sampling ω_i	
Gaussian	$\frac{1}{\sqrt{2\pi\sigma^2}}e^{-\frac{(\omega-\omega_0)^2}{2\sigma^2}}$	$\sqrt{2\sigma^2}\mathrm{erf}^{-1}\left(-1+\frac{2j-1}{N}\right)$	
Lorentzian	$\frac{\gamma/\pi}{(\omega-\omega_0)^2+\gamma^2}$	$\gamma\tan\left(\frac{\pi}{2}\left(-1+\frac{2j}{N+1}\right)\right)$	
Uniform	$\begin{cases}\frac{1}{2\gamma} & \text{for} \quad \|\omega\|\leq\gamma \\ 0 & \text{for} \quad \|\omega\|>\gamma\end{cases}$	$\begin{cases}\gamma(-1+\frac{2j-1}{N}) \\ \gamma(-1+\frac{2j-2}{N-1})\end{cases}$	mid-point rule end-point rule

where the values of $\omega = \pm\gamma$ are included in the sampling of $\{\omega_i\}$. Details for these two sampling methods are investigated in Ref. [36].

2.6 Order parameter

The collective behavior of the system with coupled oscillators is quantified by the complex order parameter Z, which is defined as

$$Z = re^{i\psi} = \frac{1}{N}\sum_{j=1}^{N} e^{i\theta_j} \qquad (2.14)$$

where ψ is the average phase and r indicates the phase coherence of oscillators and serves as a role of the order parameter during synchronization. In the thermodynamic limit of $N \to \infty$, when the system is in asynchronous state, the order parameter r is equal to zero which means that there is no coherence among oscillators. When the system is in synchronous state, r becomes a nonzero value and this means that there is phase coherence of oscillators.

Since phases of oscillators evolve with time, one can obtain the dynamics of the order parameter, $r(t)$. Generally, for given value of the coupling strength, the time-averaged value of the order parameter, $\langle r(t)\rangle$, in the steady state is taken for the statis-
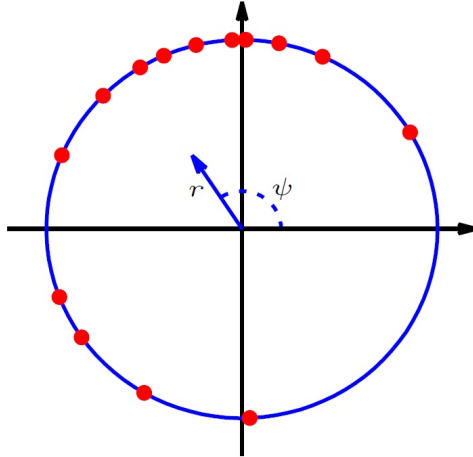
Figure 2.2: Complex order parameter as the centroid of all phases presented on complex plane.

tical analysis.

2.7 Phase transition

In statistical physics and thermodynamics, phase transition indicates the process of physical change in states of the system. As it is not confined only to the thermodynamic systems but also to the non-thermodynamic systems where temperature is not a parameter, phase transition appears in diverse complex systems.

2.7.1 Synchronization transition

As a mathematical model of ferromagnetism, the Ising model allows simple identification of phases and phase transitions. For this model, spins variables, s_i, are assigned on each sites and take only one of two possible values :

$$s_i = \pm 1 \,. \tag{2.15}$$

As the order parameter is a measure of order for the system, the net magnetization defined as the sum of all spin vectors can be one of the order parameter for this magnetic spin model. And the value of this order parameter changes with the temperature. When the temperature T is sufficiently large, spins are not aligned and the magnetization is nearly zero, which is corresponding to the disordered state. When T is small, however, spins are aligned in the same direction, and the order parameter becomes nearly one, which indicates the ordered state. Between these two states, the system exhibits a phase transition from disordered state to ordered state at the critical value of T_c.

Similarly, one can identify phases and phase transitions for the Kuramoto model as well. Without coupling strength, or $K = 0$, oscillators rotate with their given natural frequencies and their phases are distributed on a circle randomly. This is corresponding to the disordered state, or asynchronous state. In the thermodynamic limit of $N \to \infty$, the order parameter r remains at the value of zero for a sufficiently small value of K as in the Ising model. As K increases, r becomes a nonzero value at the critical strength K_c, which implies the occurrence of the ordered state, or the synchronous state, as shown in Fig 2.3. And such phase transition for synchronization phenomena is called "synchronization transition".

2.7.2 Hybrid phase transition

Phase transitions in equilibrium systems are conventionally classified according to the Ehrenfest classification scheme [37]. When the n-th derivative of the free energy with respect to its argument first becomes discontinuous, the phase transition is of the n-th order. Many phase transitions are either second-order or first-order, where an order parameter such as the magnetization changes from zero to a finite value continuously or discontinuously, and fluctuations are divergent or finite, respectively. However, this classification scheme does not accommodate some phase transitions. For instance, although the order parameter is discontinuous, critical behavior appears at the same transition point; e.g., the fluctuations of the order parameter and/or the cor-
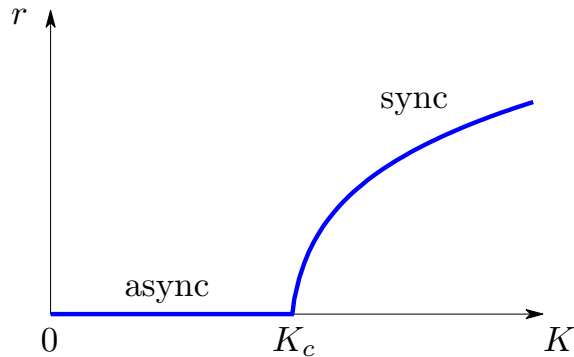
Figure 2.3: The change of the order parameter r as a function of the coupling strength K in the thermodynamic limit. The order parameter is equal to zero when the coupling strength is smaller than the critical coupling K_c, which is according to the disordered state, or the asynchronous state. When the coupling strength is larger than the critical coupling, r becomes a nonzero value implying the ordered state, or the synchronous state.

relation length diverge. This type of abnormal phase transition is called a mixed-order transition. In addition, a new type of phase transition has been observed, in which the order parameter exhibits the first-order and the second-order transition behavior at the same transition point. This type of transition is called a hybrid phase transition (HPT). The terms mixed-order and HPT may often be used interchangeably. Examples appear in various equilibrium and nonequilibrium systems, including the Ising model with long-range interactions in one dimension [38–41], the Ashkin–Teller (AT) model on scale-free networks [42], k-core percolation [43–47], DNA denaturation [48–50], jamming [51–53], crystallization of colloidal magnets [54], and coupled oscillators [34, 55–57].

2.7.3 Type of synchronization transition

For the Kuramoto system, the type of synchronization transition varies according to the topology or the setup of the model, such as the form of the natural frequency distribution. For example, it is well known that the Kuramoto model with natural frequencies
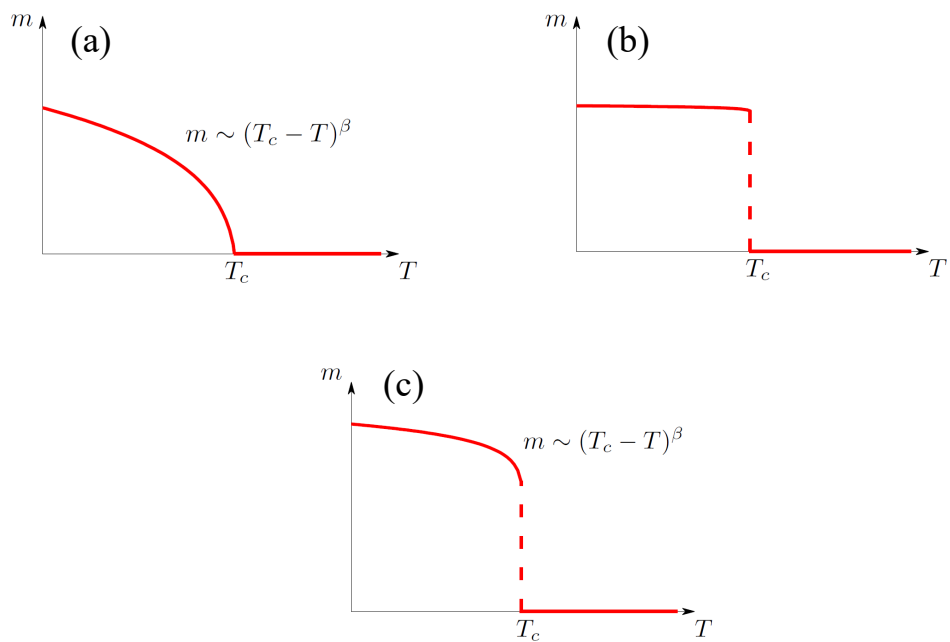
Figure 2.4: Schematic plots of several types of phase transitions. (a) For the second-order transition, the magnetization exhibits continuous transition and the critical behavior appears at the critical point. (b) For the first-order transition, the magnetization changes from zero to a finite value discontinuously at the critical point. (c) The change of magnetization is discontinuous and the critical behavior appears at the critical point for the hybrid phase transition.

following the normal distribution given by

$$g(\omega) = \frac{1}{\sqrt{2\pi}} e^{-\frac{\omega^2}{2}} \tag{2.16}$$

exhibits the second-order synchronization transition arising at the critical point $K_c = 2/[\pi g(0)] = \sqrt{8/\pi}$ in the limit $N \to \infty$ [30, 31]. And the critical value $K_c = 2/[\pi g(0)]$ is valid for any other unimodal symmetric distributions. For bimodal distribution, on the other hand, the first-order synchronization transition emerges [58–60]. And as a boundary case between unimodality and bimodality, the discontinuous transition with critical behavior, or the hybrid synchronization transition, appears for the uniform distribution [34].

2.8 Finite-size scaling

Since real systems are always finite, investigating the finite size effect is important to evaluate the unknown behavior of the system with the particular size. For the Kuramoto model, the finite number of oscillators induces different behaviors in physical quantities from the system in the thermodynamic limit of $N \to \infty$. Starting at the initial value of r_0, the order parameter is saturated after the relaxation time. And this saturated value of the order parameter r in the steady state depends on the system size N. In the subcritical regime, the dependence is given by $r \sim N^{-1/2}$, since the system is in asynchronous state and the randomness in natural frequencies dominate the dynamics of the system. As the coupling strength becomes larger and approaches to the critical value, $K \to K_c$, the order parameter exhibits another power-law behavior for different system sizes. This behavior can be understood using the finite-size scaling for various physical quantities, such as order parameter and susceptibility.

2.8.1 Critical exponents

The critical exponents describe the behavior of physical quantities near the critical point for the second-order phase transition or the hybrid phase transition with criticality. We here introduce several critical exponents of coupled oscillator systems in the thermodynamic limit. As one of the physical quantities, the correlation length diverges at the critical point $K = K_c$, which can be written as

$$\xi \sim \epsilon^{-\nu_\perp} \tag{2.17}$$

where $\epsilon = (K - K_c)/K_c$ and $\nu_\perp$ is the critical exponent relating the size of correlations to the temperature (coupling strength in this case). And the correlation time also diverges at the critical point $K = K_c$,

$$\begin{aligned} \tau &\sim \epsilon^{-\nu_\parallel} \\ &\sim \left(\xi^{-1/\nu_\perp} \right)^{-\nu_\parallel} \\ &= \xi^{\nu_\parallel/\nu_\perp} \equiv \xi^z \end{aligned} \tag{2.18}$$

where z denotes the dynamical exponent. And the saturated value of the order parameter r exhibits the behavior of

$$r \sim \epsilon^\beta \tag{2.19}$$

in the supercritical region. The susceptibility χ for the Kuramoto model is defined as

$$\begin{aligned} \chi &\equiv N[\langle (r - \langle r \rangle)^2 \rangle] \\ &= N[\langle r^2 \rangle - \langle r \rangle^2] \end{aligned} \tag{2.20}$$

where $\langle \cdot \rangle$ denotes the time average in the steady state of a given sample and $[\cdot]$ denotes the sample average, respectively. Near the criticality, the susceptibility diverges as

$$\chi \sim |\epsilon|^{-\gamma} .$$
(2.21)

2.8.2 Finite-size effect

Although the physical quantities such as the correlation length, correlation time and the susceptibility diverge at the critical point in the thermodynamic limit of $N \to \infty$, quantities for the finite-size systems does not diverge any longer. For example, as the correlation length cannot exceed the system size $L = N^{1/d}$ even at the critical value $\epsilon = 0$, one should consider the "finite-size effect" to evaluate the behavior of the correlation length near the critical point for the finite-size system. And this can be expressed as

$$\epsilon^{-\nu_\perp} \sim \xi \sim L = N^{1/d} .$$
(2.22)

Rewriting Eq. (2.22), we obtain

$$\epsilon \sim N^{-1/d\nu_\perp} \equiv N^{-1/\bar{\nu}}$$
(2.23)

and

$$\epsilon N^{1/\bar{\nu}} = \text{const} .$$
(2.24)

Using Eq. (2.23), one can identify the behavior of the order parameter and the susceptibility for the system with finite size N. Combining Eq. (2.19) and Eq. (2.23), we get

$$r \sim \epsilon^{\beta} \sim N^{-\beta/\bar{\nu}} .$$
(2.25)

And this equation can be generalized by writing

$$r \sim N^{-\beta/\bar{\nu}} f_r(\epsilon N^{1/\bar{\nu}}) \tag{2.26}$$

where $f_r(x)$ is the scaling function for the order parameter. As the scaling function behaves as $f_r(x) \sim x^\beta$ for $x \gg 1$ and constant for $x \to 0$, relations $r \sim N^{-\beta/\bar{\nu}}$ for $\epsilon = 0$ and $r \sim \epsilon^\beta$ for $N \to \infty$ are recovered.

In the same way, the finite-size effect for the susceptibility is written as

$$\chi \sim |\epsilon|^{-\gamma} \sim N^{\gamma/\bar{\nu}}. \tag{2.27}$$

And this equation can be generalized as

$$\chi \sim N^{\gamma/\bar{\nu}} f_\chi(\epsilon N^{1/\bar{\nu}}) \tag{2.28}$$

where $f_\chi(x)$ is the scaling function for the susceptibility. As the scaling function behaves as $f_\chi(x) \sim |x|^{-\gamma}$ for $x \gg 1$ and constant for $x \to 0$, relations $\chi \sim N^{\gamma/\bar{\nu}}$ for $\epsilon = 0$ and $\chi \sim |\epsilon|^{-\gamma}$ for $N \to \infty$ are recovered.

These critical exponents can be obtained through the numerical calculation for the Kuramoto model with finite size systems. For example, it is well known that $\beta = 1/2, \gamma = 1$ and $\bar{\nu} = 5/2$ are obtained for the Gaussian distribution of $\{\omega_i\}$ [61–64]. As shown in Figs. 2.5 to 2.8, we verify critical exponents numerically and obtained $\beta/\bar{\nu} \approx 0.224$ and $\gamma/\bar{\nu} \approx 0.425$.
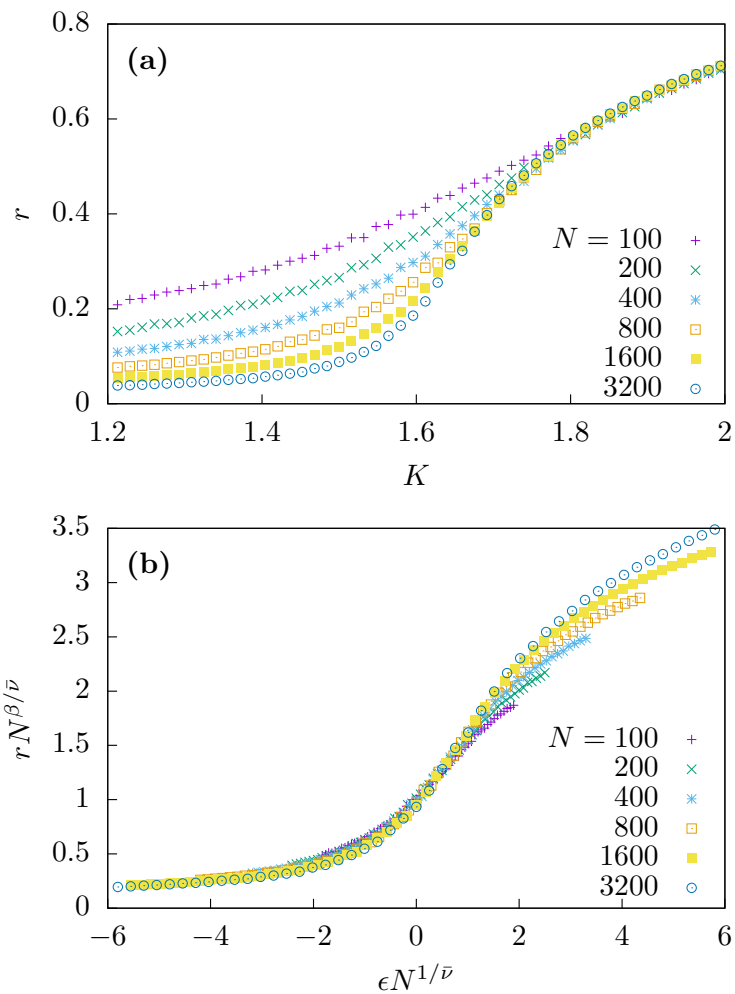
Figure 2.5: Finite-size scaling for the order parameter r. Here, the case of Gaussian distribution of $\{\omega_i\}$ with random sampling is considered where the critical coupling $K_c = \sqrt{8/\pi} \approx 1.59577$ is given. 1000 ensembles for each points are calculated. (a) The order parameter as a function of coupling strength K for various system sizes are obtained numerically. (b) With given exponents of $\beta = 1/2$ and $\bar{\nu} = 5/2$, the data collapse is performed.
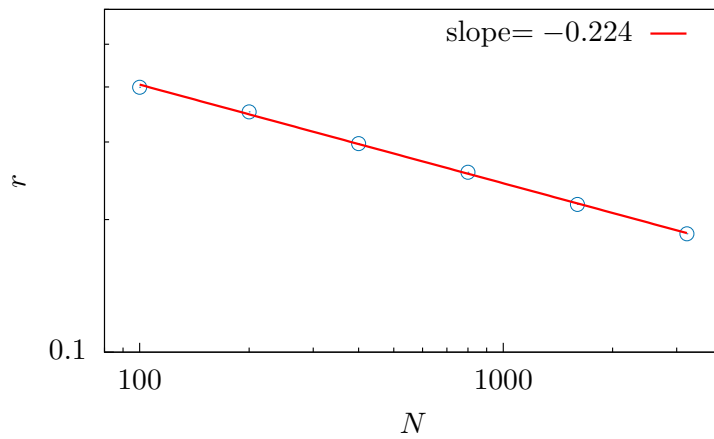
Figure 2.6: The change of the order parameter r as a function of system size N at the critical coupling $K = K_c$. 1000 ensembles for each points are calculated. As the slope denotes $-\beta/\bar{\nu}$, we obtained $\beta/\bar{\nu} \approx 0.224$ which is consistent value to critical exponents $\beta = 1/2$ and $\bar{\nu} = 5/2$.
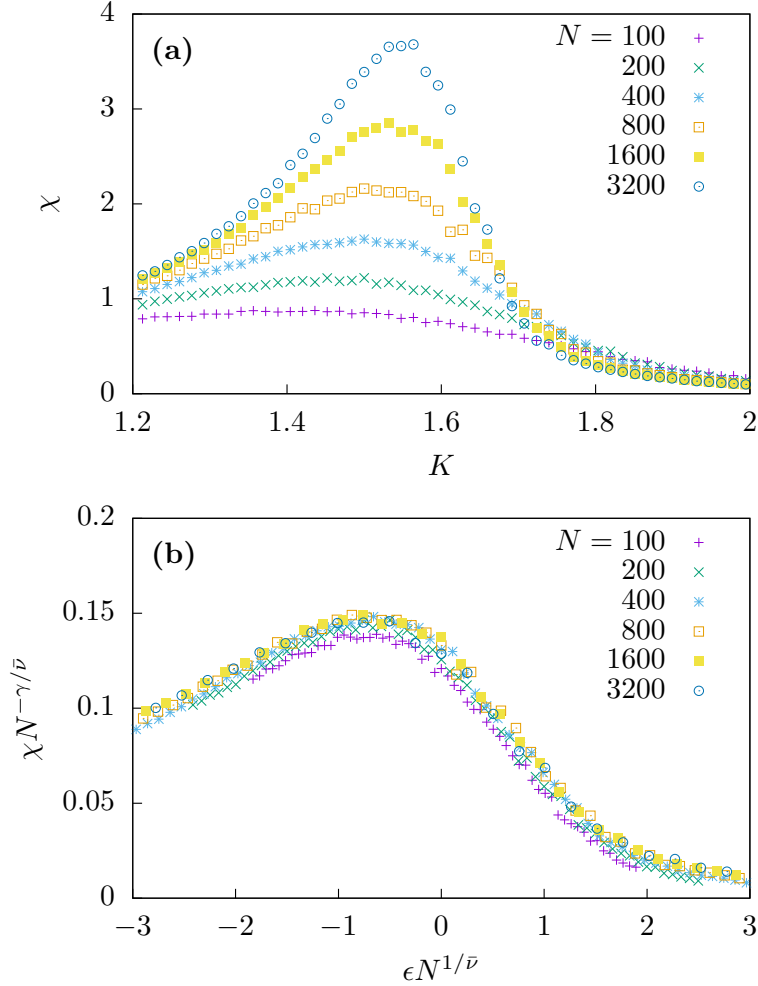
Figure 2.7: Finite-size scaling for the susceptibility χ. Here, the case of Gaussian distribution of $\{\omega_i\}$ with random sampling is considered where the critical coupling $K_c = \sqrt{8/\pi} \approx 1.59577$ is given. 1000 ensembles for each points are calculated. (a) The susceptibility as a function of coupling strength K for various system sizes are obtained numerically. (b) With given exponents of $\gamma = 1$ and $\bar{\nu} = 5/2$, the data collapse is performed.
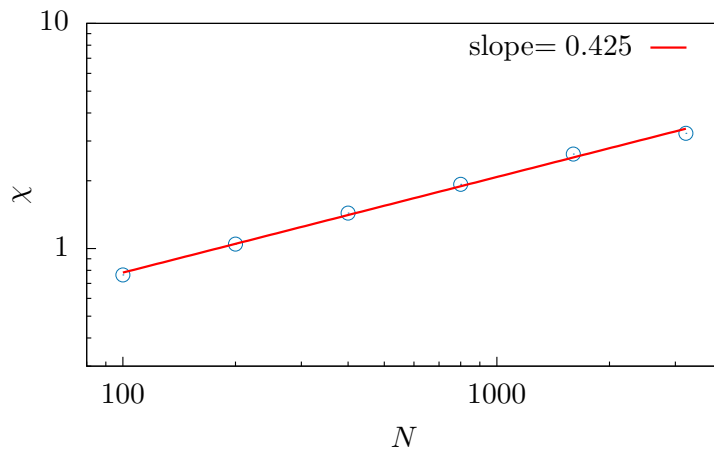
Figure 2.8: The change of the susceptibility χ as a function of system size N at the critical coupling $K = K_c$. 1000 ensembles for each points are calculated. As the slope denotes $\gamma/\bar{\nu}$, we obtained $\gamma/\bar{\nu} \approx 0.425$ which is consistent value to critical exponents $\gamma = 1$ and $\bar{\nu} = 5/2$.

Chapter 3

Effective potential approach to synchronization transition

Landau theory has been useful for determining the type of phase transition in equilibrium systems and determining the critical exponents in the mean-field limit for the second-order transition. The Landau free energy $\mathcal{L}(m)$ in Euclidean space is expanded with respect to the order parameter m (the magnetization) in polynomial form as

$$\mathcal{L}(m) = \frac{1}{2}(T - T_x)m^2 - \frac{1}{3}a_3 m^3 + \frac{1}{4}a_4 m^4 + \cdots . \qquad (3.1)$$

For the second-order transition, a_3 is zero when $\mathcal{L}(m) = \mathcal{L}(-m)$ is symmetric, and $a_4 > 0$. T_x becomes a transition point T_c, across which the position of the global minimum of $\mathcal{L}(m)$ changes from $m = 0$ for $T > T_c$ to finite m (e.g., $m > 0$) for $T < T_c$. $\partial \mathcal{L}/\partial m = 0$ and $\partial^2 \mathcal{L}/\partial m^2 < 0$ at $m = 0$ and $T = T_c$. For the first-order transition, $a_3 > 0$. $\mathcal{L}(m)$ has a minimum at $m = 0$ for $T > T_x$. Moreover, there exists $m^*(T) > 0$ such that $\partial \mathcal{L}/\partial m = 0$ at m^* when $a_3^2 > 4a_4(T - T_x)$ for $T > T_x$. The local minimum of $\mathcal{L}$ at m^* becomes a global minimum at T_c. Then, for $T < T_c$, a global free energy minimum exists at $m = m^*$. Thus, the first-order transition occurs at T_c, which is higher than T_x. Therefore, the order parameter is discontinuous across T_c. We remark that $\partial^2 \mathcal{L}/\partial m^2 > 0$ at $m = 0$ for T_c.

Recently, the Landau theory was extended to the HPT. The authors of Ref. [42] investigated the AT model on scale-free networks. In the AT model, two types of Ising spins are located on each node of a scale-free network. Two spins of each type at the

26

nearest-neighbor nodes interact with strength J_2, and four spins of both types at the nearest-neighbor nodes interact with strength J_4. The Landau free energy was established. Owing to the power-law behavior of the degree distribution of scale-free networks, the Landau free energy contains m terms with non-integer powers. For specific cases in the parameter space $(T, J_4/J_2, \lambda)$, where λ is the exponent of the degree distribution, an HPT occurs at the so-called critical endpoint. The order parameter jumps and includes critical behavior at the same transition point. The fluctuations of the order parameter are finite and diverge on either side of the transition point. The authors of Ref. [42] investigated the profile of the Landau free energy at this critical endpoint and established the criterion for the HPT within the Landau theoretical scheme as follows: At $T = T_c$, the free energy has two global minima at $m = 0$ and $m^* > 0$. Thus, for $T > T_c$, the global minimum occurs at $m = 0$, and for $T < T_c$, the global minimum occurs at $m^*(T)$. Mathematically, the criterion for the HPT is written as

$$
\begin{aligned}
\mathcal{L} = 0, \ \frac{\partial \mathcal{L}}{\partial m} = 0, \ \text{and} \ \frac{\partial^2 \mathcal{L}}{\partial m^2} = 0 \qquad & \text{at } m = 0 \ \text{ and } \ T = T_c, \\
\mathcal{L} = 0, \ \frac{\partial \mathcal{L}}{\partial m} = 0, \ \text{and} \ \frac{\partial^2 \mathcal{L}}{\partial m^2} \geq 0 \qquad & \text{at } m = m^* \text{ and } \ T = T_c, \\
\mathcal{L} < 0, \ \frac{\partial \mathcal{L}}{\partial m} = 0, \ \text{and} \ \frac{\partial^2 \mathcal{L}}{\partial m^2} > 0 \qquad & \text{at } m = m^* \text{ and } \ T < T_c.
\end{aligned}
\tag{3.2}
$$

The profiles of the Landau free energy as a function of the order parameter for different types of phase transitions are shown in Fig. 3.1. This criterion was confirmed by theoretical and experimental studies of the crystallization of colloidal magnets, in which the free energy is zero throughout the region $m = [0, m^*]$ [54].

We note that the Landau theory criterion for the HPT was established in equilibrium thermal systems. Thus, in this section, we aim to examine whether there exists a quantity corresponding to the Landau free energy and then to check whether the criterion for the HPT is still valid and useful in nonequilibrium dynamic systems. For this purpose, we consider Kuramoto models (KMs) with particular types of natural frequencies that exhibit HPTs [34, 56, 57].
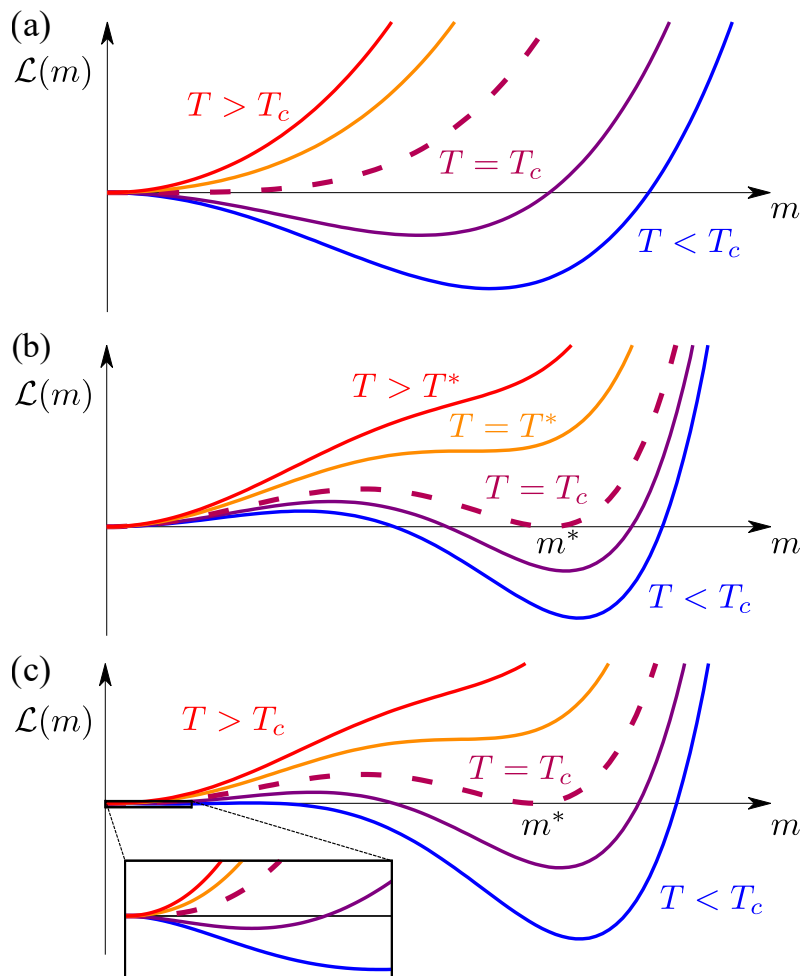
Figure 3.1: Schematic plots of the Landau free energy $\mathcal{L}(m)$ as a function of the order parameter m for (a) second-order, (b) first-order, and (c) hybrid phase transitions in thermal systems.

3.1 Analytic approaches to the Kuramoto model

Here, we will treat the way of understanding the Kuramoto model with analytic approaches. By substituting Eq. (2.14) into Eq. (2.1), one can obtain the equation

$$\dot{\theta}_i = \omega_i + Kr \sin(\psi - \theta_i) \,. \tag{3.3}$$

which is the dynamic equation for oscillator i only and describes its behavior of time evolution.

3.1.1 Self-consistency analysis

The solutions of Eq. (3.3) exhibit two types of behavior. Oscillators with natural frequencies satisfying $|\omega_i| \leq Kr$ are phase-locked in the rotating frame. These oscillators contribute to the nonzero coherence r. For these oscillators, the distribution of phases θ at given ω is given by

$$\rho_\omega(\theta) = \delta \left(\theta - \arcsin \left(\frac{\omega}{Kr} \right) \right) \,. \tag{3.4}$$

By contrast, the oscillators with $|\omega_i| > Kr$ from a symmetric distribution of $g(\omega)$ are drifting around the circle and do not contribute to r [65–67]. For these drifting oscillators, the distribution is given by

$$\rho_\omega(\theta) = \frac{C}{|\dot{\theta}|}$$
$$= \frac{C}{|\omega - Kr \sin \theta|} \tag{3.5}$$

where C is constant. Using the invariance under global rotation, we can set $\psi = 0$ without loss of generality. As oscillators in the system are divided into two groups,

this gives the order parameter equation in the $N \to \infty$ limit as

$$
\begin{aligned}
r &= \langle e^{i\theta} \rangle \\
&= \langle e^{i\theta} \rangle_{\text{lock}} + \langle e^{i\theta} \rangle_{\text{drift}} \\
&= r_{\text{lock}} + r_{\text{drift}} .
\end{aligned} \tag{3.6}
$$

The first term for locked oscillators, r_{lock}, becomes

$$
\begin{aligned}
r_{\text{lock}} &= \langle e^{i\theta} \rangle_{\text{lock}} \\
&= \int_{-Kr}^{Kr} e^{i\theta} g(\omega) d\omega \\
&= \int_{-Kr}^{Kr} \cos \theta(\omega) g(\omega) d\omega + i \int_{-Kr}^{Kr} \sin \theta(\omega) g(\omega) d\omega \\
&= \int_{-Kr}^{Kr} \cos \theta(\omega) g(\omega) d\omega .
\end{aligned} \tag{3.7}
$$

Here, the imaginary term is vanished since $\sin \theta(\omega) = \frac{\omega}{Kr}$ has a form of odd function and $g(\omega)$ is assumed as an even function. And the drifting term for the order parameter can be written as

$$
\begin{aligned}
r_{\text{drift}} &= \langle e^{i\theta} \rangle_{\text{drift}} \\
&= \langle \cos \theta \rangle_{\text{drift}} + i \langle \sin \theta \rangle_{\text{drift}} .
\end{aligned} \tag{3.8}
$$

Here, $\langle \cos \theta \rangle_{\text{drift}}$ becomes

$$
\begin{aligned}
\langle \cos \theta \rangle_{\text{drift}} &= \int_{-\pi}^{\pi} \int_{|\omega| > Kr} \cos \theta \rho_\omega(\theta) g(\omega) d\omega d\theta \\
&= \int_{-\pi}^{0} \int_{-\infty}^{-Kr} \cos \theta \rho_\omega(\theta) g(\omega) d\omega d\theta \\
&\quad + \int_{-\pi}^{0} \int_{Kr}^{\infty} \cos \theta \rho_\omega(\theta) g(\omega) d\omega d\theta \\
&\quad + \int_{0}^{\pi} \int_{-\infty}^{-Kr} \cos \theta \rho_\omega(\theta) g(\omega) d\omega d\theta \\
&\quad + \int_{0}^{\pi} \int_{Kr}^{\infty} \cos \theta \rho_\omega(\theta) g(\omega) d\omega d\theta \,.
\end{aligned} \tag{3.9}
$$

Using $\rho_\omega(\theta) = \rho_{-\omega}(\theta + \pi)$ and $g(\omega) = g(-\omega)$, we get

$$
\langle \cos \theta \rangle_{\text{drift}} = 0 \,. \tag{3.10}
$$

In the same way, it can easily be shown that the $\langle \sin \theta \rangle_{\text{drift}}$ is also equal to zero. It indicates that the contribution to the value of order parameter comes only from $\langle \cos \theta \rangle_{\text{lock}}$. Thus, in the steady state, the order parameter r satisfies the self-consistency equation (SCE)

$$
\begin{aligned}
r &= \int_{-\pi}^{\pi} d\theta \int_{-Kr}^{Kr} d\omega \cos \theta g(\omega) \delta \left(\theta - \arcsin \left(\frac{\omega}{Kr} \right) \right) \\
&= \int_{-Kr}^{Kr} d\omega \sqrt{1 - \frac{\omega^2}{K^2 r^2}} g(\omega) \equiv f(r) \,.
\end{aligned} \tag{3.11}
$$

And the SCE is reduced to $f(r) - r = 0$.

3.1.2 Ott-Antonsen ansatz

Another analytic approaches to the Kuramoto model was introduced in Ref. [32]. Ott and Antonsen, authors of the paper [32], obtained analytical description for the macroscopic dynamics of Kuramoto systems by reducing the dimension.

For this explanation, we can start by considering the continuum limit of infinitely many Kuramoto oscillators. As in the previous section, we again set the distribution density of oscillators as $\rho(\theta, \omega, t)$ for given phase θ, natural frequency ω, and time t satisfying

$$z^*(t) = \int_{-\infty}^{\infty} \int_{-\pi}^{\pi} e^{-i\theta} \rho(\theta, \omega, t) d\theta d\omega. \tag{3.12}$$

For $N \to \infty$, the time evolution of $\rho(\theta, \omega, t)$ must obey the continuity equation such that

$$\frac{\partial \rho(\theta, \omega, t)}{\partial t} + \frac{\partial \rho(\theta, \omega, t)}{\partial \theta} (\dot{\theta} \rho(\theta, \omega, t)) = 0. \tag{3.13}$$

For the Kuramoto oscillators, it becomes

$$\frac{\partial \rho(\theta, \omega, t)}{\partial t} + \frac{\partial \rho(\theta, \omega, t)}{\partial \theta} \left[\left(\omega + \frac{K}{2i} \left(z e^{-i\theta} - z^* e^{i\theta} \right) \right) \rho(\theta, \omega, t) \right] = 0. \tag{3.14}$$

Authors considered the Fourier expansion of ρ in θ of the form

$$\rho(\omega, \theta, t) = \frac{g(\omega)}{2\pi} \left[1 + \sum_{k=1}^{\infty} \hat{\rho}_k(\omega, t) e^{in\theta} + \text{c.c.} \right] \tag{3.15}$$

where $\hat{\rho}_k$ denotes the n-th Fourier coefficient and c.c. stands for the complex conjugate. By considering a restriction on phase space, Ott-Antonsen(OA) ansatz is suggested :

$$\hat{\rho}_k(\omega, t) = \alpha^k(\omega, t) \tag{3.16}$$

with analytic function of $\alpha(\omega, t)$. Using the OA ansatz, substitution of Eq. (3.15) into Eq. (3.12) and Eq. (3.14) leads to

$$z^* = \int_{-\infty}^{\infty} \alpha(\omega, t) g(\omega) d\omega \tag{3.17}$$

and

$$\frac{\partial \alpha}{\partial t} + i\omega\alpha + \frac{K}{2}(z\alpha^2 - z^*) = 0\,, \tag{3.18}$$

respectively.

To proceed further, the contour integration in Eq. (3.17) have to be evaluated using the residue theorem for appropriate distribution of $g(\omega)$. In particular, for the Lorentzian distribution given in Eq. (2.6), the integration can be analytically calculated as $g(\omega)$ have simple poles, which are given by $\omega_0 \pm i\gamma$, in the complex ω plane. Then, the contour integration of Eq. (3.17) along the path encircling the lower complex half-plane gives the result

$$z^* = \alpha(\omega_0 - i\gamma, t)\,. \tag{3.19}$$

By inserting into Eq. (3.18), it becomes

$$\begin{aligned} \dot{z} &= (-\gamma + i\omega_0)z + \frac{K}{2}(z - |z|^2 z) \\ &= \left(\frac{K}{2} - \gamma\right)z + i\omega_0 z - \frac{K}{2}|z|^2 z \end{aligned} \tag{3.20}$$

which is the ordinary differential equation for the complex order parameter z. Thus, this equation provides the order parameter dynamics of the Kuramoto system with infinite number of oscillators. Also, one can notice that a supercritical Hopf bifurcation emerges at $K_c = 2\gamma$ which indicates that the solution for stable synchronous state arises.

3.2   *Ad hoc* **free energy**

To investigate the dynamic flow and the stability of the SCE, one may choose an *ad hoc* potential, which makes it possible to visualize the entire landscape in a given parameter

space. Like the Landau theory, this landscape may give some clues to determining the synchronization transition types.

In physics, the concept of potential energy is well established as that is associated with the configuration of a system in which a force acts. This is formulated as

$$F(r) = -\frac{dU}{dr}.$$

(3.21)

When the system is dynamic near an equilibrium state, the relaxation to a stable equilibrium is expressed as the overdamped equation

$$\mu\frac{dr}{dt} = F(r) = -\frac{dU}{dr},$$

(3.22)

where μ is the friction coefficient and acts as the inverse of relaxation rate. This formulation may not be suitable to a far-from equilibrium system including the systems associated with the Kuramoto equation. Nevertheless, there was an attempt [68] to introduce a fictitious potential along the idea of near equilibrium system as:

$$\frac{d\theta_i}{dt} = -\frac{\partial U(\{\theta_i\})}{\partial \theta_i},$$

(3.23)

where

$$U(\{\theta_i\}) = -\omega_i\theta_i - \frac{K}{2N}\sum_{i,j}\cos(\theta_j - \theta_i).$$

(3.24)

ω_i is regarded as a random field applied to oscillator i and the second term on the r.h.s is called the Lyapunov function.

In this dissertation, we do not follow the formalism (3.23). Let us define

$$F(r) \equiv f(r) - r = 0$$

(3.25)

from the SCE and the *ad hoc* potential $U(r)$ through the relation $F(r) = -dU(r)/dr$.

In turn, $U(r)$ is written as

$$U(r) = \int_0^r (r' - f(r'))dr', \qquad (3.26)$$

where we set $U(0) = 0$ for simplicity. This suggests that for a given frequency distribution $g(\omega)$, $f(r)$ as defined in Eq. (3.11) allows us to explore the potential across the order parameter region.

$\left[\partial U/\partial r\right]_{r=r^*} = 0$ implies that r^* can be a solution of the SCE, but with losing the stability information. To guarantee the solution being stable, we need

$$\left[\frac{\partial^2 U}{\partial r^2}\right]_{r=r^*} > 0\,, \qquad (3.27)$$

so that the stable solution is confined in the potential well. We find that the choice of $F(r) = f(r) - r$ satisfies this stability criterion for the Kuramoto models discussed later. In fact, setting up a rigorous stability criterion for the SCE of the Kuramoto-type equation is not simple. An empirical linear stability condition of the complex SCE was proposed [69], which has been validated numerically for many cases. When $g(\omega)$ is symmetric, the cases we consider throughout this section, their stability condition is reduced to the above $\left[\partial^2 U/\partial r^2\right]_{r=r^*} > 0$. Under these stability criteria $\left[\partial U/\partial r\right]_{r=r^*} = 0$ and $\left[\partial^2 U/\partial r^2\right]_{r=r^*} > 0$, at the transition point, a second-order transition has a single stable solution at $r^* = 0$; a first-order transition has two stable solutions at $r_0^* = 0$ and r_2^*, and one unstable solution at r_1^* between the two stable solutions; and a hybrid phase transition in finite systems has many solutions r^* of $\left[\partial U/\partial r\right]_{r=r^*} = 0$, but their signs of stability alternate. As the determining of $F(r)$ can be somewhat ambiguous in Kuramoto models, we tried to pay attention on the state achieved by the system, hence our choice of $F(r) \equiv f(r) - r$ is consistent with the expected outcome and useful for the construction of $U(r)$.

In the mean time, the equation of motion for the order parameter r was derived using the Ott-Antonsen ansatz for the case of Lorentzian natural frequency distribu-

tion [32] as follows:

$$\frac{dr}{dt} = \left(\frac{K}{2} - \gamma\right)r - \frac{K}{2}r^3. \tag{3.28}$$

On the other hand, our *ad-hoc* potential is obtained as:

$$
\begin{aligned}
F(r) &= \int_{-Kr}^{Kr} d\omega \frac{\gamma/\pi}{\omega^2 + \gamma^2} \sqrt{1 - \frac{\omega^2}{K^2 r^2}} - r \\
&= \frac{\sqrt{K^2 r^2 + \gamma^2} - \gamma}{Kr} - r \\
&= \left(\frac{K}{2\gamma} - 1\right)r - \frac{K^3 r^3}{8\gamma^3} + O(r^5).
\end{aligned} \tag{3.29}
$$

Up to the leading order, the equation of motion (3.28) is also obtained approximately by the following relaxation equation

$$\frac{dr}{dt} = \gamma F(r), \tag{3.30}$$

from the *ad-hoc* potential at the transition point.

We emphasize that our method can serve as a useful framework for determining the phase transition type for various frequency distributions other than Lorentzian, which is hard to achieve otherwise. The method clearly reveals the role of the shape of natural frequency distribution, expressing it in a much interpretable picture: a potential landscape. In the following, we investigate the profiles of *ad hoc* potentials for second-order, first-order, and hybrid synchronization transitions for different types of natural frequency distributions in thermodynamic limit of $N \to \infty$. (*Ad hoc* potential analysis for the system with finite size is described in Appendix C.)

3.3 Second-order synchronization transition

Here we consider the *ad hoc* potential of the SCE for the Gaussian distribution $g(\omega)$ given by

$$g(\omega) = \frac{1}{\sqrt{2\pi}} e^{-\frac{\omega^2}{2}}. \tag{3.31}$$

We obtain the SCE as

$$r = \sqrt{\frac{\pi A}{2}} e^{-A} \left[I_0\left(A\right) + I_1\left(A\right) \right], \tag{3.32}$$

where $A = K^2 r^2/4$, and I_α ($\alpha = 0$ and 1) denotes the modified Bessel functions of the first kind. For this $g(\omega)$, the order parameter increases continuously from $r = 0$ to finite r as K is increased from a transition point $K_c = 2/[\pi g(0)]$ [30, 31].

Thus, we expand the r.h.s. of Eq. (3.32) with respect to r at $r = 0$ for $K = K_c$ and obtain that

$$r = \frac{K}{K_c} r - \frac{K^3}{\pi K_c^3} r^3 + \mathcal{O}(r^5). \tag{3.33}$$

The *ad hoc* potential is obtained as

$$U(r) = \frac{K - K_c}{2K_c} r^2 - \frac{K^3}{4\pi K_c^3} r^4 + \mathcal{O}(r^6). \tag{3.34}$$

The profile of the *ad hoc* potential is shown in Fig. 3.2(a) for various K values. The sign of the coefficient of the r^2 term changes from positive to negative as K is decreased beyond K_c, implying that the stability at $r = 0$ is also inverted. We again investigate the relationship between the position of the minimum and the coupling strength, and obtain

$$r \sim (K - K_c)^{1/2} \tag{3.35}$$

for $K \to K_c$. Using numerics, we plot r^*, at which the minimum of $U(r)$ appears, in Fig. 3.2(b) as a function of the coupling strength K. Starting from a small value of K, the minimum remains at $r = 0$ until K approaches K_c, and it increases continuously for $K > K_c$ following the relation given in Eq. (3.35) [30, 31].

3.4 First-order synchronization transition

3.4.1 Degree-frequency correlation on a scale-free network with $2 < \lambda < 3$

Refs. [55, 56] consider the KM with degree–frequency correlation on scale-free networks with a power-law degree distribution $P_d(q) \sim q^{-\lambda}$. Using the annealed network approach, the KE is written as

$$\dot{\theta}_i = \omega_i + \sum_{j=1}^{N} \frac{Kq_iq_j}{N\langle q \rangle} \sin(\theta_j - \theta_i), \tag{3.36}$$

where q_i and q_j are the degrees of nodes i and j, respectively, and $\langle q \rangle$ is the mean degree, which is defined as $\langle q \rangle = \sum_j q_j / N$. The degree–frequency correlation is given in the form of $\omega_i = q_i$. The complex order parameter of the system is defined as

$$Z = re^{i\psi} = \frac{1}{N\langle q \rangle} \sum_{l=1}^{N} q_l e^{i\theta_l}, \tag{3.37}$$

where r is the coherence, and ψ is the average phase. One can write the imaginary part of the equation as

$$r\sin(\psi - \theta_j) = \frac{1}{N\langle q \rangle} \sum_{l=1}^{N} q_l \sin(\theta_l - \theta_j). \tag{3.38}$$
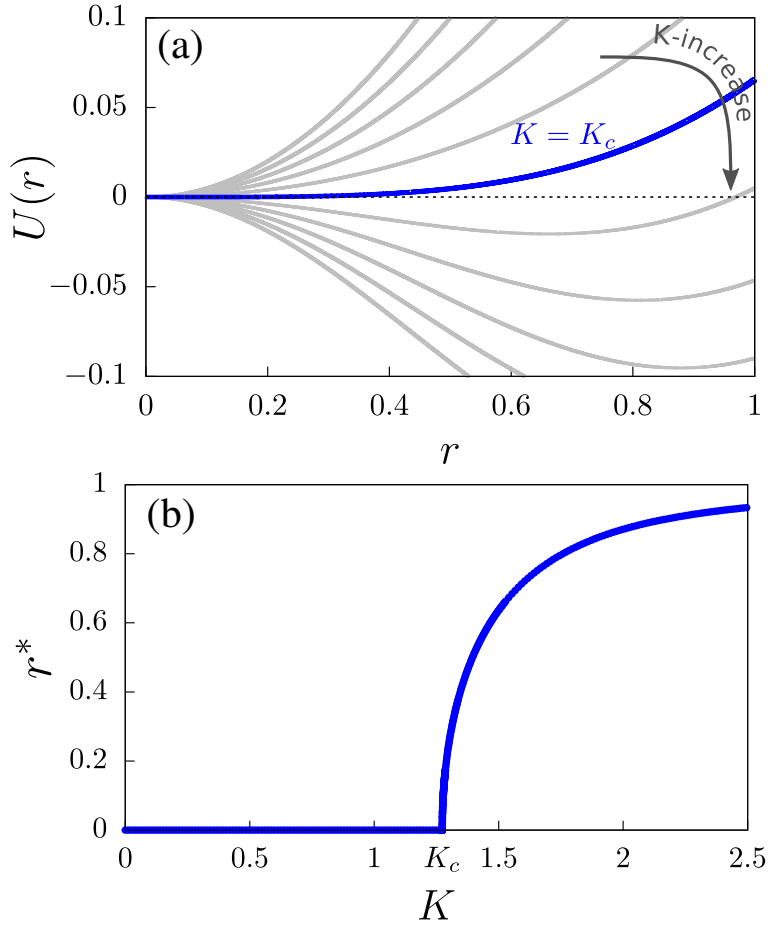
Figure 3.2: (a) Plot of ad hoc potential $U(r)$ given by Eq. (3.34) versus r. The potential exhibits a global minimum at $r = 0$ for $K \leq K_c$. For $K > K_c$, the position of the minimum increases continuously from 0 as K is increased. (b) Plot of the position of the minimum of $U(r)$, denoted as r^*, versus K for the Gaussian distribution $g(\omega)$. Here, a continuous transition occurs at K_c, and r^* follows the formula (3.35) above the critical point.

By substituting this into the Eq. (3.36), we obtain

$$\dot{\theta}_j - \Omega = \omega_j - \Omega - Kq_j r \sin(\theta_j - \psi). \tag{3.39}$$

where Ω is the group angular velocity defined as $\Omega = \dot{\psi}$. In the limit of $t \to \infty$ and $N \to \infty$, the system approaches to a steady state with a constant angular velocity such that $\dot{\Omega} = 0$. The solutions of Eq. (3.39) exhibit two types of behavior. Oscillators with $|\omega_j - \Omega| \leq Kq_j r$ are locked and have a stable solution taking the form of

$$\omega_j - \Omega = Kq_j r \sin(\theta_j - \psi). \tag{3.40}$$

On the other hand, oscillators with $|\omega_j - \Omega| > Kq_j r$ are drifting and never reach a steady state. And, for this model, the natural frequency of oscillator has a linear relation with the degree of respective node as follows,

$$\omega_j = aq_j + b. \tag{3.41}$$

Using a rotating frame $\omega_j \to \omega_j - b$, and rescaling the coupling constant, $K \to K/|a|$, we can simply reduce to the model with $a = 1$ and $b = 0$, i.e.,

$$\omega_j = q_j. \tag{3.42}$$

We will take this assumption for the following analysis. By dividing the system into locked and drifting oscillators, Eq. (3.37) can be written as

$$r = \frac{1}{N\langle q \rangle} \sum_{j=1}^{N} q_j e^{i(\theta_j - \psi)} \Theta \left(1 - \left| \frac{\omega_j - \Omega}{Krq_j} \right| \right)$$
$$+ \frac{1}{N\langle q \rangle} \sum_{j=1}^{N} q_j e^{i(\theta_j - \psi)} \Theta \left(\left| \frac{\omega_j - \Omega}{Krq_j} \right| - 1 \right). \tag{3.43}$$

In the thermodynamic limit, using Eq. (3.42), the term related to the order parameter of the locked oscillators becomes

$$\frac{1}{N}\sum_{j=1}^{N}q_j e^{i(\theta_j - \psi)}\Theta\left(1 - \left|\frac{\omega_j - \Omega}{Krq_j}\right|\right)$$

$$\simeq \int_1^\infty dq p(q)q\sqrt{1 - \left(\frac{q - \Omega}{Krq}\right)^2}\,\Theta\left(1 - \left|\frac{q - \Omega}{Krq}\right|\right)$$

$$+ i\int_1^\infty dq p(q)\frac{q - \Omega}{Kr}\Theta\left(1 - \left|\frac{q - \Omega}{Krq}\right|\right).$$ (3.44)

And the contribution of the drifting oscillators to the order parameter is given by

$$\frac{1}{N}\sum_{j=1}^{N}q_j e^{i(\theta_j - \psi)}\Theta\left(\left|\frac{\omega_j - \Omega}{Krq_j}\right| - 1\right)$$

$$\simeq i\int_1^\infty dq p(q)\frac{q - \Omega}{Kr}\left[1 - \sqrt{1 - \left(\frac{Krq}{q - \Omega}\right)^2}\right]\Theta\left(\left|\frac{q - \Omega}{Krq}\right| - 1\right).$$ (3.45)

Substituting Eqs. (3.44) and (3.45) into Eq. (3.43) and considering imaginary and real parts of the order parameter separately, one can obtain SCEs for two parameters, $\alpha \equiv rK$ and the group angular velocity, Ω, as

$$\langle q \rangle - \Omega = \int_1^\infty dq P_d(q)(q - \Omega)\sqrt{1 - \left(\frac{\alpha q}{q - \Omega}\right)^2}\,\Theta\left(\left|\frac{q - \Omega}{\alpha q}\right| - 1\right)$$ (3.46)

and

$$r = \frac{\alpha}{K}$$

$$= \frac{1}{\langle q \rangle}\int_1^\infty dq P_d(q)q\sqrt{1 - \left(\frac{q - \Omega}{\alpha q}\right)^2}\,\Theta\left(1 - \left|\frac{q - \Omega}{\alpha q}\right|\right)$$ (3.47)

where $\Theta(x)$ denotes the heaviside step function.

It is known that when the degree exponent λ is in the range $2 < \lambda < 3$, the synchronization transition is first-order [56]. For $2 < \lambda < 3$, by solving SCEs (3.46)

and (3.47) for α and Ω, one can evaluate the *ad hoc* potential. Because it is not as simple to calculate analytically, we first obtained the solution of $\Omega(\alpha)$ from Eq. (3.46) numerically and then solved for the SCE by substituting it into Eq. (3.47). As shown in Fig. 3.3(a), in this case, $U(r)$ exhibits a minimum at $r = 0$ when $K < K_{c1}$ and two minima at $r = 0$ and $r > 0$ when $K_{c1} < K < K_{c2}$, where K_{c1} and K_{c2} are defined in the caption of Fig. 3.3. As K is increased beyond K_c defined in the caption of Fig. 3.3, the minimum at $r > 0$ becomes a global minimum. As K is further increased to $K > K_{c2}$, the minimum at $r = 0$ no longer exists. This change in the potential shape as a function of K provides an intuitive understanding of the first-order synchronization transition as it appears for the first-order transition in the Landau theory for thermal systems. The order parameter behaves as shown in Fig. 3.3(b).

3.4.2 Dependence of interaction strength on the frequency

Another model exhibiting a first-order synchronization transition, the explosive synchronization model, was introduced in Ref. [67]. The model equation is written as

$$\dot{\theta}_j = \omega_j + \frac{K|\omega_j|}{\sum_{l=1}^{N} A_{jl}} \sum_{l=1}^{N} A_{jl} \sin(\theta_l - \theta_j), \tag{3.48}$$

where A_{jl} denotes an element of the adjacency matrix. The complex order parameter is defined as

$$Z = r e^{i\psi} = \frac{1}{N} \sum_{l=1}^{N} e^{i\theta_l} . \tag{3.49}$$

For all-to-all networks, Eq. (3.48) becomes

$$\dot{\theta}_j = \omega_j + \frac{K|\omega_j|}{N} \sum_{l=1}^{N} \sin(\theta_l - \theta_j) , \tag{3.50}$$
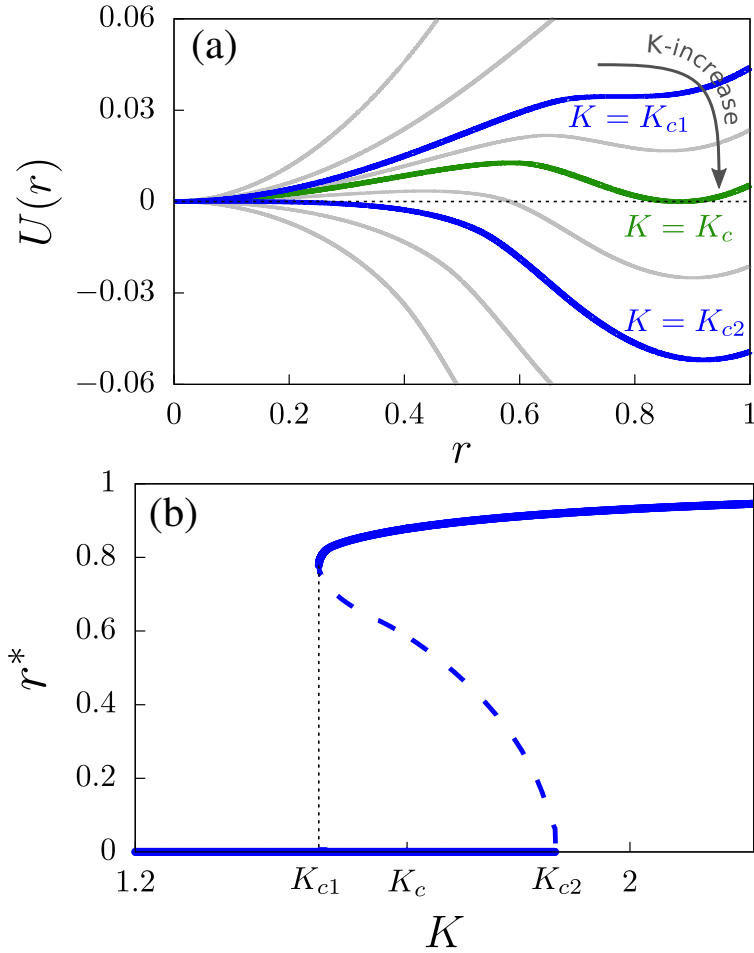
Figure 3.3: (a) *Ad hoc* potential shape $U(r)$ for different K values for the KE given by Eq. (3.36) on scale-free networks with degree exponent $\lambda = 2.8$. The potential exhibits only a minimum at $r^* = 0$ for $K < K_{c1}$. As K is increased, another local minimum is generated at $r^* > 0$ for $K > K_{c1}$. As K is further increased, $U(r)$ becomes smaller at this local minimum position; eventually, when $K = K_c$, $U(r)$ becomes zero at a certain $r^* > 0$. Thus, there exist two global minima at $r^* = 0$ and $r^* > 0$. The minimum at $r^* > 0$ becomes only a global minimum as K is further increased. By contrast, the minimum at $r = 0$ disappears when $K = K_{c2}$. (b) Position r^* at which $U(r)$ becomes either a local or a global minimum in (a) as a function of K. r^* exhibits a discontinuous transition in the region $[K_{c1}, K_{c2}]$. Blue dashed curve is the trajectory of the local maximum position of $U(r)$ as K is increased indicating an unstable curve.

and using Eq. (3.49), we get

$$\Delta\dot{\theta}_j = \omega_j - \Omega - K|\omega_j|r\sin(\Delta\theta_j)\,. \tag{3.51}$$

where Ω is the group angular velocity defined as $\Omega = \dot{\psi}$ and $\Delta\theta_j \equiv \theta_j - \psi$. $\{\omega_i\}$ has a distribution $g(\omega)$. As we can set $\Omega = 0$ for symmetric $g(\omega)$ in all-to-all networks, one can then obtain the equation

$$\Delta\dot{\theta}_j = \omega_j - K|\omega_j|r\sin(\Delta\theta_j)\,. \tag{3.52}$$

When all the oscillators are phase-locked, i.e., $\Delta\dot{\theta}_j = 0$ for all j, the solution is obtained as

$$\Delta\theta_j = \begin{cases} \arcsin\left(\frac{1}{Kr}\right) & \text{for} \quad \omega_j > 0 \\ \arcsin\left(-\frac{1}{Kr}\right) & \text{for} \quad \omega_j < 0\,. \end{cases} \tag{3.53}$$

From Eq. (3.49), the SCE can be written as

$$\begin{aligned} r =& \frac{1}{2}\int_{-\pi}^{\pi} d\theta \int_{-\infty}^{\infty} d\omega g(\omega)\cos\theta\,\Theta\left(\omega - \left|\frac{\omega}{Kr}\right|\right) \times \\ & \left(\delta\left(\theta - \arcsin\left(\frac{1}{Kr}\right)\right) + \delta\left(\theta - \arcsin\left(-\frac{1}{Kr}\right)\right)\right) \\ =& \sqrt{1 - \left(\frac{1}{Kr}\right)^2}\,\Theta\left(1 - \left|\frac{1}{Kr}\right|\right)\,. \end{aligned} \tag{3.54}$$

Hence, $f(r)$ is determined as follows:

$$f(r) = \begin{cases} 0 & \text{for} \quad Kr \le 1 \\ \sqrt{1 - \left(\frac{1}{Kr}\right)^2} & \text{for} \quad Kr > 1\,. \end{cases} \tag{3.55}$$

Accordingly, $U(r)$ is obtained as follows:

$$U(r) = \begin{cases} \frac{r^2}{2} & \text{for} \quad r \leq \frac{1}{K} \\ \frac{r^2}{2} - r\sqrt{1 - \left(\frac{1}{Kr}\right)^2} - \frac{2}{K}\arctan\left(\sqrt{\frac{Kr+1}{Kr-1}}\right) & \text{for} \quad r > \frac{1}{K}. \end{cases} \tag{3.56}$$

Fig. 3.4 shows a discontinuous transition at $K = K_{c1}$, from which a minimum of $U(r)$ at $r > 0$ starts to develop. At K_c, the minimum of $U(r)$ becomes zero for $r^* > 0$. As K is increased further, this minimum at $r^* > 0$ is a global minimum. Note that unlike the case in the previous subsection, K_{c2}, at which the second derivative of $U(r)$ with respect to r at $r = 0$ becomes zero, does not exist. It is always positive as long as K is finite. Therefore, there is no hysteresis curve. In the limit $K \to \infty$, the minimum at $r^* > 0$ becomes the dominant solution, and the minimum at $r = 0$ disappears.

3.5   Hybrid synchronization transition

3.5.1   Uniform distribution $g(\omega)$

We consider the *ad hoc* potential for the uniform distribution $g(\omega)$ given by

$$g(\omega) = \begin{cases} \frac{1}{2\gamma} & \text{for} \quad |\omega| \leq \gamma \\ 0 & \text{for} \quad |\omega| > \gamma \end{cases}, \tag{3.57}$$

where γ is the half-width of the distribution. Thus, $f(r)$ becomes

$$f(r) = \begin{cases} \frac{K}{K_c}r & \text{for} \quad Kr \leq \gamma \\ \frac{1}{2}\sqrt{1 - \frac{\gamma^2}{K^2 r^2}} + \frac{Kr}{2\gamma}\arcsin\left(\frac{\gamma}{Kr}\right) & \text{for} \quad Kr > \gamma \end{cases}, \tag{3.58}$$
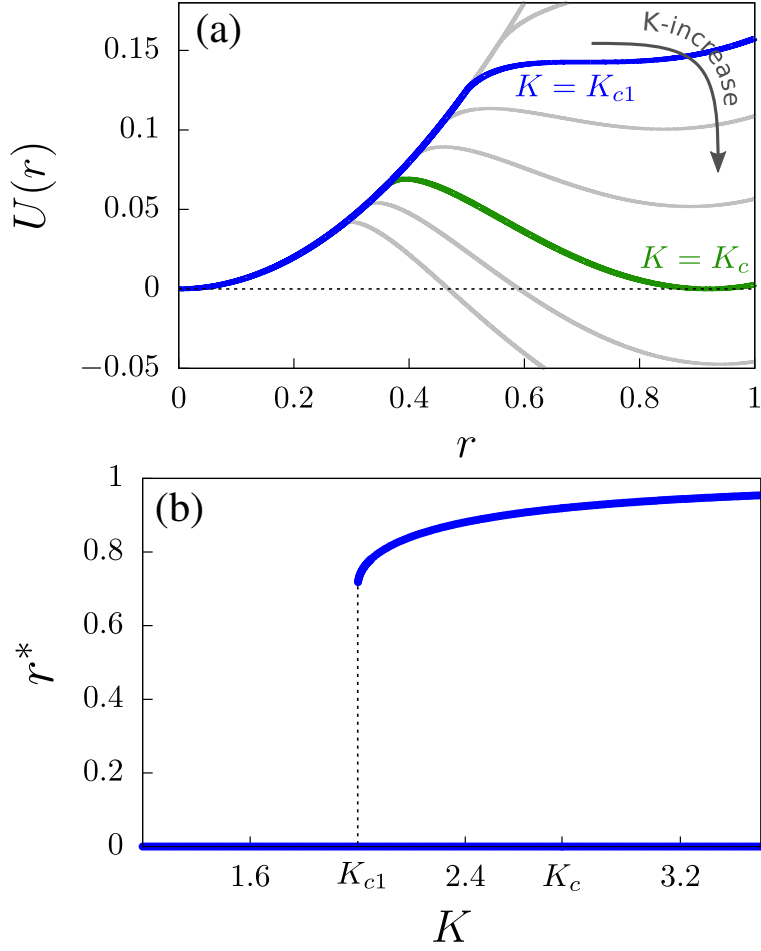
Figure 3.4: (a) *Ad hoc* potential $U(r)$ given in Eq. (3.56). The potential exhibits one minimum at $r = 0$ for $K < K_{c1}$. As K is increased, local minimum develops at $r^* > 0$ for $K > K_{c1}$, but it is not a global minimum yet. As K is increased further, $U(r)$ at the minimum point becomes smaller. When $K = K_c$, $U(r)$ becomes zero at both $r = 0$ and $r^* > 0$. So $U(r)$ at $r^* > 0$ reaches a global minimum as K is further increased. Note that minimum of $U(r)$ at $r = 0$ remains as long as K is finite. (b) Values of r^* versus K.

where K_c is the transition point in the thermodynamic limit, determined by $K_c r_c = \gamma$ [34]. Explicitly, $K_c = 4\gamma/\pi$, and $r_c = \pi/4$. The potential is determined as

$$
U(r) = \begin{cases} \frac{K_c - K}{2K_c} r^2 & \text{for} \quad r \le \frac{\gamma}{K} \\ \int_0^r \left(r' - \frac{1}{2}\sqrt{1 - \frac{\gamma^2}{K^2 r'^2}} - \frac{Kr'}{2\gamma} \arcsin\left(\frac{\gamma}{Kr'}\right) \right) dr' & \text{for} \quad r > \frac{\gamma}{K} \end{cases} . \quad (3.59)
$$

Numerical evaluations of $U(r)$ for arbitrary values of K are plotted in Fig. 3.5(a). For $K < K_c$, the coefficient of r^2 is positive for $r \le \gamma/K$ in Eq. (3.59), so the solution at $r = 0$ is stable. As K is increased, the coefficient approaches zero, and the potential becomes flatter near the origin. At $K = K_c$, the coefficient becomes zero, and a plateau is formed across the range $r \le \gamma/K_c = r_c$, as shown in Fig. 3.5(a). When $K > K_c$, the coefficient is negative, and thus the solution $r = 0$ becomes unstable. In this case, a stable minimum emerges in the region $r > r_c$.

The minimum of the potential in the region $r > r_c$ can be calculated by performing an expansion above both K_c and r_c as

$$
K = K_c + \epsilon \quad \text{and} \quad r = r_c + \delta . \quad (3.60)
$$

By substituting these expressions into Eq. (3.59) and taking the limit ϵ and $\delta \to 0$, we obtain the potential for $r > \gamma/K$,

$$
U(r) = -\frac{\pi^2 \epsilon}{16\gamma} \delta + \frac{32\sqrt{2}}{15\pi^{3/2}} \delta^{5/2} + \mathcal{O}(\delta^3) \quad (3.61)
$$

Minimizing the potential (or, $dU(r)/dr = 0$), we obtain the hybrid synchronization transition behavior of the order parameter as

$$
r - r_c = \left(\frac{9\pi^7}{2^{17}\gamma^2} \right)^{1/3} (K - K_c)^{2/3} . \quad (3.62)
$$

The stable fixed point of the order parameter follows this relation, which is consistent
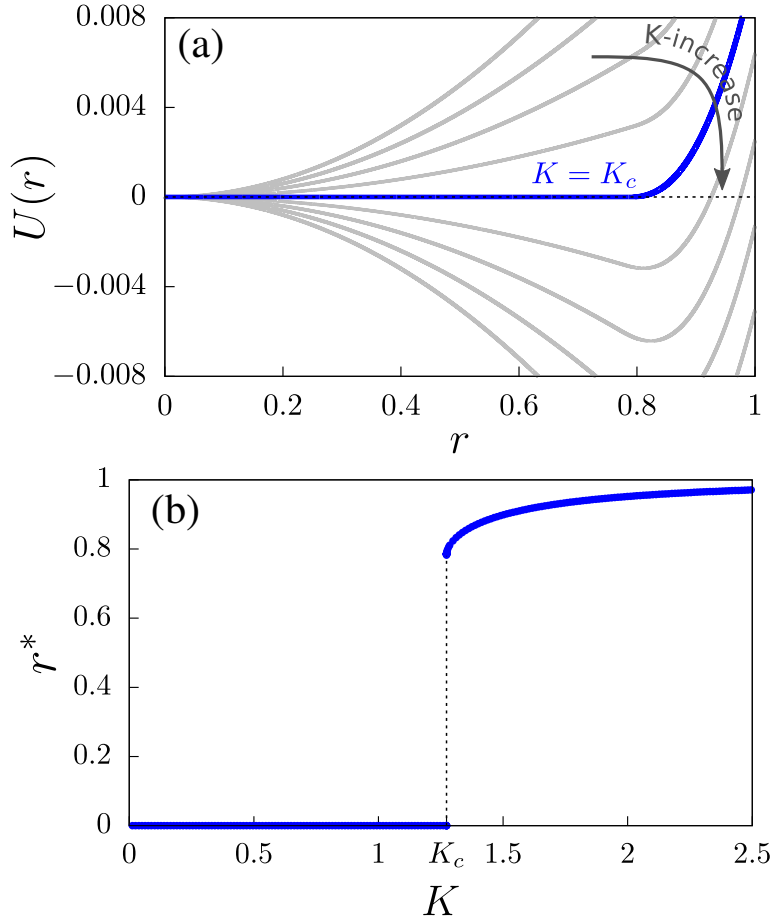
Figure 3.5: (a) Plot of *ad hoc* potential $U(r)$ as a function of the order parameter r for the case (3.59). The potential exhibits a global minimum at $r = 0$ for $K < K_c$ and forms a plateau at $K = K_c$ in the region $r \in [0, r_c = \pi/4]$. When $K > K_c$, a global minimum appears above $r_c = \pi/4$, and it increases gradually as K is increased further. (b) Plot of r^* values, at which global minima of $U(r)$ are positioned for given Ks, as a function of K for the uniform distribution $g(\omega)$. r^* undergoes a discontinuous transition at $K = K_c$ and follows Eq. (3.62) above the critical point K_c.

with the result obtained in Ref. [34]. Fig. 3.5(b) shows that the position of the minimum r^* exhibits a discontinuous jump at the critical value K_c. We remark that the potential $U(r)$ satisfies the Landau criterion for the HPT in thermal systems given in Eq. (3.2).

3.5.2 Degree-frequency correlation on scale-free networks with $\lambda = 3$

Here we consider the Kuramoto dynamics on scale-free networks that exhibit a power-law degree distribution $P_d(q) \sim q^{-\lambda}$, where q denotes the degree, for $\lambda = 3$. In this case, the KE is known to exhibit a hybrid synchronization transition [55, 56]. The KE is written as Eq. (3.36). In particular, the condition $\omega_i = q_i$, at which a hybrid synchronization transition occurs, is given.

The SCE for a scale-free network with $\lambda = 3$ was derived in the appendix of Ref. [56]:

$$r = \frac{1}{2} \int_{-1}^{1} dx \sqrt{1 - \left(\frac{x}{\alpha}\right)^2} \, \Theta\left(1 - \left|\frac{x}{\alpha}\right|\right) . \tag{3.63}$$

By using $\alpha = rK$, the equation can be written as

$$r = \begin{cases} \frac{K}{K_c} r & \text{for} \quad Kr \leq 1 \\ \frac{1}{2}\sqrt{1 - \frac{1}{K^2 r^2}} + \frac{Kr}{2} \arcsin\left(\frac{1}{Kr}\right) & \text{for} \quad Kr > 1 \end{cases} , \tag{3.64}$$

where $K_c = 4/\pi$, and $r_c = \pi/4$. This result is reduced to the same as that for the uniform distribution of $g(\omega)$ in all-to-all connected networks discussed in Sec. 3.5.1. Therefore, one can obtain exactly the same potential $U(r)$ as that given for the uniform frequency distribution $\gamma = 1$.

3.5.3 Flat distribution with exponential tails

In Ref. [57], the uniform natural frequency distribution was extended by adding tails on each side as follows:

$$
g(\omega) = \begin{cases} g(0) & \text{for} \quad |\omega| \leq \alpha \\ g(0)[1 - c(|\omega| - \alpha)^m] & \text{for} \quad \alpha \leq |\omega| \leq \alpha + c^{-\frac{1}{m}} \\ 0 & \text{otherwise} \end{cases} \tag{3.65}
$$

where c is a positive constant, and $g(0)$ is given by

$$
g(0) = \frac{1}{2} \frac{1}{\alpha + [m/(m+1)]c^{-1/m}} \tag{3.66}
$$

according to the normalization condition. For this distribution, we obtain $f(r)$ as

$$
f(r) = \frac{K}{K_c} r - h(r) \tag{3.67}
$$

where

$$
h(r) = \begin{cases} 0 & \text{for} \quad Kr \leq \alpha \\ 2g(0)c \int_\alpha^{Kr} \left(\sqrt{1 - \frac{\omega^2}{K^2 r^2}} (\omega - \alpha)^m \right) d\omega & \text{for} \quad \alpha < Kr \leq \alpha + c^{-\frac{1}{m}} \\ 2g(0)c \int_\alpha^{\alpha + c^{-\frac{1}{m}}} \left(\sqrt{1 - \frac{\omega^2}{K^2 r^2}} (\omega - \alpha)^m \right) d\omega & \text{for} \quad \alpha + c^{-\frac{1}{m}} < Kr \end{cases}
$$

$$\tag{3.68}$$

and $K_c = 2/[\pi g(0)]$. $U(r)$ was also calculated numerically using Eq. (3.67), as shown in Fig. 3.6(a). As in previous sections, plateau region of $g(\omega)$ leads the system to exhibit a hybrid synchronization transition with a flat potential at the critical point. A

calculation of r^* for the potential confirms that

$$r - r_c \sim (K - K_c)^{2/(2m+3)}, \tag{3.69}$$

which was studied in Ref. [57]. When $m = 0$, the exponent β becomes $2/3$, which is consistent with that of the uniform distribution.

3.5.4 Flat distribution with power-law tails

We consider the Lorentzian distribution with an upper cutoff defined as

$$g(\omega) = \begin{cases} g(0) & |\omega| \leq \alpha \\ \frac{1}{\mathcal{N}} \frac{\gamma/\pi}{\gamma^2 + \omega^2} & |\omega| > \alpha \end{cases}, \tag{3.70}$$

where the normalization is calculated as

$$\mathcal{N} = 1 - \frac{2}{\pi} \arctan\left(\frac{\alpha}{\gamma}\right) + \frac{2\gamma\alpha}{\pi\left(\gamma^2 + \alpha^2\right)}, \tag{3.71}$$

and

$$g(0) = \frac{1}{\mathcal{N}} \frac{\gamma/\pi}{\gamma^2 + \alpha^2}. \tag{3.72}$$

$g(\omega)$ is thus flat in $(-\alpha, \alpha)$ and has a long-decay tail $\sim |\omega|^{-2}$ on each side. We find a universal hybrid critical exponent $\beta = 2/5$, together with a plateau of $U(r)$ similar to that in Fig. 3.6(a), for this distribution and for any flat distribution with power-law tails.

Now, we consider a $g(\omega)$ that is flat in the interval $[-\alpha, \alpha]$ and decays in a power-
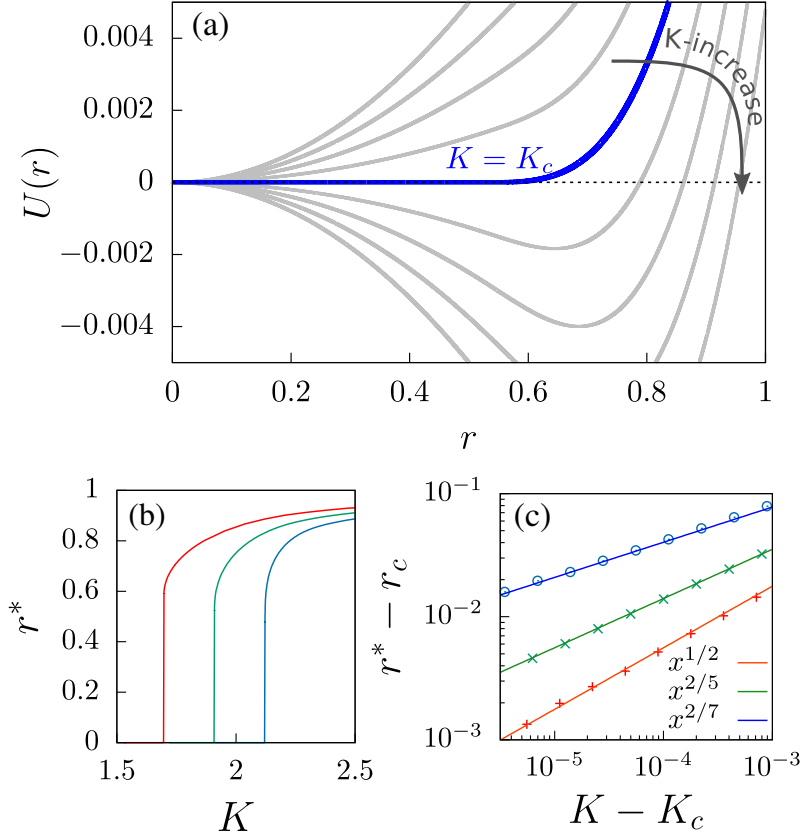
Figure 3.6: (a) Plot of *ad hoc* potential $U(r)$ as a function of r for the case (3.67) with $m = 1$. The potential exhibits a plateau in the region $[0, r_c]$. (b) Plot of r^* values at which minima of $U(r)$ are positioned as a function of K for various sets of (m, α). From the left, the curves are for $(m, \alpha) = (0.5, 1)$ (in red), $(1, 1)$ (in green), and $(2, 1)$ (in blue). For all cases, r^* undergoes a discontinuous transition at the critical point K_c. (c) Above K_c, the exponent β of the order parameter is measured for $m = 0.5$ (red), 1 (green), and 2 (blue). The straight lines are drawn according to the theoretical formula [Eq. (3.69)] for each case.
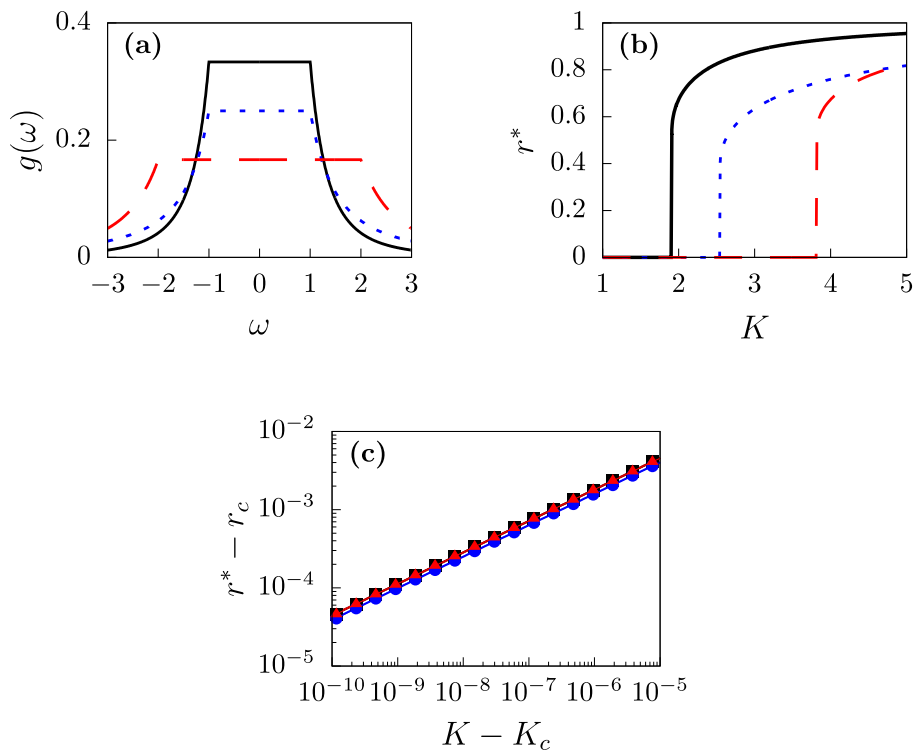
Figure 3.7: (a) Flat-with-tails distribution for various values of (α, m): solid, $(1, 3)$; dotted, $(1, 2)$; and dashed, $(2, 3)$. (b) Order parameter curve obtained using the SCE. (c) $\beta = 0.40$ is measured for all cases.

law manner, $\sim |\omega|^{-m}$ $(m > 1)$, for $\omega > \alpha$.

$$g(\omega) = \begin{cases} g(0), & |\omega| \leq \alpha \\ \frac{g(0)\alpha^m}{|\omega|^m}, & |\omega| > \alpha \end{cases}, \tag{3.73}$$

where

$$g(0) = \frac{m-1}{2\alpha m} \tag{3.74}$$

by the normalization condition, $\int g(\omega)d\omega = 1$, which is depicted in Fig. 3.7(a). For $Kr \geq \alpha$, the SCE is written as

$$\begin{aligned} r =& Krg(0) \int_{-\alpha/(Kr)}^{\alpha/(Kr)} dx \sqrt{1-x^2} \\ &+ \frac{2g(0)\alpha^m}{(Kr)^{m-1}} \int_{\alpha/(Kr)}^{1} x^{-m} \sqrt{1-x^2} dx \\ =& 2Krg(0) \int_{0}^{\theta_0} d\theta \cos^2 \theta \\ &+ \frac{2g(0)\alpha^m}{(Kr)^{m-1}} \int_{\sin^2 \theta_0}^{1} \frac{1}{2} y^{-\frac{m+1}{2}} (1-y)^{\frac{1}{2}} dy, \end{aligned} \tag{3.75}$$

where $\alpha/Kr \equiv \sin \theta_0$. Notice that at $\theta_0 = \pi/2$, the SCE shows that the order parameter jumps by as much as $r_c = \pi g(0)\alpha/2$ at $K_c = 2/[\pi g(0)]$.

Using the SCE, we obtain that

$$r - r_c \sim \frac{\alpha}{2K_c} \left(\frac{15\pi}{4mK_c} \right)^{2/5} (K - K_c)^{2/5} \tag{3.76}$$

within the leading order as shown in Fig. 3.7(b) and (c). Therefore, the transition is hybrid, and the associated exponent is $\beta = 2/5$, which differs from the value of $\beta = 2/3$ for the uniform distribution. Notice that in the limit $m \to \infty$, the second term of Eq. (3.75) vanishes because $\sin \theta_0 < 1$, and thus $\beta = 2/3$ is recovered.

3.6 Summary

We reconsidered the hybrid synchronization transitions arising in the KM by constructing an *ad hoc* potential analogous to the Landau free energy conventionally used in thermal equilibrium systems. In particular, we considered KEs with several different types of natural frequency distributions which generate hybrid synchronization transitions. From the SCEs of the KMs, we constructed *ad hoc* potentials and showed that the *ad hoc* potential in the thermodynamic limit satisfies the criterion of the Landau theory for an HPT established for thermal systems [42]. Moreover, we applied the proposed methodology to the Kuramoto systems with various natural frequency distributions and coupling strengths for diverse types of synchronization transitions such as second-order, first-order, and hybrid, transitions. Consequently, this approach could be useful for determining transition types of synchronizations and understanding transition properties for other Kuramoto-type models.

Chapter 4

Machine learning approaches to coupled oscillators

Incorporating machine learning (ML) approaches, recent progressive advances have been achieved in diverse fields of science and engineering. In particular, here we focus on the dynamical systems that exhibit synchronization transitions and chaotic dynamical patterns. Chaotic behaviors are observed in a variety of systems in nature such as cardiac cycle, neuroscience, climate and stock market. The utmost interests in such systems are to explore the chaotic signals for predicting dynamical evolution. To achieve this, in a traditional approach, once an appropriate model to the current chaotic pattern is set up and then dynamical evolution is predicted by simulating the model. However, ML approach using reservoir computing [19–21] identifies underlying factors of the current chaotic behavior and then provides so-called model-free prediction of the dynamical evolution [22–29].

Chaotic patterns are often created by the cooperation of multiple elements in the system. It may be necessary to figure out how these elements are interwoven and cooperated among them [70–72]. For instance, in neurophysiology, researches on classifying and capturing physiological events such as seizure, stroke, or headache have been progressed by identifying the correlations between EEG signals. Recently, ML approaches accelerate the progress of identifying the cooperation among neuronal components [73–76].

Synchronization of the chaotic patterns created by multiple elements in such neural systems may be a signal of stable state. Hence, a phase transition from a disordered state to an ordered state naturally arises as an interesting issue in such complex

systems. Along with the recent advance of ML algorithms for the studies of phase transitions in equilibrium and nonequilibrium systems such as Ising models and percolation [12–18], it is interesting to consider the synchronization transition using the ML approach.

As a model for describing the behavior of coupled oscillators, the Kuramoto model [30, 31] is a suitable candidate for the platform to deal with above three issues at the same time. The system exhibits not only the chaotic dynamics provoked by non-linear couplings between oscillators, but also different types of the synchronization transition depending on underlying connection topologies or variations on the model [34, 56, 57, 77, 78]. Despite the rich properties of the Kuramoto oscillators, the applications of machine learning approaches on this system has not yet been worked out thoroughly.

Here, we examine the Kuramoto model through the data-driven approaches by focusing on issues mentioned above. We adopt several machine learning models for finding and predicting the underlying properties of the Kuramoto system from the data obtained through numerical simulations. Along with the confirmation of consistency with results already demonstrated in previous studies for the Kuramoto model, we identify that this approach to the coupled oscillators is applicable to the real-world system by establishing plausible tasks and reporting successful performance.

4.1   Machine learning models

Before demonstrating the tasks performed, we first introduce the machine learning models adopted in this dissertation. All the models used here are a class of artificial neural networks which mimic the human brain through a set of algorithms operated by a collection of artificial neurons.
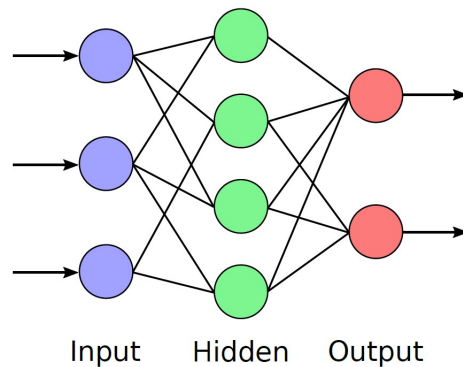
Figure 4.1: Schematic illustration of the feed-forward neural network. Information of input is always propagated in one direction and never moves backward.

4.1.1 Feed-forward neural network

As one class of the artificial neural network, the feed-forward neural networks (FNNs) are quintessential deep learning models that were invented as the first type of artificial neural networks. When the inputs are fed into the input layer, FNNs propagate the input information from one layer to the next layer in one direction only, without forming a cycle structure as illustrated in Fig. 4.1. Neurons in one layer are connected with neurons in the next layer, and all such connections between two consecutive layers are represented by the weight matrix $\mathbf{W}$. For a given input of $\mathbf{x}$, states of neurons $\mathbf{y}$ are updated by the equation

$$\mathbf{y} = f(\mathbf{W}\mathbf{x} + \mathbf{b}) \tag{4.1}$$

where $\mathbf{b}$ denotes the bias exerted on neurons and $f(\mathbf{x})$ is the activation function. In general, non-linear functions such as sigmoid, hyperbolic tangent (tanh), rectified linear unit (ReLU) and softmax are used for the activation function and one can choose different form of activation function for each layers. For FNN, neuron states act as the input in subsequent layer until it reaches to the final output layer.

4.1.2 Fully-connected neural network

Fully-connected neural networks (FCNs) consisting of fully-connected layers (FL) only is a basic structure of feed-forward neural network (FNN). Neurons in each FL are connected with all input components in the precedent layer. The major advantage of FCNs is independence in structural information of input data which means that any special assumptions about the input is not necessary.

4.1.3 Convolutional neural network

By combining FLs, convolutional layers (CL), and pooling layers, one can construct a convolutional neural networks (CNNs). By passing through CL, the input data is transformed by filters in CL, which are useful for maintaining spatial information and identifying the spatial patterns of the input such as translational symmetry and rotational symmetry. These networks are applied for image classification, image and video recognition, objects detection, and so on.

4.1.4 Recurrent neural network

As another deep learning model for dealing with the sequential data, recurrent neural network (RNN) has recurrent layers with cyclic connection topology, which leads to distinction from the FCN. This structure of RNN resembles biological brain modules which also exhibits recurrent connection pathways. These cyclic connections of RNNs allow to have applications in natural language processing, image captioning, machine translation, predicting time sequential data such as stock market, weather forecast, and so on.

4.1.5 Reservoir computing

Reservoir computing (RC), a class of recurrent neural networks, is composed of an input layer, an output layer and a reservoir layer which connects between input and
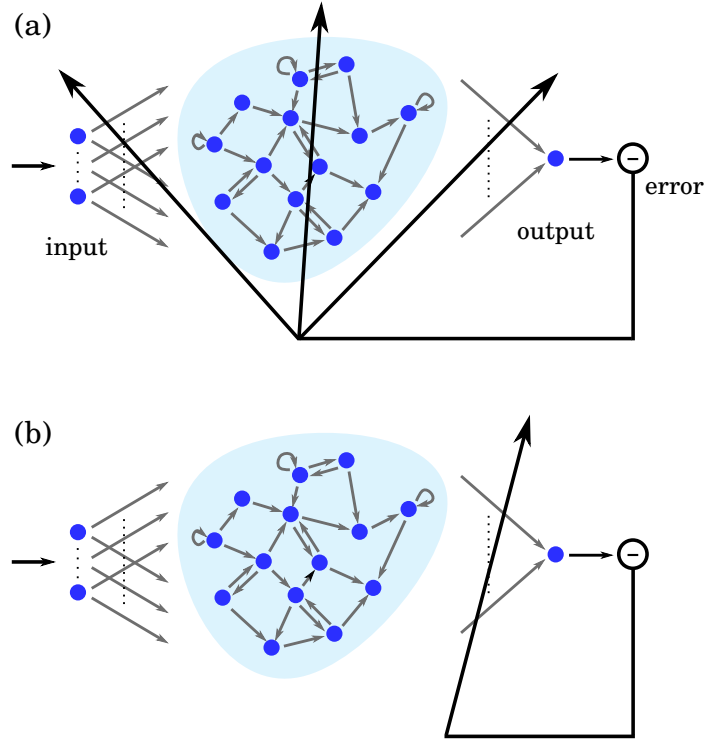
Figure 4.2: Schematic illustration of (a) the RNN training and (b) reservoir computing. For a traditional RNN training methods, all elements in input-to-hidden weight, internal weight of hidden, and hidden-to-output weight are adapted for training, while only elements in the hidden-to-output weight are updated for reservoir computing.

output layers. And neurons in the reservoir layer has internal links including the self-loop as in the recurrent layer.

In this thesis, as the input vector $\mathbf{u}(t)$ goes in, the state vector $\mathbf{r}$ is updated according to the equation

$$\mathbf{r}(t+1) = (1-\lambda)\mathbf{r}(t) + \lambda \tanh\left(\mathbf{A}\mathbf{r}(t) + \mathbf{W}_{\text{in}}\begin{bmatrix} b_{\text{in}} \\ \mathbf{u}(t) \end{bmatrix}\right) \qquad (4.2)$$

where $\mathbf{A}$ is the weighted adjacency matrix of the reservoir network, $\mathbf{W}_{\text{in}}$ is the random matrix which maps an input vector $\mathbf{u}(t)$ into a state vector $\mathbf{r}(t)$, λ is the leaking rate,

Table 4.1: Symbols for machine learning models.

Symbol	Model
FNN	Feed-forward neural network
FCN	Fully-connected neural network
CNN	Convolutional neural network
RNN	Recurrent neural network
RC	Reservoir computing

and b_{in} is the bias term. And the output vector $\mathbf{y}(t)$ is determined by a linear function

$$\mathbf{y}(t) = \mathbf{W}_{\text{out}} \begin{bmatrix} b_{\text{out}} \\ \mathbf{u}(t) \\ \mathbf{r}(t) \end{bmatrix} \tag{4.3}$$

where $\mathbf{W}_{\text{out}}$ denotes the output matrix which maps a reservoir state into a output vector for given bias of b_{out}.

4.2 Supervised learning

Although a variety of structures can be designed, FNN $\mathcal{F}$ is determined by model parameters $\{w\}$ including the weight and the bias. The model produces the output $\mathbf{y}$ for a given input $\mathbf{x}$, which is expressed as the functional form

$$\mathbf{y} = \mathcal{F}\left[\{w\}\right](\mathbf{x}). \tag{4.4}$$

For supervised learning, model parameter $\{w\}$ of FNN is adjusted for the output $\mathbf{y}$ to be close to the desired output $\bar{\mathbf{y}}$ according to the given input $\mathbf{x}$ of a training dataset. To minimize the difference between $\mathbf{y}$ and $\bar{\mathbf{y}}$, or the cost (loss, energy) function E, determined by the root mean square, the mean absolute, or the cross entropy, model

parameter w is tuned through the gradient descent method which is the fundamental method for training FNN including RNN :

$$w_{\text{new}} = w - \alpha \partial_w E(\mathbf{y}, \bar{\mathbf{y}}) \qquad (4.5)$$

where α is the learning rate. With random initial values of $\{w\}$, the well-trained FNN is obtained by repeating the learning process of Eq. (4.5) [79].

In the case of RC, when the updated state vector $\mathbf{r}$ of the reservoir is given through Eq. (4.2), the output weights $\mathbf{W}_{\text{out}}$ are determined by the equation [21, 27]

$$\mathbf{W}_{\text{out}} = \mathbf{Y}\mathbf{X}^\top (\mathbf{X}\mathbf{X}^\top + \gamma \mathbb{I})^{-1} \qquad (4.6)$$

where γ is the ridge regularization parameter and $\mathbb{I}$ is an identity matrix. And $\mathbf{X}$ and $\mathbf{Y}$ are the collecting matrix of state vector $[b_{out}, \mathbf{u}(t), \mathbf{r}(t)]^\top$ and the desired output vector $\bar{\mathbf{y}}(t)$ in the training process, respectively. While the classical RNN adopts the back-propagation through time which is based on a gradient descent method for recurrent layers, for RC, $\mathbf{A}$ and $\mathbf{W}_{\text{in}}$ are randomly created and unchanged during training, and only the output weights $\mathbf{W}_{\text{out}}$ are computed.

4.3 Finding the coupling strength

Assuming a situation where any concrete form of dynamics is unavailable, we investigate that how accurate values of underlying coupling strengths can be obtained by the neural network from the data for the dynamics of the order parameter, $r(t)$, only. As phases of oscillators and the corresponding order parameter proceed according to Eq. (2.1), $r(t)$ is obtained for given value of J. Once the generated time series of the order parameter for given J goes into the neural network as an input, learning process is carried out by a model as shown in Fig. 4.3. Taking the trained neural network, we tested for other generated 10^4 sets of $r(t)$ with randomly chosen J in the range of
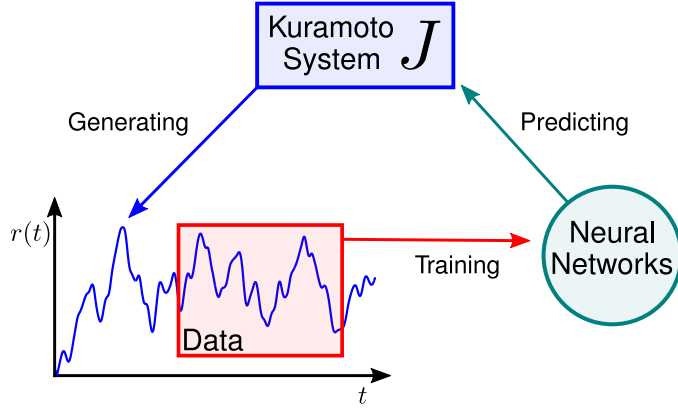
Figure 4.3: Schematic illustration of the process carried out for finding the coupling strength.

$[0, 2]$.

Here, we produced configurations of $r(t)$ for the system of $N = 1000$ using the fourth-order Runge-Kutta method with a discrete time step $\delta t = 0.05$ up to a total of 2×10^3 time steps. The sets of natural frequencies, $\{\omega_i\}$, are selected randomly from the normal distribution given in Eq. (2.5) and initial phases, $\{\theta_i(t = 0)\}$, are chosen randomly from the range of $[0, 2\pi]$. We generate 2×10^4 training datasets of $r(t)$ for each value of $J \in [0.02, 2]$ with an interval of $\delta J = 0.02$.

As shown in Fig. 4.4(a), output values, J_{ML}, using RNNs fits well with exact values of J in supercritical ($J > 1$) and subcritical ($J < 1$) regions both. To evaluate how accurate values of J_{ML} are obtained, we calculated the Pearson correlation coefficient and the root mean square (RMS) error, and obtained 0.9921 and 0.0727, respectively. By measuring the mean μ_{ML} and the standard deviation σ_{ML} with varying actual coupling strength J, one can confirm that μ_{ML} is close to J in both super and subcritical regions, while the difference in standard deviations between two regions appears as depicted in Fig. 4.4(b). Although outputs are scattered broader in the region $J < 1$ than $J > 1$, the tendency following the correct value of J provides the fact that the neural network can distinguish configurations of $r(t)$ and identify corresponding

coupling strengths.

As the result obtained can lead one to wonder what information is extracted from the data by the neural network during training, we also compare the result with the estimation of J through the calculation for values of the order parameter to support the quality of the result and investigate the learning of the neural network. Here, we used time averaged value of the order parameter, $\bar{r}$, over final 1000 steps of each training datasets and calculated mean, $\langle \bar{r} \rangle$, over all configurations with same value of J. As $\langle \bar{r} \rangle$ increases monotonically with J as shown in Fig. 4.4(c), one can estimate the coupling strength for each test datasets by obtaining $\bar{r}$ and comparing with Fig. 4.4(c). From results of this estimation, denoted as $J_{\langle \bar{r} \rangle}$, their mean $\mu_{\langle \bar{r} \rangle}$ and standard deviation $\sigma_{\langle \bar{r} \rangle}$ are plotted in Fig. 4.4(a) and (b) for comparison with μ_{ML} and σ_{ML}. One can find that $J_{\langle \bar{r} \rangle}$ is distributed in broader range than J_{ML} in subcritical region as the Pearson correlation and the RMS error with 0.9870 and 0.0945 are obtained respectively for the case of $J_{\langle \bar{r} \rangle}$. And the larger value of $\sigma_{\langle \bar{r} \rangle}$ than σ_{ML} in $J < 1$ region demonstrates the better quality of the result achieved by the machine learning.

In addition, narrow deviation in supercritical region is observed for the correlation between J_{ML} and $J_{\langle \bar{r} \rangle}$ as depicted in Fig. 4.4(d) while the deviation in subcritical region is broader. This implies that the information of the time-averaged value is dominant for the neural network to evaluate the coupling strength in supercritical region, while it can evaluate through acquisition of more information than the time-averaged value from the data of $r(t)$ in subcritical region, as smaller deviations for the machine learning case are shown in Fig. 4.4(b).

We performed the estimation of the coupling strength for the case of uniform natural frequency distribution, where the hybrid synchronization transition occurs, as well. As shown in Fig. 4.5(a), estimations for both cases of the Gaussian distribution, J_g, and the uniform distribution, J_u exhibit outstanding accurate. For the result in the subcritical region, the standard deviation of estimations in the uniform distribution case is similar to the case of Gaussian distribution as depicted in Fig. 4.5(b), but an

evident difference between two standard deviations in the supercritical region is observed. Since all oscillators are phase-locked in the supercritical region for the case of uniform distribution, which leads to absence of time fluctuation in the order parameter (zero susceptibility), it is easier to distinguish and identify the value of coupling strength and thus, we obtain smaller value of σ_{u} than σ_{g}.

4.4 Finding the synchronized state

As the machine learning of thermodynamical phase transitions for diverse systems have been paid much attention in previous studies [12–14, 16–18], we also performed another study of machine learning model for the phase transition of the Kuramoto system. Here, taking the neural network, we classify phase snapshots of all oscillators in the steady state into subcritical and supercritical regimes and eventually find the critical point of the system.

Again, the fourth-order Runge-Kutta method with a time step of $\delta t = 0.01$ is adopted for generating 2×10^4 datasets of $\{\theta_i\}$ for each values of system size N and $J \in [0.01, 2.20]$ with $\delta J = 0.01$. As in the previous section, for each configuration, natural frequencies and initial phases are selected randomly from the normal distribution and the uniform distribution, respectively. To avoid any transient behavior, we collect snapshots of phases, $\{\theta_i\}$, after the first 10^6 steps. For training datasets, each snapshots are labelled through one-hot encoding where configurations obtained in supercritical region of $J \in [0.01, 0.6]$ are encoded as $(0, 1)$ and ones in supercritical region of $J \in [1.6, 2.2]$ are encoded as $(1, 0)$. And we used data preprocessing by taking $\cos \theta_i$ and $\sin \theta_i$ for each phases as an input, due to the cyclic feature of θ_i which contains the 2π periodicity.

Constructing the FCN, we train the machine with labelled snapshots of N phases $\{\cos \theta_i, \sin \theta_i\}$. When the network is optimized after the training, generated snapshots in whole region of J goes in as an input at the test stage.

The trained neural network produces two outputs representing predictabilities for
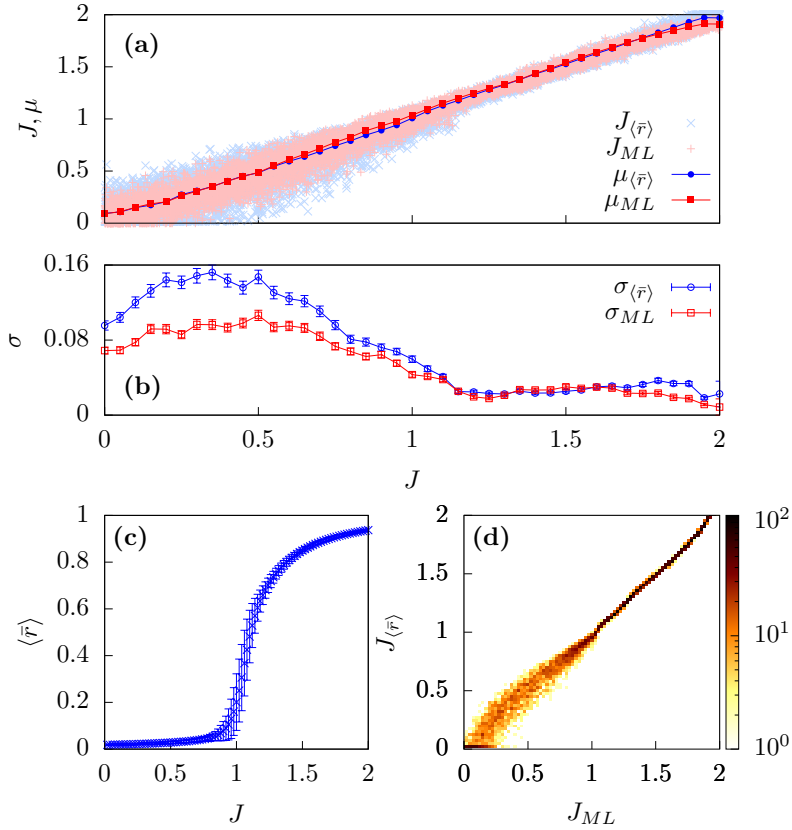
Figure 4.4: (a) The scatter plot of prediction for coupling strength using RNN (light red) and using $\langle \bar{r} \rangle$ (light blue). The line of $y = x$ indicates the correct value of J. For both methods of RNN (red) and $\langle \bar{r} \rangle$ (blue), the mean μ and the standard deviation σ are depicted in (a) and (b), respectively. (c) Ensemble and time averaged value of the order parameter, $\langle \bar{r} \rangle$, as a function of coupling J for generated sample data of $r(t)$. The system exhibits the synchronization transition near the critical value $J_c = 1$. (d) 2D histogram of J_{ML} and $J_{\langle \bar{r} \rangle}$ obtained for each given test datasets.
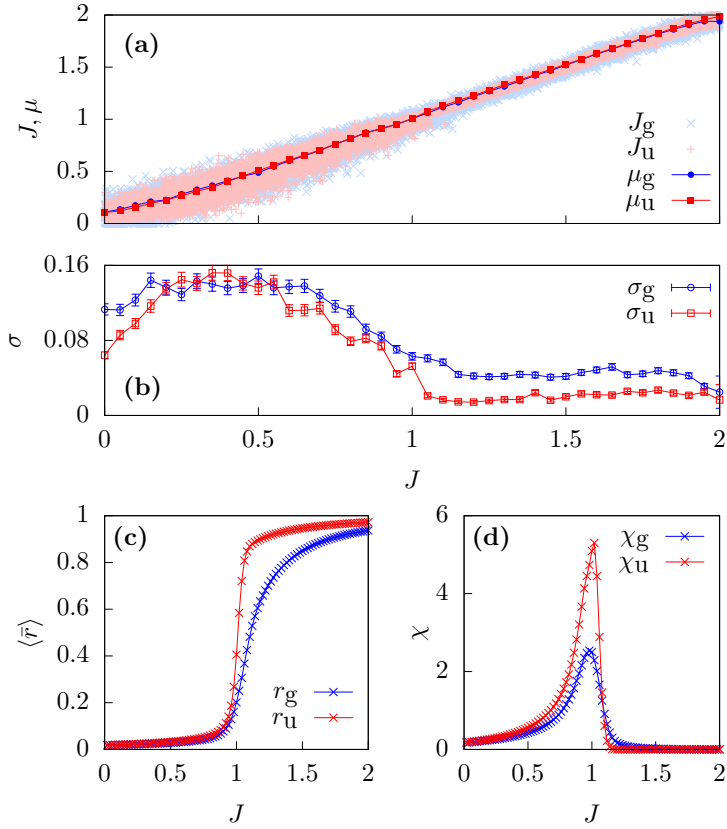
Figure 4.5: (a) The scatter plot of prediction for coupling strength in the case of the uniform natural frequency distribution (light red) and the Gaussian natural frequency distribution (light blue). The line of $y = x$ indicates the correct value of J. For both cases of the uniform distribution (red) and the Gaussian distribution (blue), the mean μ and the standard deviation σ are depicted in (a) and (b), respectively. (c) Ensemble and time averaged value of the order parameter, $\langle \bar{r} \rangle$, and (d) susceptibility, χ, as a function of coupling J for generated sample data of $r(t)$ in both cases. The second-order synchronization transition occurs for the Gaussian distribution while the hybrid synchronization transition occurs for the uniform distribution.

the system to be in subcritical and supercritical region, respectively, as illustrated in Fig. 4.6(a). And the crossing point of two output lines indicates a transition point $J_c(N)$ for given system size N. Since $J_c(N)$ approaches to the critical point $J_c = 1$ as N is increased, we can determine the value of $\bar{\nu}$ using the behavior $|J_c(N) - J_c| \sim N^{-1/\bar{\nu}}$. Fig. 4.6(b) exhibits the finite size scaling of the $J_c(N)$ with the exponent of $1/\bar{\nu} = 0.417 \pm 0.021$ which is consistent with the exponent obtained in Refs. [61–64]. Using Eq. (2.26) and the exponent $1/\bar{\nu} = 0.417$ calculated, output lines for different sizes are collapsed as depicted in Fig. 4.6(c).

In terms of phase transition and critical phenomena, machine learning approaches for classifying phases and finding the critical point have been reported in classical spin models, closed and open quantum models so far [12–15]. We here observe that such studies on the nonlinear dynamical system are also achieved where the synchronization transition is exhibited.

4.5 Application I : Prediction of the phase dynamics

Since the sine function in the coupling term of Eq. (2.1) induces nonlinear/chaotic behavior of oscillators, the system has a sensitive dependence on initial conditions. With the outstanding progress on the model-free prediction of chaotic dynamical systems [25–29], widespread application of the KM provide sufficient motivation for the study of predicting the dynamics of each oscillators in the KM. In particular, RC approach has recently been adopted for various studies of low-dimensional nonlinear systems due to its simplicity and efficiency. In addition to the RC, we here used FCNs, CNNs, and RNNs for prediction of the future behavior of the Kuramoto system.

As an input for this study, time series of phase, $\theta_i(t)$, for each oscillators are generated. We implemented the fourth-order Runge-Kutta method with a discrete time step $\delta t = 0.005$ up to a total of 1.95×10^5 time steps for this generation of datasets. To examine predictability for behaviors of all oscillators, for RC, we take 9×10^4 steps of $\{\cos\theta_i(t), \sin\theta_i(t)\}$ as washout period and subsequent 10^5 steps as an training data
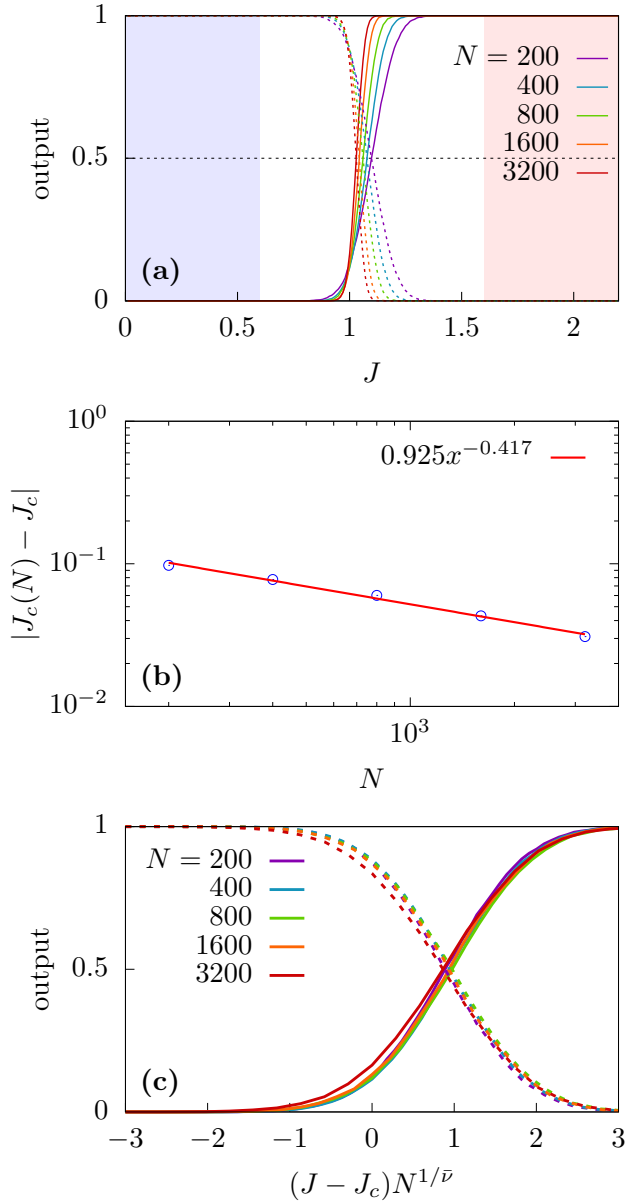
Figure 4.6: (a) Outputs of the neural network trained using data of phase snapshots as a function of J with system size of $N = 200, 400, 800, 1600$ and 3200. The crossing point of two output lines indicates $J_c(N)$ for given N. (b) Behavior of $|J_c(N) - J_c|$ with increasing N. The straight line is the fitting line with slope of -0.417 ± 0.021. (c) Scaling plot for output lines against $(J - J_c)N^{1/\bar{\nu}}$ with $1/\bar{\nu} = 0.417$.
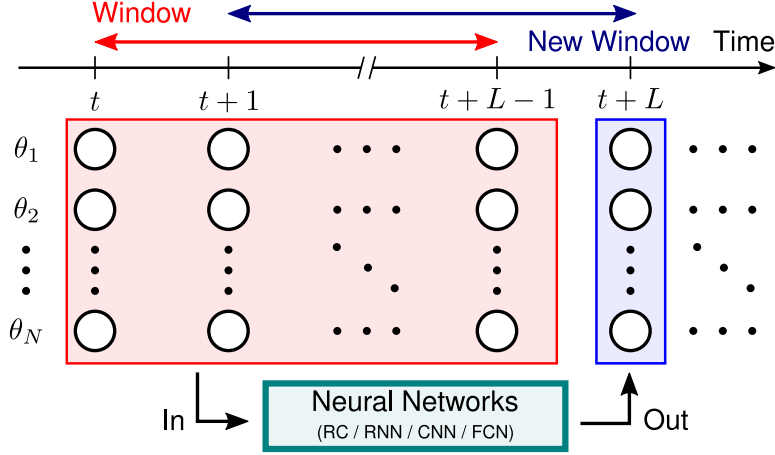
Figure 4.7: Schematic illustration of learning processes by neural networks for prediction of phase dynamics. Using feedback process for given length of the time window, L, inputs for all models are determined from the data of phase dynamics $\{\theta_i(t)\}$ for all oscillators.

to produce phases for last 5×10^3 time steps by feeding the output data back to the reservoir in turn. For other models, taking 1.9×10^5 steps for training datasets, subsequent 5×10^3 time steps of phases are produced as an output by the neural network to compare with the exact dynamics of $\theta_i(t)$. The detailed description for these methods is illustrated in Fig. 4.7. For RC, we set time length $L = 1$ to predict the henceforth phase dynamics, while $L = 200$ is given for inputs of the other models.

Fig. 4.8 shows the prediction for phase dynamics using 4 machine learning models. As shown in Fig. 4.8(b), RC produces accurate predicted data for observed time steps. And one can also obtain the accurate phase dynamics for around $2000 \sim 4000$ steps using classical RNN, CNN and FCN as depicted in Figs. 4.8(c)-(e). Although the Kuramoto model with Eq. (2.1) contains nonlinearity and exhibits chaotic behavior for oscillators, machine learning approaches can be applied to learn the behavior of the phase dynamics and predict future behaviors.

Figure 4.8: Prediction for the phase dynamics of the Kuramoto oscillators using several machine learning methods. (a) The actual evolution of $\{\theta_i(t)\}$. The difference between the actual data and the predicted solution obtained using (b) RC, (c) classical RNN, (d) CNN, and (e) FCN.

4.6   Application II : Reconstruction of the network structure

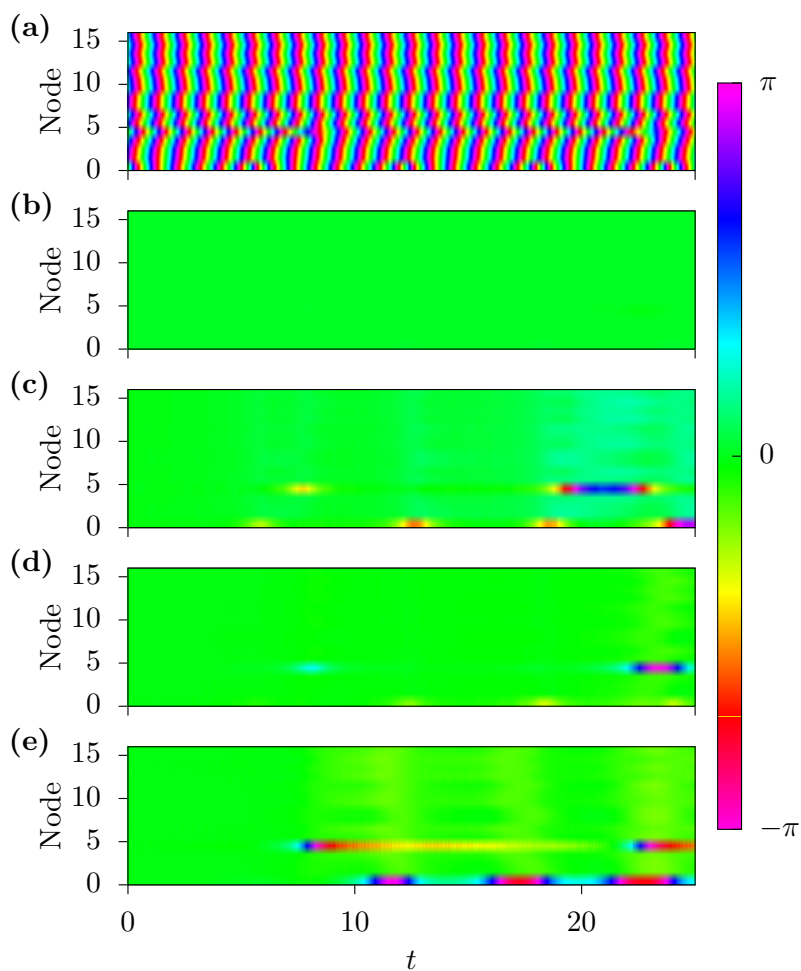Identifying the network topology can be one of the main problem for predicting the behavior of the system and understanding properties of individuals or implicit mechanisms in various systems such as neuronal connections in the brain and epidemics in social networks. Since it is impossible to directly determine the neuronal structure, for example, developments for measuring the time evolution of nodes has been studied to indirectly recover the structure. In the Kuramoto model, it has been studied for the relationship between the modular structure and the synchronization dynamics by observing the correlation between pairs of oscillators which is ordered in a hierarchical way [80]. Applying to more general networks than the modular network, we here assume the situation where the connections of network are not provided but only individual patterns which is produced through inherent interactions between them. As it is of great potential application, machine learning approach is performed to detect whole network topology by comprehending interactions between signals.

For this purpose, we produce 10^6 training datasets for the coupled oscillators on random networks and calculate dynamics of each oscillators following the equation

$$\dot{\theta}_i = \omega_i + K \sum_{j=1}^{N} A_{ij} \sin(\theta_j - \theta_i) \qquad (4.7)$$

where A_{ij} is the adjacency matrix of the given network. Here we adopt $N = 29$ and the natural frequency set, $\{\omega_i\}$, selected regularly from the normal distribution, given in Eq. (2.5). And the given set of $\{\omega_i\}$ are shuffled and assigned to the 29 nodes on the visual cortex network [81], and calculation for Eq. (4.7) is progressed to generate test datasets. As in the previous section, implementing the fourth-order Runge-Kutta method with a time step $\delta t = 0.05$ up to a total of 200 steps, sets of time series of phases, $\{\theta_i(t)\}$, are generated for input. And we set the initial phase as $\theta_i(0) = 0$ for all i.
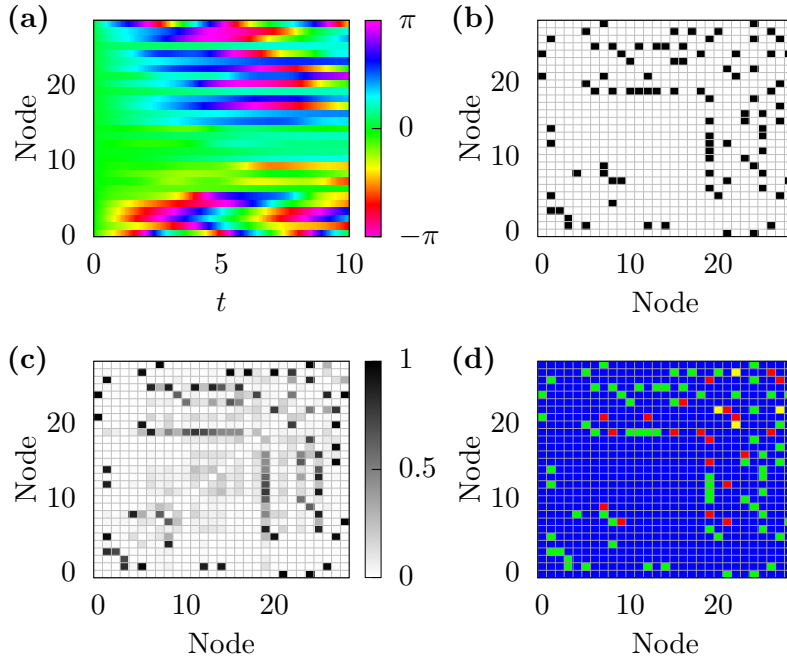
Figure 4.9: Reconstruction of the visual cortex network with $N = 29$. (a) An input dataset of the actual phase evolution, $\{\theta_i(t)\}$, for one of the sample set of shuffled natural frequencies. (b) The actual adjacency matrix of the visual cortex network. Black square indicates the link existing on the network. (c) Outputs obtained through RNN. Output elements are in a range of $[0, 1]$. (d) Comparison between the actual adjacency matrix and the rounded values of obtained output elements in Panel (c). Blue (green) square denotes the case when the corresponding element in the actual network is zero (one) and the one in the rounded output element is also zero (one). Red (yellow) square denotes the case when the corresponding element in the actual network is zero (one) and the one in the rounded output element is one (zero).

Fig. 4.9(a) illustrates one of the pattern samples used for testing the neural network. The actual given network topology for this pattern is depicted as the adjacency matrix shown in Fig. 4.9(b). As the trained neural network produces real numbers in the range of $[0, 1]$ (see Fig. 4.9(c)) which implies the probabilities for each links or elements in the adjacency matrix to exist, these outputs are rounded off to 0 or 1 as in Fig. 4.9(d), to compare with the actual matrix. Although phase dynamics of all oscillators exhibit irregular and complex behaviors, the prediction for the underlying network topology is successfully achieved by the neural network as shown in Fig. 4.9(b) and (d). We obtained the accuracy of 93.5% for all elements in adjacency matrices of total 10^3 samples.

4.7 Summary

To summarize, with machine learning methods for the coupled oscillator system, we have performed phase classification and model-free prediction based on exploiting chaotic property of the system. We demonstrate that the scaling behavior is not only verified for the second-order synchronization transition through the discrimination between the asynchronous state and the synchronous state with neural network approaches, but also identified for the model where numerical analysis for finite size scaling is demanding. Furthermore, despite of the nonlinearity of the system, successful prediction for the future behavior of the phase dynamics is achieved by employing machine learning approaches. As the learning for chaotic dynamics of coupled oscillators is confirmed, artificial neural networks are trained with the patterns of individual elements on real brain network. Underlying connections between them can be identified through the well-trained machine and this can be extended to other problems for detecting the topology of the system. Additionally, as the model-free prediction for nonlinear dynamics has been performed, such machine learning methods overcome the disadvantages of analysis with modelling and simulation, and thus, have extensive applicability to other nonlinear models or systems in nature. Consequently, we

believe that our work may shed light on the further studies of machine learning on nonlinear/chaotic systems.

Chapter 5

Conclusion

We investigated the synchronization of coupled oscillator system through both analytic approach and data driven method. Synchronization is ubiquitous phenomena observed in nature. The system with interacting oscillators on complex network are one of the most proper model to describe such collective behavior. In particular, the Kuramoto model is the most representative model for the phase synchronization achieved by adjusting oscillators' phases through the interaction between them. As this model exhibits rich properties such as the synchronization transition and chaotic behavior, it is worthful to explore and adopt for figuring out synchronization or chaotic dynamics emerging in natural and artificial systems.

We analytically constructed the *ad hoc* potential regarding to the coupled oscillator system, which demonstrates the landscape over the order parameter space and provides support for intuitive understanding of phase transition. As the Landau theory is established to describe what happens at and near the critical point, the potential scheme has been conventionally applied for the thermal equilibrium system exhibiting various types of phase transition. Along with the second-order and the first-order phase transition, the hybrid transition has been observed in various systems and the criteria of the Landau theory for this hybrid phase transition was constructed for thermal systems. We here developed the potential approaches for the nonequilibrium system, the Kuramoto system from the self-consistency equation derived. As we confirmed that this scheme is valid up to the dominant order, the *ad hoc* potential approach to the phase transition is applied for the synchronization transition of the Kuramoto system. With

varying the natural frequency distributions and models, we identified that the profile of the *ad hoc* potential in the thermodynamic limit behaves as the Landau potential for the same type of phase transition. In particular, for the model exhibiting the hybrid synchronization transition, the *ad hoc* potential satisfies the criteria of the Landau potential for hybrid phase transition. We believe that the introduced methodology can potentially be applied to the Kuramoto systems with various sets of natural frequencies and models. Consequently, this approach may can shed light on the interpretation of the system dynamics and the phase transition for any model consisting of Kuramoto oscillators.

As recent advances in a diverse fields of science and engineering have been achieved by adopting the machine learning methods, we also performed the machine learning approach to the coupled oscillator system. By assuming the situation where the limited amount of information is given, we examined that whether target parameters can be inferred. Based on the data obtained through the numerical simulation for the Kuramoto model, predicting the future dynamical evolution of the system and identifying underlying parameter and structure are performed. Once the data for the order parameter dynamics obtained numerically, these are used as an input for training the machine, the fully-connected neural network in this case, to deduce the inherent coupling strength. The machine learning approach demonstrates more precise results than the inference through statistical quantities. Additionally, by feeding all phases of oscillators, the machine is also trained to classify the ordered state, or the synchronous state, and the disordered state, or the asynchronous state. By obtaining predictibilities for each configuration to be in subcritical and supercritical region, we identify the critical value with scaling behavior for synchronization transition of the Kuramoto model. Also, utilizing the property of the nonlinear and chaotic behavior for the coupled oscillators, we construct tasks which can be applicable to general systems exhibiting intricate dynamical evolution. Long-term prediction for future chaotic phase dynamics for all oscillators was successfully achieved by 4 machine learning models, FCN,

CNN, RNN, and RC. We also reconstructed the underlying topology of the real brain network by learning all the phase dynamics. It is believed that our work for application of machine learning on coupled oscillator system has potential for the further studies of machine learning on chaotic systems or synchronization transition.

Appendices

Appendix A

Numerical simulation method

Guidance and tips for numerical simulation of the Kuramoto model are introduced in this part.

A.1 Runge-Kutta method

For the most differential equations given in the real world, it is not simple to obtain algebraic solutions. As a result, one can figure out solutions of such differential equations by solving them numerically. As one of the numerical approach for solving them, simple Euler method is the most basic method for numerical integration with a given initial value. The improved version of the Euler method, Heun's method can also be adopted to overcome shortcomings of the Euler method, inaccuracy and slowness. All these methods are generalized as a collection of Runge-Kutta methods by adding multiple steps for calculation. That is, the Euler method and Heun's method are represented by the first-order Runge-Kutta method, and the second-order Runge-Kutta method, respectively. Beyond that, the fourth-order Runge-Kutta method, or RK4 method, is the technique commonly used as it achieves balance between computational cost and accuracy. Most computer packages are designed to use this method by default for numerical calculation of differential equations.

The initial value problem is given by

$$\frac{dy}{dt} = f(t, y) \quad \text{and} \quad y(t_0) = y_0 \tag{A.1}$$

where y is an unknown function of time t and initial conditions y_0 and t_0 are given. The procedure for calculation of the differential equation as follows :

$$y_{n+1} = y_n + \frac{1}{6}(k_1 + 2k_2 + 2k_3 + k_4) \tag{A.2}$$

and

$$t_{n+1} = t_n + h \tag{A.3}$$

where h is the size of the interval and four slopes,

$$k_1 = f\left(t_n, y_n\right)$$
$$k_2 = f\left(t_n + \frac{h}{2}, y_n + \frac{hk_1}{2}\right)$$
$$k_3 = f\left(t_n + \frac{h}{2}, y_n + \frac{hk_2}{2}\right)$$
$$k_4 = f\left(t_n + h, y_n + hk_3\right) \tag{A.4}$$

are determined. Therefore, the next value of y is calculated by weighed averaging the four slopes given in the range of time interval h. As the RK4 method is a fourth-order method, the local truncation error is an order of $\mathcal{O}(h^5)$ and the total accumulated error is an order of $\mathcal{O}(h^4)$.

We applied this RK4 method for the numerical calculation of the Kuramoto model, the time-invariant system where the function $f(\{\theta_{i,n}\})$ is given by

$$f(\{\theta_{i,n}\}) = \omega_i + \frac{K}{N}\sum_{j=1}^{N}\sin(\theta_{j,n} - \theta_{i,n}). \tag{A.5}$$

For fixed value of h, one can obtain four slopes, k_1, k_2, k_3 and k_4, and the next values of phases, $\{\theta_{i,n+1}\}$, in turn.

A.2   Kahan summation

For iteratively adding a sequence of finite-precision floating numbers, numerical error in total summation can arise. When n numbers are summed in sequence, a root mean square error of the summation grows as $\sqrt{n}$ in the worst case. With the Kahan summation, one can minimize this loss of significance in accumulation as it include the compensated summation in the calculation loop. By doing so, the error bound becomes effectively independent of n. The pseudocode for this algorithm is given as follows :

Algorithm 1 Kahan summation algorithm

1: **procedure** KAHANSUM ($input$)
2:     **var** $sum \leftarrow 0.0$
3:     **var** $c \leftarrow 0.0$
4:     **for** $i \leftarrow 1, input.length$ **do**
5:         **var** $y \leftarrow input[i] - c$
6:         **var** $t \leftarrow sum + y$
7:         $c \leftarrow (t - sum) - y$
8:         $sum \leftarrow t$
9:     **return** sum

A.3   Simulation of the Kuramoto equation

Evaluation for sine function is the most time consuming process over the whole numerical calculation of the Kuramoto model given by

$$\dot{\theta}_i = \omega_i + \frac{K}{N} \sum_{j=1}^{N} \sin(\theta_j - \theta_i).$$

(A.6)

Naive evaluation and summation of sine functions in interaction term of the Kuramoto model given in Eq. (A.6) require cost as much as $\mathcal{O}(N^2)$ sine calculation. To reduce the time taken for evaluation of sine functions and improve the speed of the calculation, one can develop the calculation by considering the order parameter at each time step.

Using the definition of order parameter given in Eq. (2.14), Eq. (A.6) can be rearranged by the trigonometric identity as below :

$$\dot{\theta}_i = \omega_i + Kr\sin(\psi - \theta_i)$$
$$= \omega_i + Kr(\sin\psi\cos\theta_i - \cos\psi\sin\theta_i)\,. \tag{A.7}$$

In the meanwhile, since the order parameter equation can be rewritten as

$$Z = re^{i\psi} = \frac{1}{N}\sum_{j=1}^{N} e^{i\theta_j}$$
$$= \frac{1}{N}\sum_{j=1}^{N}\cos\theta_j + i\frac{1}{N}\sum_{j=1}^{N}\sin\theta_j\,, \tag{A.8}$$

we simply obtain that

$$r\cos\psi = \frac{1}{N}\sum_{j=1}^{N}\cos\theta_j$$
$$r\sin\psi = \frac{1}{N}\sum_{j=1}^{N}\sin\theta_j\,. \tag{A.9}$$

Therefore, once the cosine and sine evaluation for all phases are processed, simple summation and multiplication allow the calculation for all phase updates given in Eq. (A.6). And the total number of sine evaluation is reduced to $\mathcal{O}(N)$ which is much faster than the case of naive calculation for $\sin(\theta_j - \theta_i)$.

Appendix B

Asymmetric interaction-frequency correlated model

For the model following Eq. (3.48), it is known that the explosive synchronization also occurs for asymmetric $g(\omega)$ such as power-law frequency distribution given by

$$g(\omega) \sim \omega^{-\gamma} \tag{B.1}$$

with $\omega > 0$. In this case, Eq. (3.51) can be written as

$$\Delta \dot{\theta}_j = \omega_j - \Omega - K \omega_j r \sin(\Delta \theta_j). \tag{B.2}$$

As in Sec. 3.4.1, following the same derivation in the thermodynamic limit, we obtain two equations

$$1 - \frac{\gamma - 1}{\gamma \omega_0} \Omega = \int_{\omega_0}^{\infty} d\omega g(\omega) \left(\frac{\omega - \Omega}{\omega} \right) \sqrt{1 - \left(\frac{\alpha \omega}{\omega - \Omega} \right)^2} \, \Theta \left(\left| \frac{\omega - \Omega}{\alpha \omega} \right| - 1 \right) \tag{B.3}$$

$$r = \int_{\omega_0}^{\infty} d\omega g(\omega) \sqrt{1 - \left(\frac{\omega - \Omega}{\alpha \omega} \right)^2} \, \Theta \left(1 - \left| \frac{\omega - \Omega}{\alpha \omega} \right| \right) \tag{B.4}$$

for two parameters $\alpha \equiv Kr$ and Ω. Here, ω_0 is the minimum value of the natural frequency. Note that these two equations have very similar form with Eqs. (3.46) and (3.47). As the system exhibits second-order, hybrid and first-order transitions for $\gamma > 3$, $\gamma = 3$, and $2 < \gamma < 3$, respectively, in Sec. 3.4.1, corresponding transitions occur for $\gamma > 2$, $\gamma = 2$, and $1 < \gamma < 2$ in this system. In particular, further analytical

calculation can be performed for the case of $\gamma = 2$.

First, introducing new variable $x \equiv q/(q - \Omega)$, Eq. (B.3) becomes

$$
\frac{\Omega^{\gamma-1}}{\omega_0^{\gamma}} \left(\frac{\omega_0}{\gamma - 1} - \frac{\Omega}{\gamma} \right)
$$
$$
= - \left(\int_{\frac{\omega_0}{\omega_0 - \Omega}}^{-\infty} dx + \int_{\infty}^{1} dx \right) x^{-3} \left(\frac{x}{x - 1} \right)^{2-\gamma} \sqrt{1 - (\alpha x)^2} \Theta(1 - |\alpha x|). \quad \text{(B.5)}
$$

For the case of $\gamma = 2$, this equation is reduced to

$$
\frac{\Omega(2\omega_0 - \Omega)}{2\omega_0^2} = - \left(\int_{\frac{\omega_0}{\Omega - \omega_0}}^{\infty} dx - \int_{1}^{\infty} dx \right) x^{-3} \sqrt{1 - (\alpha x)^2} \Theta(1 - |\alpha x|) \quad \text{(B.6)}
$$

which is exactly the same equation with the system in Sec. 3.4.1 with $\gamma = 3$ and it also has a solution $\Omega = 2\omega_0$ for any α. In a similar way, introducing new variable $x \equiv (\omega - \Omega)/\omega$, Eq. (B.4) becomes

$$
r = (\gamma - 1) \left(\frac{\Omega}{\omega_0} \right)^{1-\gamma} \int_{\frac{\omega_0 - \Omega}{\omega_0}}^{1} dx (1 - x)^{\gamma-2} \sqrt{1 - \left(\frac{x}{\alpha} \right)^2} \Theta \left(1 - \left| \frac{x}{\alpha} \right| \right). \quad \text{(B.7)}
$$

For a simple case of $\gamma = 2$, using $\Omega = 2\omega_0$, Eq. (B.7) is reduced to

$$
r = \frac{1}{2} \int_{-1}^{1} \sqrt{1 - \left(\frac{x}{Kr} \right)^2} \Theta \left(1 - \left| \frac{x}{Kr} \right| \right) dx \quad \text{(B.8)}
$$

$$
= \begin{cases} \frac{K}{K_c} r & \text{for} \quad Kr \leq 1 \\ \frac{1}{2} \sqrt{1 - \frac{1}{K^2 r^2}} + \frac{Kr}{2} \arcsin \left(\frac{1}{Kr} \right) & \text{for} \quad Kr > 1 \end{cases} \quad \text{(B.9)}
$$

Solving equations numerically, we obtain $U(r)$ for $\gamma = 1.8$, 2.0 and 2.8 as shown in Fig. B.1(a), (c), and (e), respectively. As in the degree-frequency correlated model, the type of synchronization transition changes with varying γ. In this case, however, the hybrid transition occurs for the case of $\gamma = 2.0$, not 3.0 as in the former model.
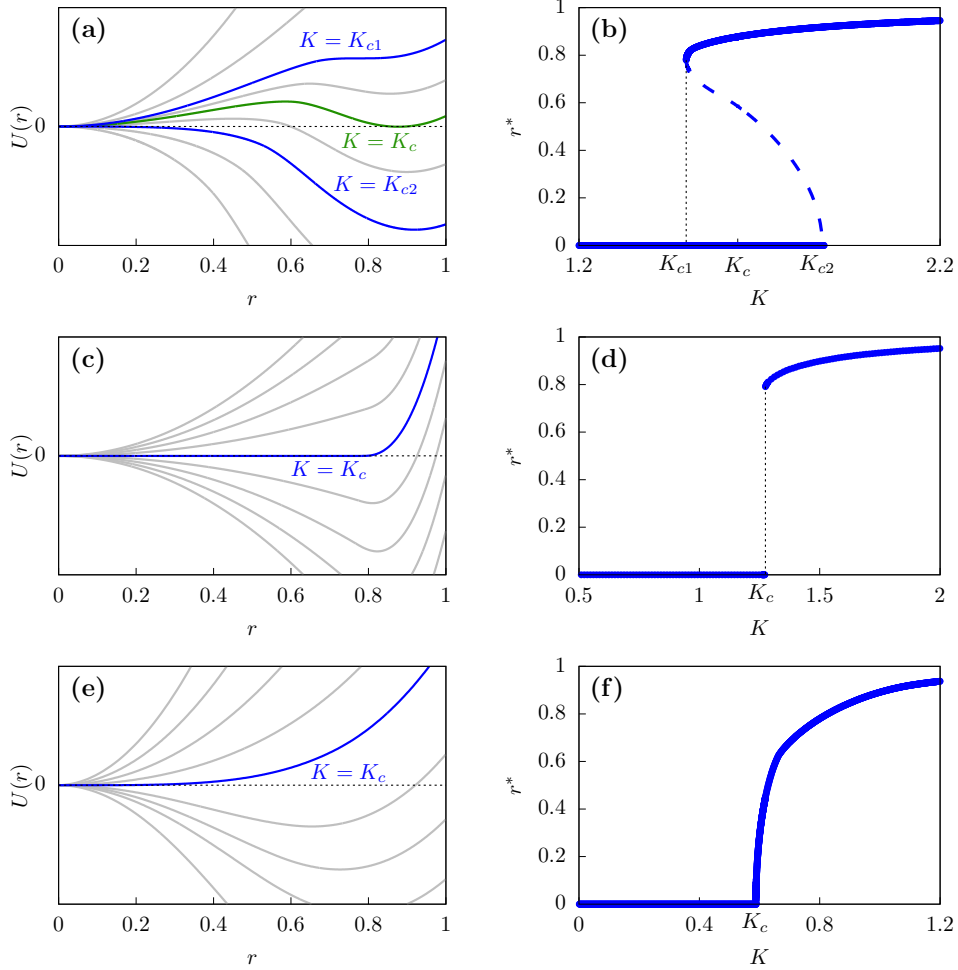
Figure B.1: *Ad hoc* potential $U(r)$ for the KE given by Eq. (3.48) with power-law natural frequency distribution in Eq. (B.1). The change of $U(r)$ with varying K is obtained for (a) $\gamma = 1.8$ (c) 2.0 and (e) 2.8. And the position of minima r^* exhibits (b) first-order, (d) hybrid, and (f) second-order transitions, respectively.

Appendix C

Effective potential approaches for finite size systems

In finite systems, the SCE given in Eq. (3.11) is written as

$$r = \frac{1}{N} \sum_{|\omega_i| \leq Kr} \sqrt{1 - \frac{\omega_i^2}{K^2 r^2}} \equiv f(r). \qquad (C.1)$$

with a sample-dependent correction $\delta f \equiv f - \langle f \rangle \propto \sqrt{N_s}/N$ where $\langle \cdot \rangle$ indicates sample average and N_s is the number of entrained oscillators with $\omega_i \leq Kr$ [62, 64, 82, 83]. This SCE may also be written in the form $x/K = h(x)$, where

$$h(x) \equiv \frac{1}{N} \sum_{|\omega_i| \leq x} \sqrt{1 - \frac{\omega_i^2}{x^2}} = \frac{x}{K}, \qquad (C.2)$$

where $x \equiv Kr$ and $h(x)$ replaces $f(r)$. Here we consider that $g(\omega)$ is uniform. The *ad hoc* potential is defined as it was above:

$$U(r) = \int_0^r (r' - f(r'))dr'. \qquad (C.3)$$

We consider two cases in which the natural frequencies of each oscillator are taken randomly and regularly.

C.1   Random sampling of $\{\omega_i\}$

We first consider the case that ω_i is selected randomly from the uniform distribution $g(\omega)$ given by (3.57) for half of the oscillators ($i = 1, \ldots, N/2$), and the other half

are assigned values following $\omega_i = -\omega_{N-i+1}$ for $i = N/2 + 1, \ldots, N$, so that the mean natural frequency becomes zero. The *ad hoc* potential of the SCE for each case is obtained as shown in Fig. C.1(a). For a given K, there exist local minima, which are stable solutions of the SCE. The global minimum of the potential develops from $r = 0$ as K is increased, leading the order parameter to jump to a finite value. This abrupt change of the position of the global minimum suggests the possibility of a hybrid synchronization transition in the limit $N \to \infty$, as discussed in Sec. 3.5.1.

To validate this scheme in view of the effective potential, we perform simulations for a system size $N = 6400$ using the fourth-order Runge-Kutta method up to $t = 10^6$ time in steps of $\delta t = 10^{-2}$.

Fig. C.1(b) shows the evolution of the order parameter under the same condition used in Fig. C.1(a). Because initial phases of each oscillators are distributed randomly, the order parameter is $r \sim \mathcal{O}(N^{-1/2})$ at $t = 0$. As time runs, the dynamics proceeds according to the effective potential landscape. As shown in Fig. C.1(b), $r(t)$ exhibits a plateau with some fluctuations for a certain period of time. Comparing with the profile of the *ad hoc* potential, this pattern results from that the system is confined in a corresponding potential well before jumping to the next.

As r increases, the number of drifting oscillators decreases according to $\langle N_d \rangle = (1 - r/r_c)N$ and so do the dynamic fluctuations of the order parameter [see the width of the fluctuations in Fig. C.1(b)]. Moreover, the potential barrier from $r \approx 0.4$ to the left is higher than that to the right in Fig. C.1(a)], and thus the system tends to move to the right side of the landscape (larger r). Consequently, the system beginning at $r \sim \mathcal{O}(N^{-1/2})$ passes through metastable states of local potential wells and then reaches the steady state, which corresponds to the rightmost position, as far as possible, among the positions of the local minima.

We also consider the evolution of the order parameter from different initial values of r. For the same randomly sampled set used in Fig. C.1, the dynamics begins in a totally synchronized state, $r = 1$, and flows to the steady state coinciding with the final
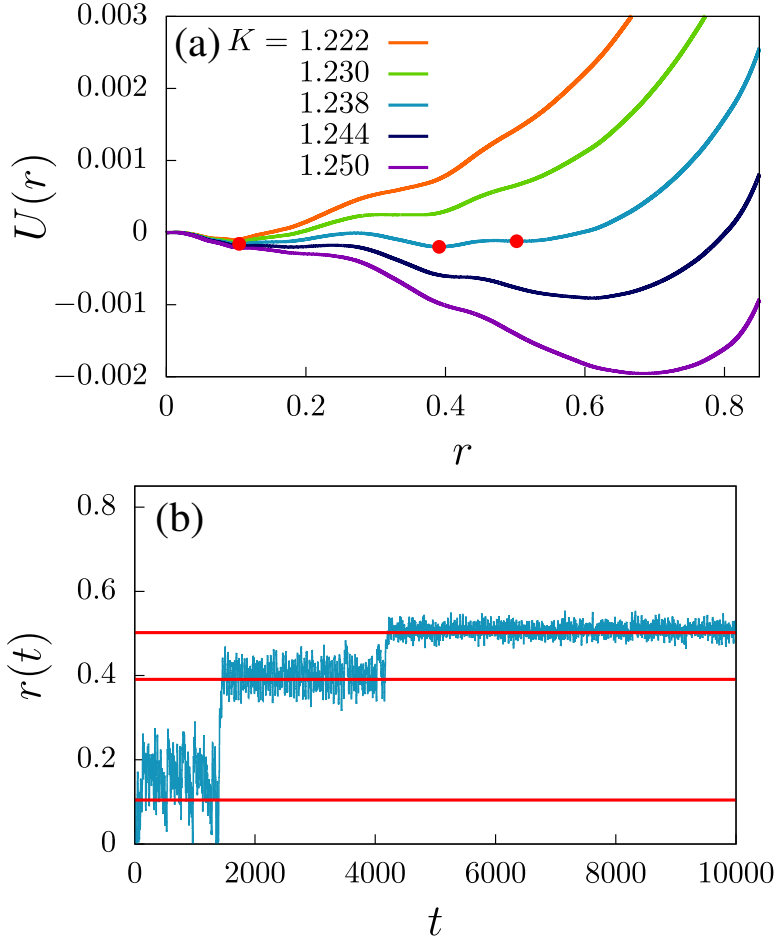
Figure C.1: (a) Plot of *ad hoc* potential $U(r)$ as a function of r for the case of random sampling of $\{\omega_i\}$ from the uniform distribution $g(\omega)$ with $\gamma = 1$ for $K = 1.222, 1.230, 1.238, 1.244,$ and 1.250. Except the minimum at $r = 0$, local minima of $U(r)$ are marked by red dots for $K = 1.238$. (b) Time evolution of the order parameter $m(t)$ for the set of oscillators used in (a) with $K = 1.238$ and random initial phases. The three local minima positions in (a) are indicated by red lines.

Figure C.2: Comparison of the order parameter behavior as a function of t from different initial configurations with $r(0) \sim \mathcal{O}(N^{-1/2})$ (blue, d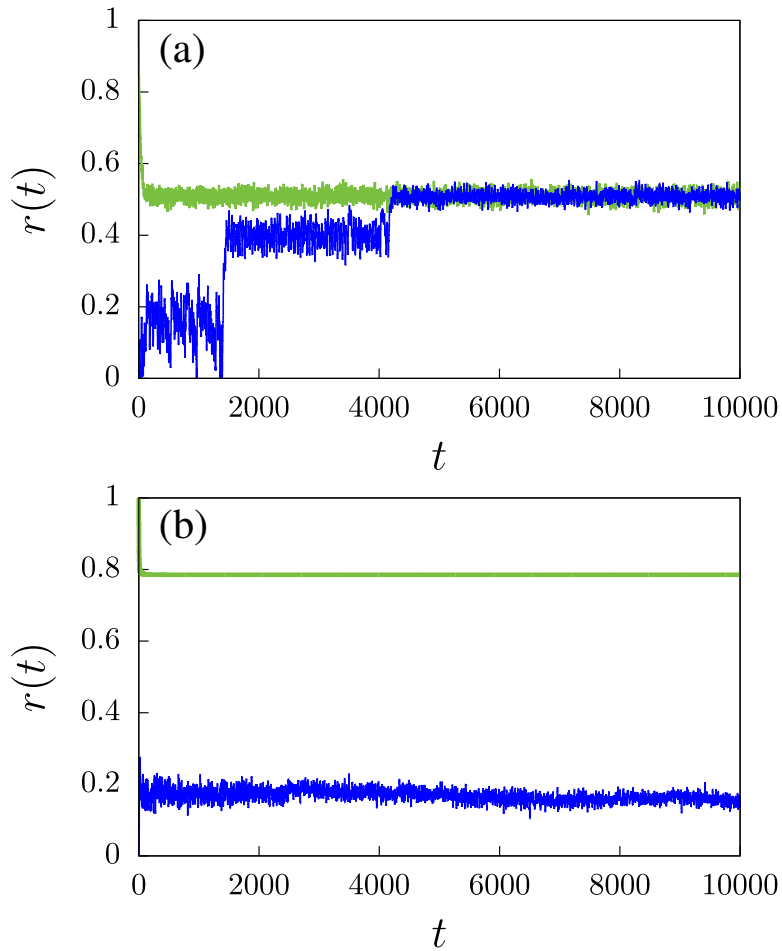ark) and 1 (green, gray). Natural frequencies of each oscillator are selected randomly in (a) and regularly in (b). Numerical simulations are performed for the case $N = 6400$ at $K = 1.238$ (a) and K_c (b).

state of the dynamics beginning at $r \sim \mathcal{O}(N^{-1/2})$. This can be intuitively understood in terms of the *ad hoc* potential shown in Fig. C.1(a). At the initial value of $r = 1$, the dynamics of the system moves down from the far right side of the potential and first encounters a minimum at a certain value of r. As the fluctuations at this minimum are not sufficiently large to overcome the barrier on the left, the dynamics remains at this minimum, as shown in Fig. C.2(a). This result does not differ much from that of other general random sets of $\{\omega_i\}$.

C.2 Regular sampling of $\{\omega_i\}$

We consider that $\{\omega_i\}$ is selected regularly from the uniform distribution given in Eq. (3.57). In this case, ω_i is given as

$$\omega_i = -\gamma + \frac{\gamma}{N}(2i - 1) \tag{C.4}$$

for $i = 1, \ldots, N$. The SCE of Eq. (C.2) is rewritten as

$$\frac{x}{K} = \frac{1}{N} \sum_{i=N-n+1}^{n} \sqrt{1 - \frac{\omega_i^2}{x^2}} = h(x), \tag{C.5}$$

where n is the index satisfying $\omega_n \leq x < \omega_{n+1}$, so phase-locked oscillators contribute to the summation.

Fig. C.3(a) illustrates the behaviors of both sides of Eq. (C.5) along with the parameter x. $h(x)$ is a continuous function; however, it is not smooth in shape because the range of the summation varies with x. Because the slope of the l.h.s. of the equation is $1/K$, it is instructive to notice how solutions of Eq. (C.5), denoted as $\{r^*\}$, change as K is increased by examining the crossing points of the linear line and $h(x)$. For instance, in Fig. C.3(a), when the slope $1/K$ is sufficiently large, a linear line with slope $1/K$ meets $h(x)$ only at $r^* = 0$, which is a solution of the SCE. As $1/K$ is decreased, the number of solutions r^* increases, and there exists $K^{**}(N)$ at which the

number of solutions becomes N for the first time. At this point, the SCE has a non-trivial solution in the range $x > \omega_N$, as shown in Fig. C.3(a). This solution becomes a local minimum of $U(r)$ at the largest r^*, denoted as r^{**} which implies that all the oscillators are phase-locked. Thus, when dynamics starts from $r = 1$, the system reaches to the state with the r^{**} value as shown in Fig. C.3(b). When $1/K$ is decreased further and reaches $1/K_c(N)$, $U(r^{**})$ at r^{**} becomes zero. This is another global minimum for finite r. Between these two values of $K^{**}(N)$ and $K_c(N)$, there exists the transition point $K_c(\infty)$ in the thermodynamic limit. For brevity, we denote it as K_c. At this K_c, the *ad hoc* potential $U(r)$ exhibits underdamped oscillation around a plateau as depicted in Fig. C.3(b).

In Figs. C.4(a) and (b), we show the positions r^* of local minima for each given K. For instance, when $N = 10$, there exist five nonzero r^* values when $K = K_c(N)$, which correspond to the positions of the five local minima in Fig. C.3(b).

C.3 Trapped at metastable states

Here, we note that for the regular sampling case, the system can be more easily trapped at a longstanding metastable local minimum positioned at $r^* < r_c$. For instance, as shown in Fig. C.2(b), when dynamics starts from $r = 1$, the system stays at $r \approx 0.8$ for a long time within the limit of our simulation time, which differs from $r \approx 0.2$ reached from an initial state with $r \sim \mathcal{O}(N^{-1/2})$. Thus, we need more careful check if the system indeed remains at some metastable state with $r^* \neq r_c(\infty)$ as $N \to \infty$.

We perform numerical simulations for the KM (2.1) with the uniform distribution of $g(\omega)$ given by Eq. (3.57) at a fixed $K_c = 4\gamma/\pi$. The system size is controlled. We remind that at K_c, the potential $U(r)$ exhibits underdamped oscillation around a plateau, whereas at $K_c(N)$, the potential $U(r)$ is slanted. We first assign a random set of initial phases $\{\theta_i(0)\}$ $(i = 1, \ldots, N)$ and trace the order parameter as a function of time for 10^3 realizations. For better statistics, we take time intervals specified in the legend of Fig. C.5(a). Each of these intervals contains 10^4 times. Taking all order
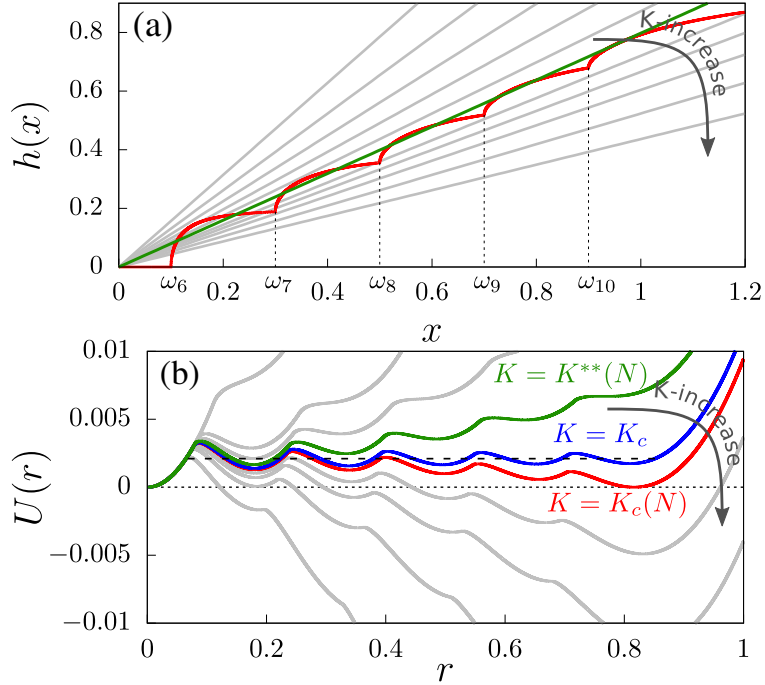
Figure C.3: (a) Schematic plot of each side of Eq. (C.5) for $N = 10$ and $\gamma = 1$. The r.h.s. of the equation, $h(x)$ (red line), increases abruptly at the points where x is equal to each value of ω_i marked on the x axis. Linear lines with various slopes indicate the l.h.s. of the equation with different values of K (gray line), including $K = K^{**}(N)$ (green line). (b) Potential $U(r)$ versus r at $K = K^{**}(N)$ (green), K_c (blue), and $K = K_c(N)$ (red). At $K = K_c(N)$, there exist $N/2$ local minima and $U(r^*) = 0$ at the largest r^*, representing $r_c(N)$. Thus, a global minimum occurs at $r_c(N)$.
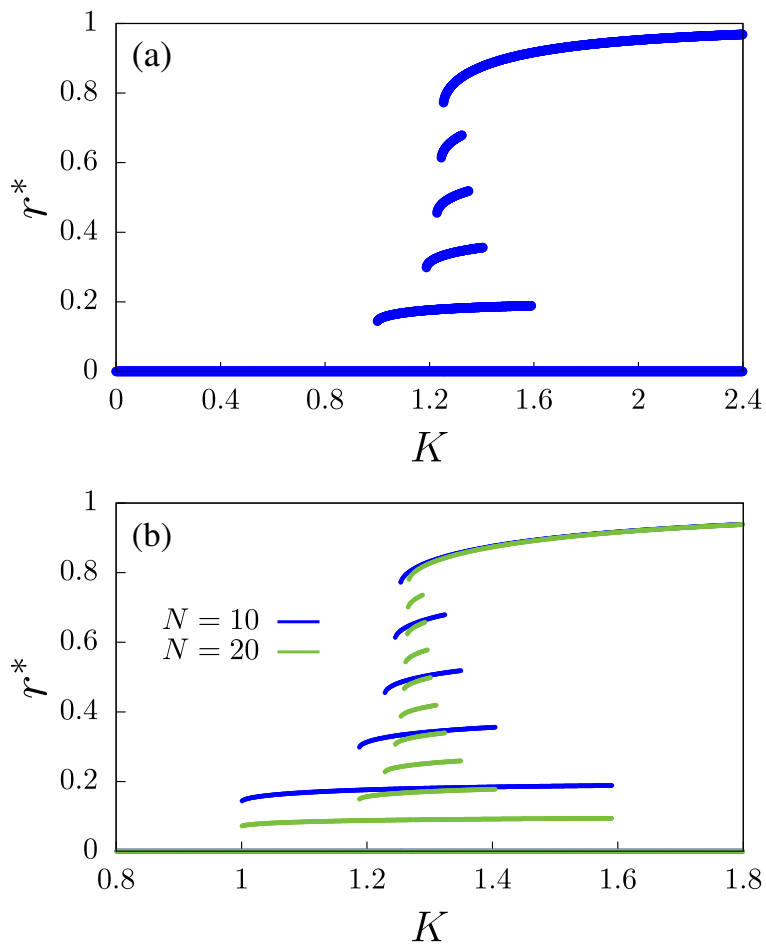
Figure C.4: (a) Positions r^* for the local minima of $U(r)$ for a given K are unstable unless $U(r^*)$ is a global minimum with $N = 10$ and $\gamma = 1$. (b) Solutions r^* of the SCE (C.5) for two different system sizes $N = 10$ and 20.

Figure C.5: (a) Plot of the distribution $P(r(t))$ versus $r(t)$ obtained from time intervals $t \in [0, 10000], [5000, 15000], [10000, 20000], [20000, 30000]$, and $[40000, 50000]$ and 10^3 realizations at $J_c(N)$. The system size is fixed as $N = 6400$. (b) Plot of $D(t_i)$ versus t_i for various system sizes.

parameter values in each given time interval, the distribution of the order parameter $P(r(t))$ is constructed as shown in Fig. C.5(a). Whereas in early time interv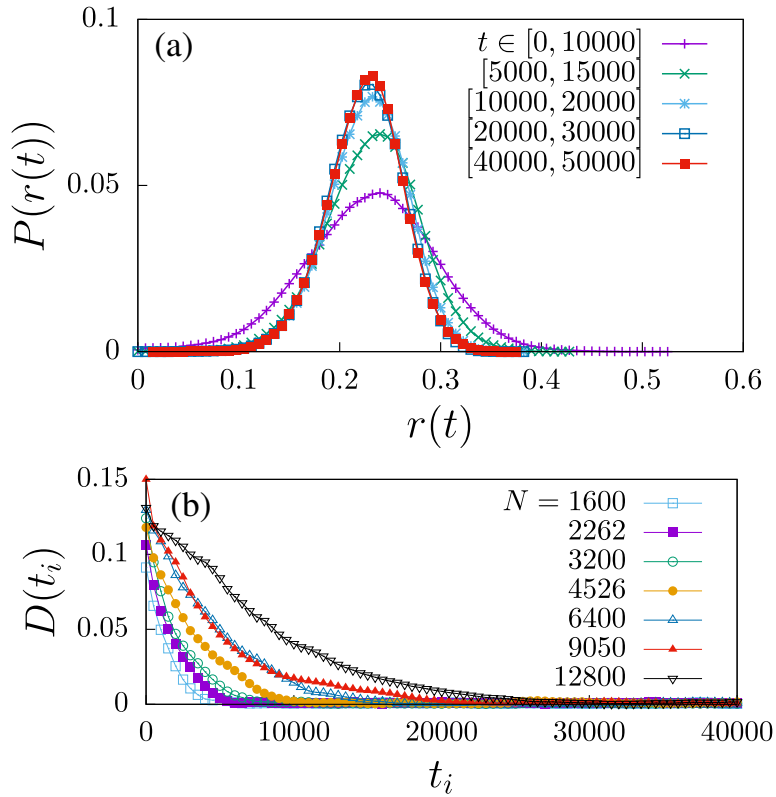als, the order parameters are distributed in broad range of r, as time goes on, the distribution becomes narrower; the mean value is shift; and it finally approaches to a stationary distribution, being insensitive to when the interval is taken. To check the stability of the distribution function, we use the so-called Kullback-Leibler (KL) divergence, in which measure D is introduced as

$$D \equiv \int a(r) \ln \left(\frac{a(r)}{b(r)} \right) dr + \int b(r) \ln \left(\frac{b(r)}{a(r)} \right) dr. \tag{C.6}$$

This measure indicates to what extent two distributions $a(r)$ and $b(r)$ differs from each other. When the two distributions are exactly the same, $D = 0$. To check the KL divergence for $P(r(t))$, we take the $P(r(t))$ obtained from the latest time interval $t \in [9.9 \times 10^4, 10^5]$ as $a(r)$ and the distribution at different time interval $[t_i, t_i + 1000]$ as $b(r)$. Then, the dependence of D on t_i is calculated with increasing t_i. Since the distribution $P(r)$ converges to a certain form as illustrated in Fig. C.5(a), we expect that D gradually decreases and approaches to zero. Indeed, $D(t_i)$ behaves as shown in Fig. C.5(b). Moreover, we trace $D(t_i)$ values as a function of t_i for different system sizes N, finding that the saturation time becomes longer as the system size is increased. Based on these results, we conclude that the distribution $P(r)$ for $N \leq 12800$ is in steady state at the time $t = 10^5$.

We examine the distribution $P(r)$ for different system sizes N in steady states. As the system size N is increased, the peak position of $P(r)$ moves to the left and the width becomes narrower, as shown in Fig. C.6(a). By measuring the mean values $\langle r \rangle$ of $P(r)$ and the standard deviation σ_r for various system sizes, we obtain power-law decays as $\langle r \rangle \sim N^{-0.24}$ and $\sigma_r \sim N^{-0.39}$, as shown in Figs. C.6(b) and C.6(c), respectively. These power-law behaviors suggest that the system stays at $r = 0$ in the limit $N \to \infty$, which is in agreement with the previous result in Sec. 3.5.1. Moreover, this result may explain the reason for the discrepancy of the steady states reached from

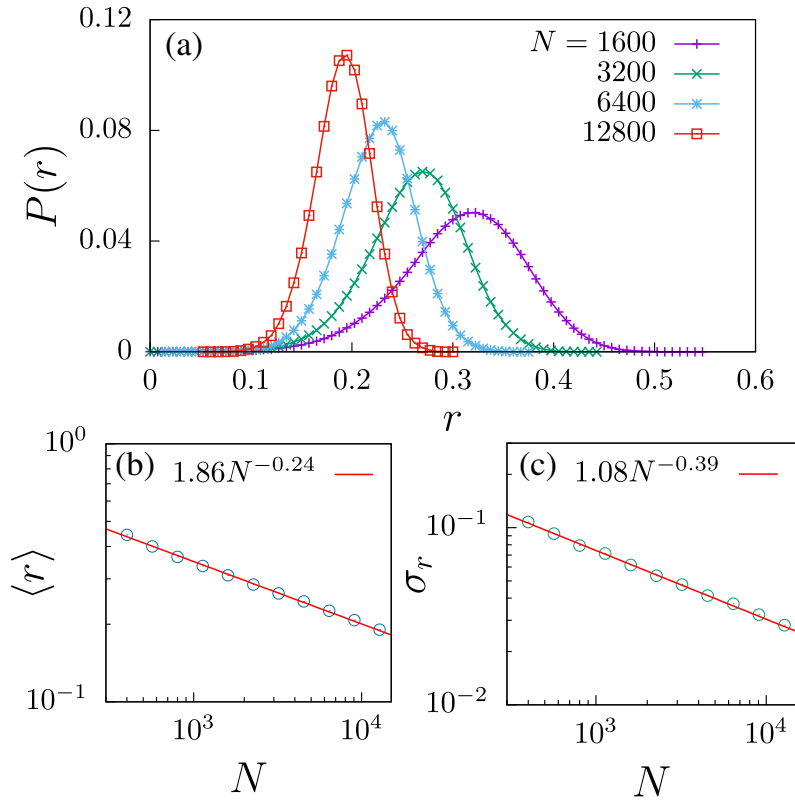Figure C.6: (a) Plot of the distribution $P(r)$ versus the order parameter value r. Data points are obtained from different 10^6 time steps in steady state and 10^3 samples for various system sizes N at $K_c(\infty)$. (b) Plot of $\langle r \rangle$ versus N. The straight line is a guideline with slope -0.24. (c) Plot of the standard deviation of $P(r)$ versus N. The straight line is a guideline with slope -0.39.
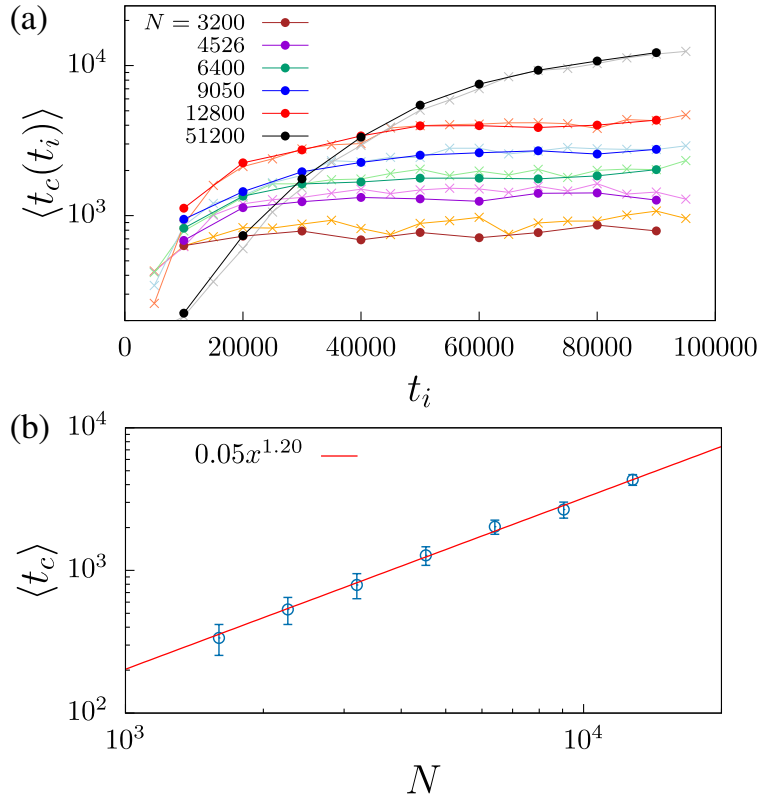
Figure C.7: (a) Plot of $\langle t_c(t_i) \rangle$ for various system sizes. The data points are averaged over 10^3 samples. The order parameter $r(t)$ was measured until time $t = 10^5$ in steps of $\Delta t = 5000$ (light, cross) and 10000 (dark, circle) to evaluate t_c. The obtained values of $\langle t_c \rangle$ seems to be saturated for $N \leq 12800$, while they are not for the case of $N = 51200$. (b) Plot of the estimated values of $\langle t_c \rangle$ versus N up to 12800. The straight line is a guideline with estimated slope 1.20.

different initial configurations for the regular sampling case shown in Fig. C.2(b).

Finally, we estimate a characteristic time $\langle t_c \rangle$, beyond which the order parameter reaches a steady state. We perform simulations up to $t = 10^5$ for the system size $N \leq 51200$ in the following way. First, we take time intervals $[t_i, t_i + \Delta t]$, where t_i is taken as the dotted ones in Fig. C.7(a) and Δt is taken appropriately as represented in the caption of Fig. C.7. Second, the order parameter is averaged over each time interval, which is denoted as $\bar{r}(t_i)$. Next, we determine the characteristic time $t_c(t_i)$ at which $r(t)$ becomes larger than $\bar{r}(t_i)$ for the first time. We repeat this process until $t_i + \Delta t = 10^5$. Next, $t_c(t_i)$ are averaged over 10^3 realizations, and the resulting mean is denoted as $\langle t_c(t_i) \rangle$. Fig. C.7(a) shows that $\langle t_c(t_i) \rangle$ seems to be saturated to a constant value (denoted as $\langle t_c \rangle$) as t_i is increased for $N \leq 12800$. However, when $N = 51200$, the simulation time 10^5 seems to be insufficient, and longer simulation time is required. Finally, we check the characteristic time $\langle t_c \rangle$ as a function of N. Fig. C.7(b) shows that $\langle t_c \rangle$ exhibits power-law behavior with respect to N as $\langle t_c \rangle \sim N^{1.2}$. Thus, the dynamic exponent for the system size N is estimated to be $\bar{z} \approx 1.2$.

Bibliography

[1] E. RENYI, "On random graph," *Publicationes Mathematicate*, vol. 6, pp. 290–297, 1959.

[2] A.-L. Barabási and R. Albert, "Emergence of scaling in random networks," *Science*, vol. 286, no. 5439, pp. 509–512, 1999.

[3] R. Albert and A.-L. Barabási, "Statistical mechanics of complex networks," *Rev. Mod. Phys.*, vol. 74, pp. 47–97, Jan 2002.

[4] M. E. J. Newman, "The structure and function of complex networks," *SIAM Review*, vol. 45, no. 2, pp. 167–256, 2003.

[5] S. N. Dorogovtsev and J. F. F. Mendes, "Evolution of networks," *Advances in Physics*, vol. 51, no. 4, pp. 1079–1187, 2002.

[6] S. Boccaletti, V. Latora, Y. Moreno, M. Chavez, and D.-U. Hwang, "Complex networks: Structure and dynamics," *Physics Reports*, vol. 424, no. 4, pp. 175 – 308, 2006.

[7] A.-L. Barabási, "Linked: The new science of networks," 2003.

[8] G. Caldarelli, *Scale-free networks: complex webs in nature and technology*. Oxford University Press, 2007.

[9] M. Newman, *Networks*. Oxford university press, 2018.

[10] S. H. Strogatz and R. E. Mirollo, "Collective synchronisation in lattices of nonlinear oscillators with randomness," *Journal of Physics A: Mathematical and General*, vol. 21, pp. L699–L705, jul 1988.

[11] T. M. Mitchell *et al.*, "Machine learning. 1997," *McGraw Hill*, vol. 45, no. 37, pp. 870–877, 1997.

[12] A. Bohrdt, C. S. Chiu, G. Ji, M. Xu, D. Greif, M. Greiner, E. Demler, F. Grusdt, and M. Knap, "Classifying snapshots of the doped hubbard model with machine learning," *Nature Physics*, vol. 15, no. 9, pp. 921–924, 2019.

[13] W. Zhang, J. Liu, and T.-C. Wei, "Machine learning of phase transitions in the percolation and xy models," *Phys. Rev. E*, vol. 99, p. 032142, Mar 2019.

[14] J. Carrasquilla and R. G. Melko, "Machine learning phases of matter," *Nature Physics*, vol. 13, no. 5, pp. 431–434, 2017.

[15] P. Broecker, J. Carrasquilla, R. G. Melko, and S. Trebst, "Machine learning quantum phases of matter beyond the fermion sign problem," *Scientific reports*, vol. 7, no. 1, pp. 1–10, 2017.

[16] J. Venderley, V. Khemani, and E.-A. Kim, "Machine learning out-of-equilibrium phases of matter," *Phys. Rev. Lett.*, vol. 120, p. 257204, Jun 2018.

[17] M. J. S. Beach, A. Golubeva, and R. G. Melko, "Machine learning vortices at the kosterlitz-thouless transition," *Phys. Rev. B*, vol. 97, p. 045207, Jan 2018.

[18] Q. Ni, M. Tang, Y. Liu, and Y.-C. Lai, "Machine learning dynamical phase transitions in complex networks," *Phys. Rev. E*, vol. 100, p. 052312, Nov 2019.

[19] W. Maass, T. Natschläger, and H. Markram, "Real-time computing without stable states: A new framework for neural computation based on perturbations," *Neural Computation*, vol. 14, no. 11, pp. 2531–2560, 2002.

[20] H. Jaeger and H. Haas, "Harnessing nonlinearity: Predicting chaotic systems and saving energy in wireless communication," *Science*, vol. 304, no. 5667, pp. 78–80, 2004.

[21] M. Lukoševičius and H. Jaeger, "Reservoir computing approaches to recurrent neural network training," *Computer Science Review*, vol. 3, no. 3, pp. 127 – 149, 2009.

[22] Z. Lu, J. Pathak, B. Hunt, M. Girvan, R. Brockett, and E. Ott, "Reservoir observers: Model-free inference of unmeasured variables in chaotic systems," *Chaos: An Interdisciplinary Journal of Nonlinear Science*, vol. 27, no. 4, p. 041102, 2017.

[23] T. L. Carroll, "Using reservoir computers to distinguish chaotic signals," *Phys. Rev. E*, vol. 98, p. 052209, Nov 2018.

[24] Z. Lu, B. R. Hunt, and E. Ott, "Attractor reconstruction by machine learning," *Chaos: An Interdisciplinary Journal of Nonlinear Science*, vol. 28, no. 6, p. 061104, 2018.

[25] J. Pathak, Z. Lu, B. R. Hunt, M. Girvan, and E. Ott, "Using machine learning to replicate chaotic attractors and calculate lyapunov exponents from data," *Chaos: An Interdisciplinary Journal of Nonlinear Science*, vol. 27, no. 12, p. 121102, 2017.

[26] J. Pathak, B. Hunt, M. Girvan, Z. Lu, and E. Ott, "Model-free prediction of large spatiotemporally chaotic systems from data: A reservoir computing approach," *Phys. Rev. Lett.*, vol. 120, p. 024102, Jan 2018.

[27] T. Weng, H. Yang, C. Gu, J. Zhang, and M. Small, "Synchronization of chaotic systems and their machine-learning models," *Phys. Rev. E*, vol. 99, p. 042203, Apr 2019.

[28] J. Jiang and Y.-C. Lai, "Model-free prediction of spatiotemporal dynamical systems with recurrent neural networks: Role of network spectral radius," *Phys. Rev. Research*, vol. 1, p. 033056, Oct 2019.

[29] H. Fan, J. Jiang, C. Zhang, X. Wang, and Y.-C. Lai, "Long-term prediction of chaotic systems with machine learning," *Phys. Rev. Research*, vol. 2, p. 012080, Mar 2020.

[30] Y. Kuramoto, *Chemical Oscillations, Waves, and Turbulence*, vol. 19 of *Springer Series in Synergetics*. Berlin, Heidelberg: Springer Berlin Heidelberg, 1984.

[31] Y. Kuramoto, *Self-entrainment of a population of coupled non-linear oscillators*. Berlin/Heidelberg: Springer-Verlag, 1975.

[32] E. Ott and T. M. Antonsen, "Low dimensional behavior of large systems of globally coupled oscillators," *Chaos: An Interdisciplinary Journal of Nonlinear Science*, vol. 18, no. 3, p. 037113, 2008.

[33] P. S. Skardal, "Low-dimensional dynamics of the kuramoto model with rational frequency distributions," *Phys. Rev. E*, vol. 98, p. 022207, Aug 2018.

[34] D. Pazó, "Thermodynamic limit of the first-order phase transition in the kuramoto model," *Phys. Rev. E*, vol. 72, p. 046211, Oct 2005.

[35] H.-A. Tanaka, A. J. Lichtenberg, and S. Oishi, "First order phase transition resulting from finite inertia in coupled oscillator systems," *Phys. Rev. Lett.*, vol. 78, pp. 2104–2107, Mar 1997.

[36] B. Ottino-Löffler and S. H. Strogatz, "Kuramoto model with uniformly spaced frequencies: Finite-n asymptotics of the locking threshold," *Phys. Rev. E*, vol. 93, p. 062220, Jun 2016.

[37] P. Ehrenfest, "Phase changes in the ordinary and extended sense classified according to the corresponding singularities of the thermodynamic potential," in *Proc Acad Sci Amsterdam*, vol. 36, pp. 153–157, 1933.

[38] D. J. Thouless, "Long-range order in one-dimensional ising systems," *Phys. Rev.*, vol. 187, pp. 732–733, Nov 1969.

[39] A. Bar and D. Mukamel, "Mixed-order phase transition in a one-dimensional model," *Phys. Rev. Lett.*, vol. 112, p. 015701, Jan 2014.

[40] F. J. Dyson, "An ising ferromagnet with discontinuous long-range order," *Communications in Mathematical Physics*, vol. 21, no. 4, pp. 269–283, 1971.

[41] M. Aizenman, J. Chayes, L. Chayes, and C. Newman, "Discontinuity of the magnetization in one-dimensional 1/ x- y 2 ising and potts models," *Journal of Statistical Physics*, vol. 50, no. 1-2, pp. 1–40, 1988.

[42] S. Jang, J. S. Lee, S. Hwang, and B. Kahng, "Ashkin-teller model and diverse opinion phase transitions on multiplex networks," *Phys. Rev. E*, vol. 92, p. 022110, Aug 2015.

[43] J. Chalupa, P. L. Leath, and G. R. Reich, "Bootstrap percolation on a bethe lattice," *Journal of Physics C: Solid State Physics*, vol. 12, pp. L31–L35, jan 1979.

[44] A. V. Goltsev, S. N. Dorogovtsev, and J. F. F. Mendes, "k-core (bootstrap) percolation on complex networks: Critical phenomena and nonlocal effects," *Phys. Rev. E*, vol. 73, p. 056101, May 2006.

[45] S. N. Dorogovtsev, A. V. Goltsev, and J. F. F. Mendes, "k-core organization of complex networks," *Phys. Rev. Lett.*, vol. 96, p. 040601, Feb 2006.

[46] D. Cellai, A. Lawlor, K. A. Dawson, and J. P. Gleeson, "Tricritical point in heterogeneous k-core percolation," *Phys. Rev. Lett.*, vol. 107, p. 175703, Oct 2011.

[47] G. J. Baxter, S. N. Dorogovtsev, K.-E. Lee, J. F. F. Mendes, and A. V. Goltsev, "Critical dynamics of the k-core pruning process," *Phys. Rev. X*, vol. 5, p. 031017, Aug 2015.

[48] D. Poland and H. A. Scheraga, "Phase transitions in one dimension and the helix—coil transition in polyamino acids," *The Journal of Chemical Physics*, vol. 45, no. 5, pp. 1456–1463, 1966.

[49] M. E. Fisher, "Effect of excluded volume on phase transitions in biopolymers," *The Journal of Chemical Physics*, vol. 45, no. 5, pp. 1469–1473, 1966.

[50] Y. Kafri, D. Mukamel, and L. Peliti, "Why is the dna denaturation transition first order?," *Phys. Rev. Lett.*, vol. 85, pp. 4988–4991, Dec 2000.

[51] S. Henkes and B. Chakraborty, "Jamming as a critical phenomenon: A field theory of zero-temperature grain packings," *Phys. Rev. Lett.*, vol. 95, p. 198002, Nov 2005.

[52] C. Toninelli, G. Biroli, and D. S. Fisher, "Jamming percolation and glass transitions in lattice models," *Phys. Rev. Lett.*, vol. 96, p. 035702, Jan 2006.

[53] J. M. Schwarz, A. J. Liu, and L. Q. Chayes, "The onset of jamming as the sudden emergence of an infinite k-core cluster," *Europhysics Letters (EPL)*, vol. 73, pp. 560–566, feb 2006.

[54] R. Alert, P. Tierno, and J. Casademunt, "Mixed-order phase transition in a colloidal crystal," *Proceedings of the National Academy of Sciences*, vol. 114, no. 49, pp. 12906–12909, 2017.

[55] J. Gómez-Gardeñes, S. Gómez, A. Arenas, and Y. Moreno, "Explosive synchronization transitions in scale-free networks," *Phys. Rev. Lett.*, vol. 106, p. 128701, Mar 2011.

[56] B. C. Coutinho, A. V. Goltsev, S. N. Dorogovtsev, and J. F. F. Mendes, "Kuramoto model with frequency-degree correlations on complex networks," *Phys. Rev. E*, vol. 87, p. 032106, Mar 2013.

[57] L. Basnarkov and V. Urumov, "Phase transitions in the kuramoto model," *Phys. Rev. E*, vol. 76, p. 057201, Nov 2007.

[58] E. A. Martens, E. Barreto, S. H. Strogatz, E. Ott, P. So, and T. M. Antonsen, "Exact results for the kuramoto model with a bimodal frequency distribution," *Phys. Rev. E*, vol. 79, p. 026204, Feb 2009.

[59] D. Pazó and E. Montbrió, "Existence of hysteresis in the kuramoto model with bimodal frequency distributions," *Phys. Rev. E*, vol. 80, p. 046215, Oct 2009.

[60] B. Pietras, N. Deschle, and A. Daffertshofer, "Equivalence of coupled networks and networks with multimodal frequency distributions: Conditions for the bimodal and trimodal case," *Phys. Rev. E*, vol. 94, p. 052211, Nov 2016.

[61] H. Hong, H. Park, and M. Y. Choi, "Collective synchronization in spatially extended systems of coupled oscillators with random frequencies," *Phys. Rev. E*, vol. 72, p. 036217, Sep 2005.

[62] H. Hong, H. Chaté, H. Park, and L.-H. Tang, "Entrainment transition in populations of random frequency oscillators," *Phys. Rev. Lett.*, vol. 99, p. 184101, Oct 2007.

[63] J. Um, H. Hong, and H. Park, "Nature of synchronization transitions in random networks of coupled oscillators," *Phys. Rev. E*, vol. 89, p. 012810, Jan 2014.

[64] H. Hong, H. Chaté, L.-H. Tang, and H. Park, "Finite-size scaling, dynamic fluctuations, and hyperscaling relation in the kuramoto model," *Phys. Rev. E*, vol. 92, p. 022122, Aug 2015.

[65] T. K. D. Peron and F. A. Rodrigues, "Determination of the critical coupling of explosive synchronization transitions in scale-free networks by mean-field approximations," *Phys. Rev. E*, vol. 86, p. 056108, Nov 2012.

[66] P. Ji, T. K. D. Peron, P. J. Menck, F. A. Rodrigues, and J. Kurths, "Cluster explosive synchronization in complex networks," *Phys. Rev. Lett.*, vol. 110, p. 218701, May 2013.

[67] X. Zhang, S. Boccaletti, S. Guan, and Z. Liu, "Explosive synchronization in adaptive and multilayer networks," *Phys. Rev. Lett.*, vol. 114, p. 038701, Jan 2015.

[68] J. Van Hemmen and W. Wreszinski, "Lyapunov function for the kuramoto model of nonlinearly coupled oscillators," *Journal of Statistical Physics*, vol. 72, no. 1-2, pp. 145–166, 1993.

[69] D. Iatsenko, S. Petkoski, P. V. E. McClintock, and A. Stefanovska, "Stationary and traveling wave states of the kuramoto model with an arbitrary distribution of frequencies and coupling strengths," *Phys. Rev. Lett.*, vol. 110, p. 064101, Feb 2013.

[70] M. Nitzan, J. Casadiego, and M. Timme, "Revealing physical interaction networks from statistics of collective dynamics," *Science Advances*, vol. 3, no. 2, 2017.

[71] W.-X. Wang, Y.-C. Lai, and C. Grebogi, "Data based identification and prediction of nonlinear and complex dynamical systems," *Physics Reports*, vol. 644, pp. 1 – 76, 2016. Data based identification and prediction of nonlinear and complex dynamical systems.

[72] D. Eroglu, M. Tanzi, S. van Strien, and T. Pereira, "Revealing dynamics, communities, and criticality from data," *Phys. Rev. X*, vol. 10, p. 021047, Jun 2020.

[73] F. Mormann, T. Kreuz, C. Rieke, R. G. Andrzejak, A. Kraskov, P. David, C. E. Elger, and K. Lehnertz, "On the predictability of epileptic seizures," *Clinical Neurophysiology*, vol. 116, no. 3, pp. 569 – 587, 2005.

[74] P. Mirowski, D. Madhavan, Y. LeCun, and R. Kuzniecky, "Classification of patterns of eeg synchronization for seizure prediction," *Clinical Neurophysiology*, vol. 120, no. 11, pp. 1927 – 1940, 2009.

[75] S. Chandaka, A. Chatterjee, and S. Munshi, "Cross-correlation aided support vector machine classifier for classification of eeg signals," *Expert Systems with Applications*, vol. 36, no. 2, Part 1, pp. 1329 – 1336, 2009.

[76] J. R. Williamson, D. W. Bliss, D. W. Browne, and J. T. Narayanan, "Seizure prediction using eeg spatiotemporal correlation structure," *Epilepsy & Behavior*, vol. 25, no. 2, pp. 230 – 238, 2012.

[77] L.-H. Tang, "To synchronize or not to synchronize, that is the question: finite-size scaling and fluctuation effects in the kuramoto model," *Journal of Statistical Mechanics: Theory and Experiment*, vol. 2011, p. P01034, jan 2011.

[78] F. A. Rodrigues, T. K. D. Peron, P. Ji, and J. Kurths, "The kuramoto model in complex networks," *Physics Reports*, vol. 610, pp. 1 – 98, 2016. The Kuramoto model in complex networks.

[79] I. Goodfellow, Y. Bengio, and A. Courville, *Deep Learning*. MIT Press, 2016.

[80] A. Arenas, A. Díaz-Guilera, and C. J. Pérez-Vicente, "Synchronization reveals topological scales in complex networks," *Phys. Rev. Lett.*, vol. 96, p. 114102, Mar 2006.

[81] R. A. Rossi and N. K. Ahmed, "The network data repository with interactive graph analytics and visualization," in *AAAI*, 2015.

[82] J. C. Bronski, L. DeVille, and M. Jip Park, "Fully synchronous solutions and the synchronization phase transition for the finite-n kuramoto model," *Chaos: An Interdisciplinary Journal of Nonlinear Science*, vol. 22, no. 3, p. 033133, 2012.

[83] C. Wang, N. Rubido, C. Grebogi, and M. S. Baptista, "Approximate solution for frequency synchronization in a finite-size kuramoto model," *Phys. Rev. E*, vol. 92, p. 062808, Dec 2015.

초 록

　　서로 간의 상호작용이 있는 다수의 개체로 구성된 계는 집단적인 행동을 보인다는 것이 잘 알려져있다. 그러한 집단적인 행동의 대표적인 예로써, 동기화 현상은 두 개 이상의 개체가 상호작용을 통해 모두 동일한 상태에 이르게 되는 과정을 뜻한다. 반딧불의 깜빡임, 귀뚜라미의 울음소리, 심장박동원세포 등 자연에는 동기화 현상의 수많은 예들이 있다. 동기화 현상을 이해하고 묘사하기 위한 가장 대표적이고 적합한 모형으로, 결합된 진동자들로 이루어진 시스템을 생각해 볼 수 있다. 시스템에 있는 각각의 진동자들은 각자의 특성을 나타내는 고유 진동수(natural frequency)를 갖고 있으며, 각각의 위상(phase)들은 시스템의 다른 진동자들과의 상호작용을 통해 시간이 지남에 따라 점차 맞추어 나가게 된다. 이 때, 이러한 위상 동기화가 일어나는 과정에서 진동자들 사이의 연결 또는 상호작용들은 복잡계 네트워크 위의 링크(link)로 표현될 수 있으며, 각각의 개체 혹은 진동자들은 노드(node)로 표현된다. 이러한 결합된 진동자들에 대한 수많은 연구들이 지난 20여년간 이루어져 왔다.

　　집단현상을 묘사하는 간단하면서도 대표적인 모형인 구라모토 모형을 차용하여 결합된 진동자들의 동기화 현상에 대한 많은 연구들이 진행되어왔다. 구라모토 모형은 카오스 동역학, 동기화 상전이 등의 다양한 특성을 나타내는만큼, 흥미로운 연구들이 많이 이루어져 왔는데, 먼저, 구라모토 모형에서 나타나는 동기화 현상에 대한 선행연구들에서 밝혀진 중요한 결과 및 배경들을 이 학위 논문의 앞부분에서 소개하였다.

　　그리고 각각을 주요한 연구주제로써, 결합된 진동자들의 시스템에 대한 두 가지 방법론을 사용하여 논문을 구성을 하였다. 첫번째 연구에서는, 유효 포텐셜(effective potential)을 이용한 방법론을 도입하여 해석적인 방법으로 구라모토 모형을 분석하였다. 구라모토 모형에서는 고유 진동수의 분포형태가 변함에 따라 동기화 상전이의 유형또한 변하게 되는데, 구라모토 방정식으로부터 유도한 자기일관성 방정식(self-consistency equation)을 사용하여 이러한 결과를 해석적으로 분석할 수 있다. 하지

만, 이러한 방법은 시스템의 안정성과 같은 상세한 특징을 파악하는 데에는 어려움이 있다. 이 연구에서는, 자기일관성 방정식을 적분하여 유도한 유효포텐셜 방법론을 도입하여, 열역학적 극한에 있는 시스템에 대하여 1차 상전이, 2차 상전이 뿐만 아니라 하이브리드 동기화 상전이가 나타날 때의 포텐셜 경관(potential landscape)을 파악하였으며, 특히, 하이브리드 상전이에서는 유효 포텐셜의 최솟값이 임계점에서 평평한 형태를 보인다는 것을 확인하였다. 이러한 결과들은 동기화 상전이의 형태를 파악하는 데에 있어서 유효 포텐셜이 주요한 역할을 해줄 수 있음을 의미한다.

두번째 연구에서는, 데이터 기반 방법론인 기계학습을 사용하여 결합된 진동자들의 시스템을 파악하고, 이러한 방법이 실제의 시스템에 대해서도 확장이 가능한지에 대하여 연구하였다. 최근, 과학분야 뿐만아니라 여러 다양한 분야에서 기계학습에 대한 관심이 높아져 왔는데, 물리적 계에 대해서도 기계학습을 이용한 분류 및 생성 작업을 통해 많은 발전이 이루어져왔다. 본 연구에서는, 여러 기계학습의 모형들을 이용해 구라모토 모형에서 보이는 동기화 상전이 및 비선형, 카오스 동역학을 분석하였다. 질서변수의 시간에 따른 동역학으로부터 진동자들 사이에 내재된 상호작용을 찾고, 진동자들의 위상으로 부터 동기화된 상태와 비동기화된 상태를 구분하여 임계점을 찾는 데에 기계학습 방법을 적용시켜 보았다. 유한 크기 축적 방법(finite-size scaling)을 이용하여 이러한 결과들이 기존의 알려진 구라모토 모형에 대한 눈금 바꿈 행태(scaling behavior)의 결과와 일관성이 있는 것을 확인하였다. 또한, 모든 진동자들의 위상 동역학을 인공 신경망에 입력으로 넣어줌으로써, 진동자들의 이후의 동역학 행태를 파악할 뿐만 아니라, 기저에 깔려 있는 실제 쥐의 시각 피질 네트워크를 알아내는 연구를 진행하였다. 따라서, 동기화 현상 및 비선형 동역학을 보이는 여러 실제의 시스템들에 대한 구라모토 모형의 응용이 가능함에 따라, 본 연구는 그러한 시스템에 대해서도 기계학습 방법을 활용할 수 있는 가능성을 내포한다.